Search for Modification of Vector Meson Properties in Nuclei

By

Clarisse Tur

Licence et Maitrise de Physique Fondamentale
Université de Paris Sud, Orsay, 2000

Master of Science
University of South Carolina, 2003

– –

Submitted in Partial Fulfillment of the Requirements

for the Degree of Doctor of Philosophy in the

Department of Physics and Astronomy

University of South Carolina

2005

Major Professor	Committee member
Committee member	Chair of Examining Committee
Committee member	Dean of the Graduate School

ABSTRACT

Search for Modification of Vector Meson Properties in Nuclei

Clarisse Tur

QCD sum rules depict the atomic nucleus as being a medium with partially restored chiral symmetry. This property of the nucleus would imply that the properties of vector mesons, such as their mass and width, are modified when produced in the nuclear medium, since they are controlled by chiral symmetry and its spontaneous as well as explicit breaking in QCD. A number of theoretical models have predicted a dropping in the mass of the ρ and ω mesons at normal nuclear density. And so, the g7 (or E01-112) experiment has been designed to look for medium effects on the properties of the light vector mesons (ρ, ω, and ϕ) in photoproduction, through their rare leptonic decay into e^+e^-. This decay channel has been preferred to the two pion channel to avoid distorting the information by strong final interaction. The data for this experiment was taken in the fall of 2002 using the CLAS detector at the Jefferson Laboratory. A bremsstrahlung's photon beam was sent on a target containing a liquid deuterium cell and several nuclear targets: C, Fe, Ti, and Pb. A depletion of the ω and ϕ peaks has been observed with increasing target density. This depletion was not seen as markedly in the simulations done using a code based on the BUU transport equations. The data was broken up per target and fitted using the unmodified ρ, ω and ϕ invariant mass distributions from the BUU simulation code, the omega Dalitz decay contribution also from the same code and the combinatorial background shape from the mixed e^+e^- g7 events. The overall quality of the fits is suggestive of no medium effects observed on the properties of the vector mesons from this data set.

CONTENTS

LIST OF TABLES

LIST OF FIGURES

Chapter 1

Introduction

The properties of vector mesons, such as their mass and width, are predicted to be modified in a dense medium such as a nucleus. A partial restoration of chiral symmetry at normal nuclear density has been proposed as a possible cause for those modifications besides more "conventional" many-body effects. The E01-112 (g7) experiment has been designed to look for possible medium effects on the properties of the light vector mesons (ρ, ω and ϕ), in photoproduction, through their rare leptonic decay into e^+e^- pairs. More precisely, the reaction of interest to g7 is:

$$\gamma A \rightarrow VA' \rightarrow e^+e^-A', \tag{1.1}$$

where V = ρ, ω or ϕ.

The experiment was twice proposed ([Ber94], [Dja01]) and twice approved by the Program Advisory Committee at the Jefferson Laboratory before successfully running in the fall of 2002. The data was collected September 20, 2002 through November 13, 2002 using the CEBAF accelerator and the CLAS detector. A bremsstrahlung photon beam was sent on a multi-segmented target containing a liquid deuterium cell used as a reference and several nuclear targets: C, Fe, Ti

and Pb. The detail of the experimental setup will be given in the second chapter of the thesis.

A simulation code developed by the group of U. Mosel at the University of Giessen was used to simulate the inclusive e^+e^- photo-production under the conditions of the g7 experiment in order to make comparisons with the experimental data. The code treats the photon-nucleus reactions as a two-step process where, in the first step, the incoming photons react with a single nucleon taking into account the effects of shadowing, then in the second step, the produced particles are propagated explicitly through the nucleus allowing for all kinds of final-state interactions. The last part of the model is governed by the semiclassical Boltzmann-Uehling-Uhlenbeck (BUU) transport equations. The code actually allows one to simulate the inclusive particle production in heavy-ion collisions from 200A MeV to 200A GeV as well as in pion-, photon-, and electron-induced reactions with the very same physical input. More on the details of the simulation program will be given in the third chapter.

The fourth chapter will give the details of the analysis procedure. One major challenge for the analysis of the g7 data set was to separate the e^+e^- final state events from the very large hadronic background (i.e. the decay of the vector mesons into two pions). In doing so, one ought to be careful to reject as much as possible of the pion background, while trying to keep as many as possible of the electron events. Thus the event selection method taking this compromise into account will be presented in detail. A subsection of the fourth chapter will also include the invariant mass spectra obtained using the simulation code detailed in the third chapter and the same spectra from the data obtained by applying the cuts identified in the event selection phase.

The fifth chapter will consist in presenting the results i.e. the fitted invariant mass spectra per g7 target and the outcome in terms of physics i.e. the final word on the presence or absence of medium effects.

Finally, as far as the present chapter is concerned, the following subsections

will give as much background information as possible on the physics behind the g7 experiment and among other things, some general information on the topic of medium effects on the properties of hadrons as well as the detail of the findings of some of the previous theoretical and experimental work on the subject.

1.1 Why would the properties of the hadrons change in the medium and how?

The in-medium effects that can influence the properties of hadrons may be divided into two categories: the "conventional" in-medium effects and those due to new physics, namely a partial/full restoration of chiral symmetry ([Ko97]) in the medium. Those two categories of effects will be developed in the following two sub-sections with a very strong emphasis on the chiral symmetry and its influence on the properties of hadrons.

1.1.1 The "conventional" many-body effects

A nucleus or a hadronic system created in heavy-ion collisions is made up of strongly interacting particles. Therefore, many-body excitations may be present that carry the same quantum numbers as the hadrons under consideration and thus can mix with the hadronic states ([Ko97]). For instance, pions at finite momenta interact very strongly through the p-wave interaction, which is dominated by the P_{33} Δ-resonance. This leads to a strong mixing of the pion with nuclear particle-hole and delta-hole excitations. As a result, the pion-like excitation spectrum develops several branches, which, to leading order, correspond to the pion, particle-hole and delta-hole excitations. The consequence is a modified in-medium pion dispersion relation. In the context of heavy-ion collisions, it has been argued that such a modified pion dispersion relation would lead to an enhanced dilepton yield at invariant masses close to twice the pion mass. Sim-

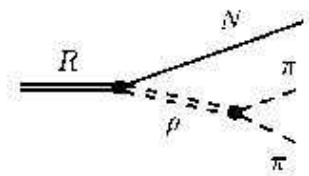

Figure 1.1: Decay of a nucleon resonance into two pions via a rho meson.

ilar to the pion, that becomes renormalized by delta-hole loops in the nuclear medium, there are contributions to the self-energy of the rho from resonance-hole loops ([Pet98]). The decay of those resonances will lead to an in-medium broadening (or collisional broadening) of the rho. Figure 1.1 illustrates the decay of a nucleonic resonance into two pions via a rho meson.

In addition, in the nuclear environment, simple many-body effects, such as Pauli blocking, are at work, which can lead to considerable modification of hadronic properties. For the particular case of the photon-induced reactions, one has to also take into account collective effects such as shadowing (i.e. $\sigma_{\gamma A} < A\sigma_{\gamma N}$) above photon energies of approximately 1 GeV ([Fal02]). In naive words, this corresponds to the situation where the nucleons on the front side of the nucleus shadow or hide the downstream nucleons.

1.1.2 Chiral symmetry restoration

This second category of medium effects is a more inspiring one as it implies the possibility of new physics: The properties of hadrons are controlled by chiral symmetry and its spontaneous as well as explicit breaking. So, in a medium where chiral symmetry is partially restored, one would expect them to have different properties than in the vacuum.

In QCD, chiral symmetry is indeed both explicitly and spontaneously broken. The explicit breaking stems from the presence of mass terms in the QCD Lagrangian due to the small but non-zero masses of the u, d and s quarks (one can see this when rewriting the QCD Lagrangian in terms of the left and right

components of the Dirac spinors and trying to swap the left and right indexes). Now, in a world where the masses of the u, d and s quarks would be zero, the QCD Lagrangian would appear to be chirally symmetric but the ground state solution would break the chiral symmetry. Otherwise stated, in such a world, chiral symmetry would be spontaneously broken.

The spontaneous breaking of chiral symmetry in QCD leads to a non-zero value for $< q\overline{q} >$ ([Ko97]). This expectation value is called the chiral condensate or the scalar quark condensate. The value of the chiral condensate is zero for a chirally symmetric phase. A phase transition of hadronic matter to a chirally restored phase is expected to take place for temperatures above 150MeV and/or densities above $5\rho_0$, where ρ_0 $(= 0.16 fm^{-3})$ is the normal nuclear density. So, the chiral condensate plays the role of an order parameter for the onset of this transition. While such a phase at high density and temperature can be produced in heavy-ion collisions, the atomic nucleus itself is a system at zero temperature and finite density. QCD sum rules predict a 30% decrease in the value of the chiral condensate at normal nuclear density ([Coh95]) and this qualifies the atomic nucleus as a medium with partially restored chiral symmetry according to the discussion above. Consequently, one should be able to observe the medium modifications on the properties of the hadrons in pion-, proton- or photon-induced reactions. The g7 experiment falls into this last category.

1.1.3 Which properties of hadrons are subject to be modified if chiral symmetry is partially restored?

The contents of this subsection are largely inspired by the reference [Leu01] and so, the reader is encouraged to refer to that paper for more ample information.

When chiral symmetry is progressively restored, the properties of chiral partners should start to approach each other and finally become identical in the

chirally symmetric phase. Let us take the example of the isovector vector meson ρ and its much heavier chiral partner, the isovector axial-vector meson a1. In principle, one can distinguish three types of phenomena as chiral symmetry gets restored (with increasing temperature and density):

a). Mass shifts: The masses of ρ and a1 might approach each other. This may happen in different ways: the masses may meet at a value somewhere in between their vacuum masses (and possibly drop together afterwards). It is also possible that the masses of both mesons drop and finally (approximately) vanish at the point of chiral symmetry restoration.

b). Peak broadening: From the experimental point of view the ρ (a1) meson shows up as a peak in the vector (axial-vector) channel. In a medium the peaks might get broader (maybe without a change of the respective peak positions, i.e. the nominal masses) until the melted spectra in both channels become degenerate.

c). Mixing: The distinct peaks might maintain (maybe without shifts or broadening), but the a1 peak shows up with increasing height in the vector channel and vice versa.

In the case of the g7 experiment, the a1 meson is not produced and so, the mixing effect is not studied.

1.2 What are the theoretical predictions for the properties of the vector mesons at normal nuclear density?

The study of the density/temperature-induced changes on the properties of hadrons, with a particular emphasis on the properties of the vector mesons, has seen much theoretical as well as experimental interest. The focus of this section is the theoretical aspect, the experimental aspect being the subject of the

next section. In particular, the assertion by Brown and Rho ([Bro91]) based on arguments of restoration of the scale-invariance of QCD in dense matter, that the masses of all non-strange hadrons, with the exception of the Goldstone bosons, should scale with the quark condensate, thereby predicting a 20% decrease in the masses of the ρ and ω mesons at normal nuclear density, has triggered an excitement still strong within the "medium-effects community", some 15 years after the publication date of their paper. Their idea remains a conjecture of which the theoretical foundations are still being worked out, but, the basic argument of Brown and Rho is the following ([Ko97]): Hadron masses, such as that of the ρ meson, violate scale-invariance, which is a symmetry of the classical QCD Lagrangian. In QCD, scale-invariance is broken at the quantum level by the so called trace anomaly, which is proportional to the gluon condensate. Thus, one could imagine that with the disappearance of the gluon condensate, i.e. the bag pressure, scale-invariance is restored. On the hadronic level, this implies that the hadron masses have to vanish. Therefore, one could argue that the hadron masses should scale with the bag pressure. Then Brown and Rho go even further. They assume that the gluon condensate can be separated into a hard and a soft part. The latter scales with the quark condensate and is also responsible for the masses of the light hadrons.

This conjecture found some support from more quantitative calculations by Hatsuda and Lee ([Hat92]) a year later, who, based on QCD sum rules, predicted an 18% drop for the masses of the same vector mesons at normal nuclear density. However it must be noted that those authors made the "narrow width approximation" i.e. excluded by hand the possibility of width broadening via chiral symmetry restoration. Leupold and Mosel later emphasized the shortcomings of the QCD sum rules ([Leu01], [Leu98]), namely their lack of predictive power to fix both the mass and the width. Typically some assumption is made concerning the width, in order to predict something about the mass. The predictions are strongly dependent on the aformentioned assumption: the masses should indeed

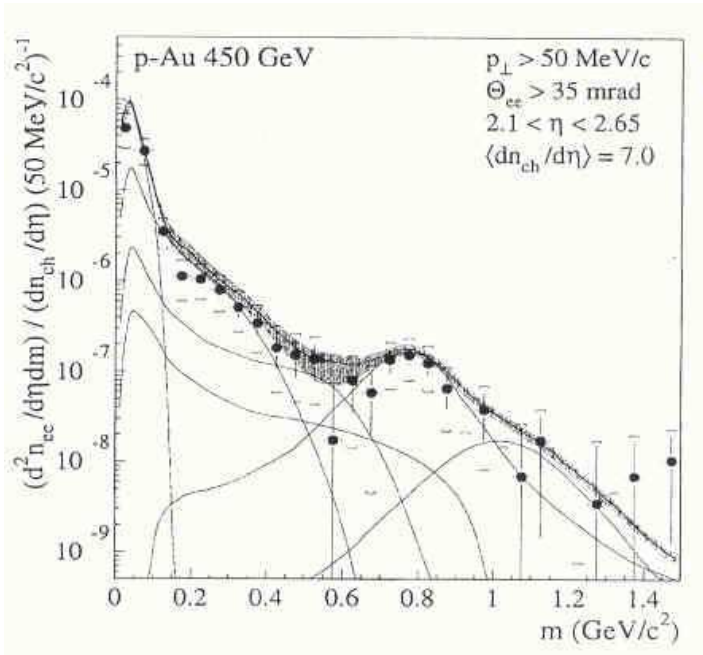

Figure 1.2: Inclusive e^+e^- mass spectra in 450 GeV p-Au collisions at CERES showing the data and the various contributions from hadron decays ([Aga95]). The shaded region indicates the systematic error on the summed contributions.

decrease if the width is small, but they stay constant or even increase if the width increases. So, the theoretical predictions can vary quite a bit.

1.3 What has been done on the experimental side?

The first experimental clue as to the possibility of the manifestation of a medium-lowered ρ mass came from the CERES and HELIOS/3 collaborations of CERN in 1995 ([Aga95], [Mas95]). For instance, the CERES collaboration reported on measurements of low-mass e^+e^- pairs from p-Au and S-Au collisions. While their proton-induced data could satisfactorily be accounted for by summing various hadron decay contributions, an enhancement over the hadronic contributions was observed for the S-Au data. The Figures 1.2 and 1.3 illustrate these results.

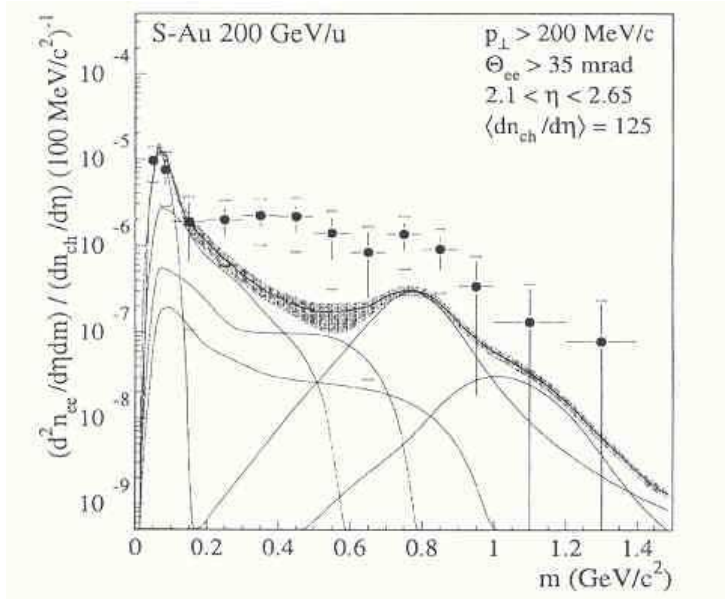

Figure 1.3: Inclusive e^+e^- mass spectra in 200 GeV/nucleon S-Au collisions at CERES. Same explanations as for 1.2.

The same year, some theorists claimed being able to account for this excess by using a relativistic transport model and assuming a drop in the mass of the ρ ([Li95]). However, it has also been suggested that more conservative effects, such as an in-medium modified pion dispersion relation may be able to provide enough enhancement ([Son96], [Koc96]). Since no clear discrimination between the two scenarios (i.e. hadronic versus dropping-mass) could be established more experiments were needed.

More recently, a large downward mass shift has been reported for the ρ meson by the TAGX collaboration, who sent photons on a ^3He target and detected the $\pi^+\pi^-$ pairs stemming from subthreshold ρ production ([Kag99], [Lol98]). A claim of observing a medium-modified vector meson invariant mass spectrum has been made by a collaboration at the KEK-PS in an experiment (E325) where 12 GeV protons were sent on nuclear targets such as carbon and copper and the outcoming e^+e^- pairs were detected ([Oza01], [Oza02]). Very recently, results came from an experiment using the Crystal Barrel/TAPS at ELSA claiming a downward shift in the mass of the ω, where the analysis focused on the $\pi^0\gamma$

Table 1.1: Characteristics of the ρ, ω and ϕ mesons

Parameter	ρ-meson	ω-meson	ϕ-meson
Lepton branching ratio	$e^+e^-(0.0044\%)$	$e^+e^-(0.0072\%)$	$e^+e^-(0.0031\%)$
Hadron branching ratio	$2\pi(100\%)$	$3\pi(89\%)$, $2\pi(2\%)$	2K(84%), $3\pi(12\%)$
m_V (MeV)	771.1	782.57	1019.45
Γ_V (MeV)	149.2	8.44	4.26
cτ (fm)	1.3	23.4	44.4
σ_{VN} (mb)	21	21	12

decay of low-momentum ω mesons produced by sending photons on a nuclear target ([Trn05]). All these experiments are yielding results complementary to each other and offer excitement. But, no clear consensus has yet emerged between the various analyses and some of the results have been the subject of criticism (e.g. [Bra02]). This implies that there is still a need for further experimentation.

1.4 Why are the light vector mesons particularly attractive among all hadrons?

The characteristic features of the vector mesons are given in Table 1.1. Any experimentalist wishing to study the medium effects on the mass spectra of hadrons need to be careful about three important constraints: on the one hand, the lifetime of the hadron and the production energy, which need to be considered in conjunction, and on the other hand the hadron's decay channel.

In the case of the vector mesons, the shorter lifetime of the ρ makes it a more interesting candidate than the ω or the ϕ, since this gives it a better chance

of actually decaying inside the nucleus. The choice of the production energy should be motivated by the desire to be as close to the ρ production threshold as possible to give it as little chance as possible of escaping from the nucleus before it decays. The photon beam energy threshold to produce a ρ on a proton is 1.086 GeV (this threshold is 1.108 GeV for an ω and 1.574 GeV for a ϕ). At the g7 energies, most of the ω and ϕ mesons are expected to decay outside, even for the case of a big nucleus such as the lead. Indeed, one would expect the maximum counting rate at $E_\gamma = 1.5$ GeV where both the ρ and ω production cross sections reach their maximum values. For this energy, all length scales are boosted by a factor of two. Thus, the decay length is expected to be 2.5 fm for the ρ-meson, 45 fm for the ω-meson and 85 fm for the ϕ-meson. These lengths should be compared to the radii of the target nuclei: 2.5 fm for the carbon, 4.5 fm for the iron and 6.5 fm for the lead. A simple calculation shows that 63% of the ρ-mesons will decay inside the carbon, 83% inside the iron and 93% inside the lead. For the narrow vector mesons, the situation is different: even inside the lead, only 13% of the ω-mesons and 7% of the ϕ-mesons will decay in the nuclear medium ([Ber94]). Actually, according to Bertin and Guichon ([Ber90]), the ϕ-meson is not expected to be shifted , because in first approximation, the ϕ does not couple to the nuclear field. Now, this also means that detecting the ϕ can provide a nice handle on the invariant mass spectra, since it is expected at its known mass value.

While almost 100% of the ρ mesons decay into $\pi^+\pi^-$ pairs, this decay channel is "unclean" in the sense that pions interact strongly and will undergo many secondary interactions before even getting out of the nucleus. And this will essentially wash out the information about the vector meson that gave them birth. In the year 2000, a paper published by Effenberger and Mosel ([Eff00]), gave predictions for the $\pi^+\pi^-$ invariant mass spectrum in γC and γPb reactions, using a BUU transport model including a dropping of the meson masses. The outcome was that the $\pi^+\pi^-$ spectrum is hardly influenced by such a medium

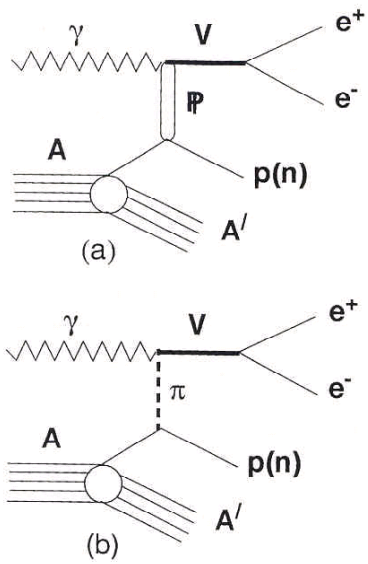

Figure 1.4: Feynman diagrams of Vector Meson Photoproduction off nuclei ([Ber94]): (a). Diffractive photoproduction. (b). One Pion Exchange mechanism of photoproduction.

modification. This is simply due to the fact that the pions have a very short mean free path in the nuclear medium (about 1 fm). Therefore the probability that two pions that stem from a decay of a ρ-meson at normal nuclear density are both able to propagate to the vacuum without rescattering is very low. The e^+e^- channel is comparatively a much cleaner decay channel since the leptons only interact electromagnetically. The price to pay in that case is the very small branching ratio (of the order of 10^{-5}). But the mere existence of this channel for the ρ, ω and ϕ mesons is also what makes these vector mesons experimentally attractive.

The g7 experiment was designed taking all these factors into consideration. The Feynman diagrams for the photoproduction of the vector mesons are shown in Figure 1.4. The diffractive mechanism and the One Pion Exchange (OPE) mechanism give the bulk of the vector meson production.

Chapter 2

The Experimental setup

The content of this chapter is largely inspired by the M.S. Thesis of C. Tur ([Tur03]), although it tends to be more succinct on some levels and more elaborate on others. The reader is encouraged to read this reference for a different insight.

The g7 data was taken at the TJNAF (Thomas Jefferson National Accelerator Facility) also know as the Jefferson Laboratory or simply Jlab. Jlab is a nuclear physics research laboratory run by the Southeastern Universities Research Association (SURA) for the Department of Energy in Newport News, Virginia. Its primary goal is to do basic research in order to better understand the atom's nucleus, but it conducts, as a secondary goal, some applied research as well, for using the Free-Electron Lasers (FEL) based on technology that Jlab developed for its own experiments.

For the purpose of basic research, Jlab houses a continuous electron beam accelerator, CEBAF, and 3 experimental halls, the Halls A, B and C. CEBAF was originally designed to deliver electrons with energies up to a maximum of 4 GeV (which was achieved in 1997), but, since 2000, it routinely delivers beam

energies up to 6 GeV, which allows experiments at the nuclear and particle physics interface. The energy regime being studied is right in-between the regime were the physical observations can be described in terms of the nucleon and meson degrees of freedom and the one where things can be described in terms of the quark and gluon degrees of freedom. A lot of the experimental effort is being devoted to the study of the structure of the nucleon, the spectroscopy of the higher nucleon resonances (the N^* resonances), and the multinucleon correlations in nuclei. There is a project of upgrading CEBAF to deliver beam energies up to 12 GeV and to build an extra experimental hall, the Hall D. The Lab also has a nuclear theory group pursuing a broad program of theoretical research in support of its experimental physics program. A few of the topics of interest to the theory group are the study of the spectra and decays of hadrons and confinement in QCD, the hadron form factors and quark-gluon distributions, the strangeness and parity violation in hadrons and nuclei, the few-body and many-body nuclear physics.

The three experimental halls have complementary facilities, and each has a different mode of operation ([Gil02]). Hall A is devoted to precision measurements, and houses twin high-resolution spectrometers that can each be placed at different angles with respect to the beam. Hall C is similar, but is used for what Jlab calls major set-up experiments, those that require complex dedicated apparatus. Hall B contains the CLAS, a detector with a toroidal magnetic field configuration that covers 90% of 4π, and is run by a collaboration of approximately 200 scientists.

The following sections will give more detailed descriptions of the equipment used for specifically the g7 experiment, i.e the CEBAF accelerator, the CLAS detector and the g7 target.

2.1 CEBAF: The Continuous Electron Beam Accelerator Facility

A major source of inspiration for this section was the reference [Lee01], in which the interested reader can find a rather complete description of CEBAF from a historical and technical point of view. It also gives a nice list of the past physics achievements it enabled and the future research perspectives.

The original idea behind the proposal of CEBAF was to have an accelerator to study the interface between the nuclear and the particle physics, the transition region between the energy regime where strongly interacting matter is understood as nucleon bound states and the regime where the underlying quark-gluon structure appears. This required a combination of characteristics: multi-GeV energy for spacial resolution and kinematic flexibility, high intensity for precise measurement of relatively small electromagnetic cross sections, high duty factor to allow coincidence experiments, and beam quality sufficient for use with high-resolution spectrometers and detectors. Essential for the new accelerator were also: the continuous wave operation, currents up to 200 μA, and simultaneous delivery of beams to multiple users. The upper limit for the beam energy, as originally specified, was 4 GeV.

Those specifications where indeed met and gave birth to CEBAF, a five-pass recirculating superconducting radiofrequency LINAC, capable of simultaneous delivery of beam to three end stations of continuous wave beams of up to 200 μA with 75% polarization (if needed) and a relative momentum spread of a few 10^{-5}. CEBAF routinely delivers beam currents sufficient to achieve luminosities of several times $10^{38} cm^{-2} s^{-1}$ to Halls A and C. The properties of the Hall B detector, CLAS, however limit the maximum luminosity for this Hall, for which the beam current is four orders of magnitude smaller than that simultaneously delivered to the other Halls. The lowest operating energy is 0.6 GeV, the present full energy is nearly 6 GeV, and an upgrade to 12 GeV is possible and indeed

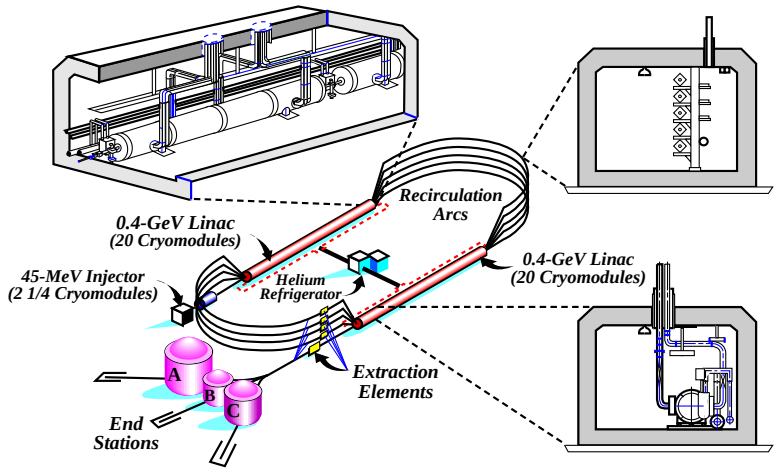

Figure 2.1: Schematic of CEBAF at 4 GeV (design goal achieved in 1997). CEBAF can deliver up to 6 GeV since the year 2000.

planned. A schematic of CEBAF as it stands now is shown in Figure 2.1. The combination of five-pass recirculation, a three-laser photocathode source, and subharmonic-rf-separator-based extraction enables simultaneous delivery of three beams at different energies, with hall-to-hall current ratios approaching 10^6, and with a specified orientation of the beam polarization. The total length of the accelerator is 1.4 km.

The most important innovations in CEBAF are the choice of the superconducting radiofrequency technology and the use of multipass beam recirculation. Neither had been previously applied on the scale of CEBAF. Actually, until LEP II came into operation, CEBAF was the world's largest implementation of superconducting radiofrequency technology. Beam recirculation minimizes the cost of that implementation.

Simultaneous delivery of highly polarized and nominally unpolarized beam has become routine. The polarized source liberates electrons from a Cs and NF3 coated Gallium Arsenide crystal by means of photo-emission. The duty-factor conserving three beam operation is implemented by creating three interlaced 499 MHz beams at the source (at 100 keV). Spaced apart by 120° of rf phase, they form a 1497 MHz beam in which each bunch has properties, that may differ

from its immediately preceding and trailing pair of neighbors, but which repeats every third bunch. This is achieved by using three independent rf-gain-switched lasers directed at a single photocathode (the Gallium Arsenide crystal). The beam formed this way has a 2.004 ns bunch structure and progresses into the injector (each laser "fires" every 2ns (= 1 / 499 MHz) producing the beam for a given experimental hall). There is a spare gun in case the photocathode gets old or damaged and switching from the one to the other takes about 1 hour. The injector has 18 accelerating cavities, which originally were designed to boost the electrons up to 45 MeV in energy, but have by the year 2000 been able to get them up to 67 MeV. The beam enters then into the north LINAC, made of 160 accelerating cavities, is then guided to the south LINAC by the east arc, where dipole magnets bend its trajectory. The LINACs were originally designed to give an extra 0.4 GeV of energy to the electrons, but are by now able to go up to 0.6 GeV. The beam particles get further accelerated in the south LINAC, exactly similar in design to the north LINAC, and enter the west arc to be led to the north LINAC again, and so forth, up to five passes total in each LINAC. In the arcs, the electrons in the pipes closest to the floor have been around more times than those in pipes closest to the ceiling, and thus have a bigger energy and need stronger bending magnets. The electrons can be extracted by the end of any complete tour, with an energy equal to a multiple (between 1 and 5) of one fifth of the end point energy. Simultaneous distribution to the three end stations is achieved by using properly phased rf deflecting cavities ("rf separators") operating at 499 MHz following the final pass through the accelerator. The main machine parameters are summarized in Table 2.1.

The accelerating cavities are made of pure niobium sheet and plate and have been carefully inspected for surface defects. Cavities were hermetically paired and installed in "cryounits", four of which make up an 8.25 m long, eight cavity "cryomodule". There is a central helium refrigerator, located in the center of the racetrack shaped accelerator, that supplies 2.2K, 2.8 atm helium to cool down

Table 2.1: Main machine parameters (from reference [Lee01]).

Energy	6.06 GeV
Average current (Halls A and C)	1-150 μA
Average current (Hall B)	1-100 nA
Bunch charge	< 0.3 pC
Repetition rate	499 MHz/hall
Beam polarization	$> 75\%$
Beam size (rms transverse)	≈ 80 μm
Bunch length (rms)	300 fs, 90 μm
Energy spread	2.5 x 10^{-5}
Beam power	< 1 MW
Beam loss	$< 1\mu$A
Number of passes	5
Number of accelerating cavities	338
Fundamental mode frequency	1497 MHz
Accelerating cavity effective length	0.5 m
Cells/cavity	5
Average Q_0	4.0 x 10^9
Implemented Q_{ext}	5.6 x 10^6
Cavity impedance (r/Q)	980 Ω
Average cavity accelerating gradient	7.5 MV/m
RF power	< 3.5 kW/cavity
Amplitude control	1.00 x 10^{-4} rms
Phase control	0.1° rms
Cavity operating temperature	2.08 K
Heat load @ 2 K	< 9 W/cavity
Liquefier 2 K cooling power	5 kW
Liquefier operating power	5 MW

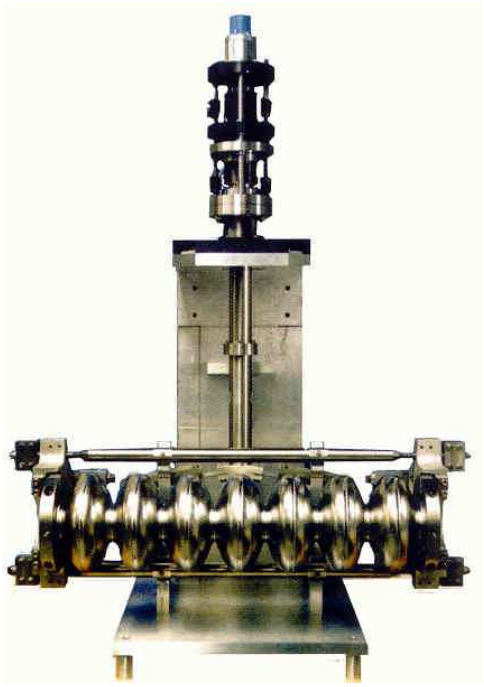

Figure 2.2: The new seven cell cavity design for CEBAF at 12 GeV. The existing cavities have a similar design but only 5 cells.

the cavities.

And last but not least, the whole accelerator operations is controlled and monitored via the EPICS control system (Experimental Physics and Industrial Control System), which enables communication between the machine operators and thousands of devices along the beam line...

2.2 The experimental Hall-B

A schematic view of Hall B is shown in Figure 2.3 taken from reference [Mec03] of which further use shall be made in the rest of this section. Two types of experiments are routinely performed in Hall B: those which use an electron beam and those which use a photon beam. The following subsections will essentially describe the equipment that g7 used, that is the standard photon setting, plus some novelties.

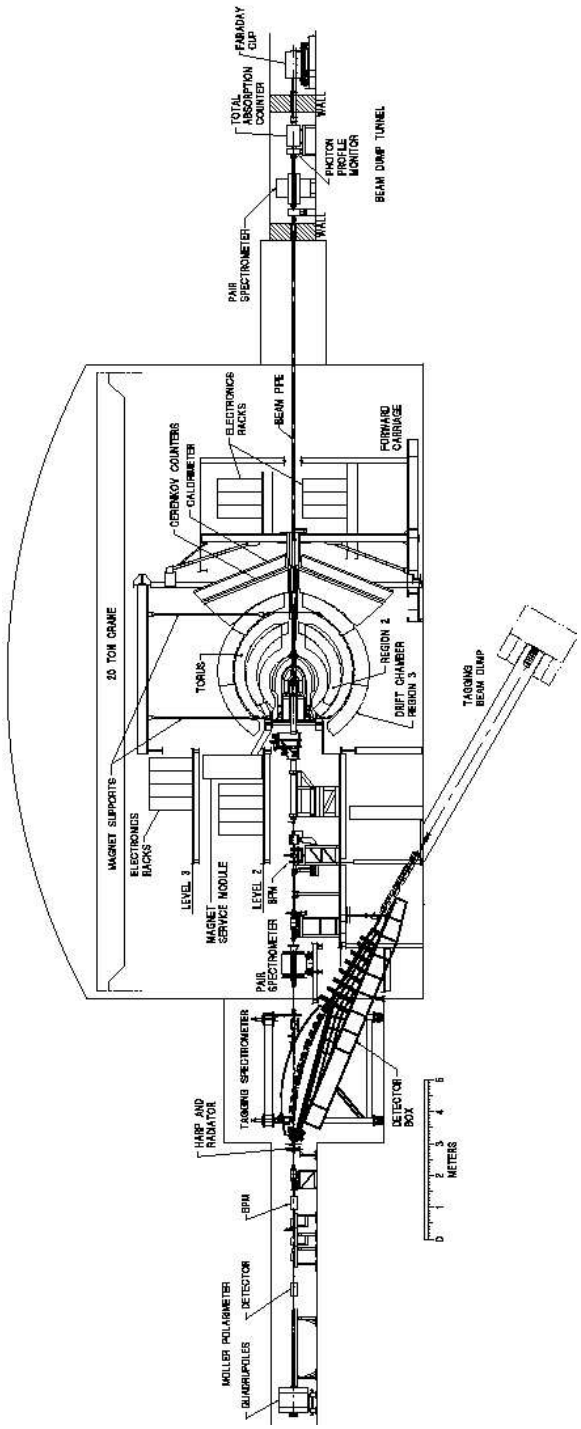

Figure 2.3: Side view of the CLAS detector in Hall B with beam line and associated equipment ([Mec03]).

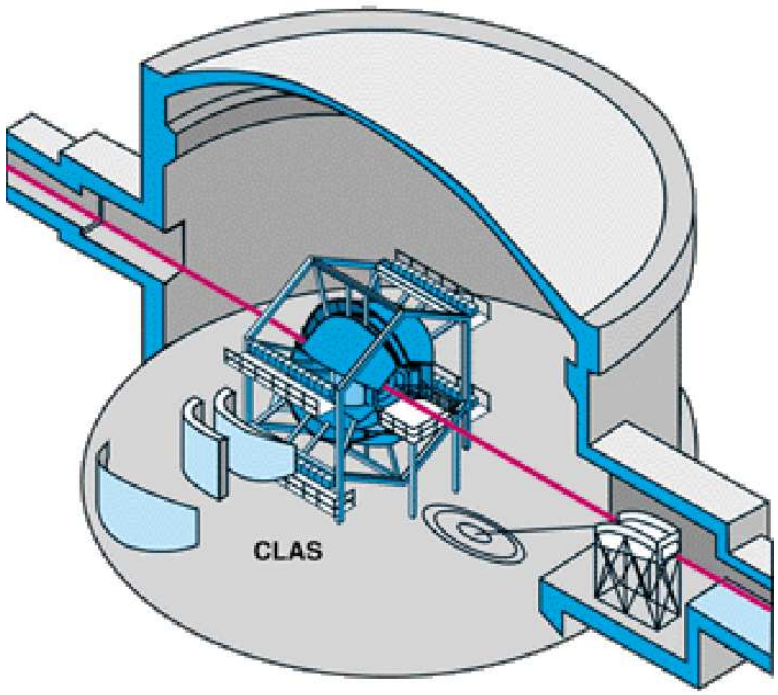

Figure 2.4: Schematic of Hall B. The beam is coming from the bottom right corner on the picture.

2.2.1 The production and tagging of the photon beam

This subsection is dedicated to the description of the way the photons used in the photon run experiments of Hall B are produced and "tagged" (i.e. an energy and a time information is associated to each one of them). More details can be found in [Sob00].

The production of the photon beam

As mentioned already, the CEBAF accelerator delivers an electron beam to the different Halls. The photon beam of Hall B is produced by letting this electron beam go through a thin target, the "radiator", just upstream from a magnetic spectrometer, the "tagger" and radiate. A schematic view of Hall B is given in Figure 2.4.

An electron of the original beam gets decelerated (scattered) by the electro-

magnetic field of a nucleus in the radiator, and in the process emits an energetic photon. The bremsstrahlung radiator target ladder is based on a modification of a HARP design used throughout the CEBAF accelerator as an electron beam position monitor. Thus a standard wire scanner and four radiator targets are mounted on the same ladder assembly. This way, the position of the electron beam can be precisely determined at the exact location where the radiators are to be inserted. Radiators with high atomic numbers were used in order to minimize the effects from electron-electron bremsstrahlung in the spectrum. Several thicknesses of radiator targets, ranging from $1\text{x}10^{-6}$ to $1\text{x}10^{-4}$ radiation lengths are available. Thinner radiators are combination films of gold on a backing of carbon, the thicker ones are free-standing gold films.

The principle of the tagging

The tagger is placed right after the radiator ladder along the beam line and made of a single dipole magnet combined with a hodoscope containing two planar arrays scintillators. It can detect energy-degraded electrons from a thin bremsstrahlung radiator and can thus tag photon energies over a range from 20% to 95% of the incident electron beam energy.

The electrons together with the photons they radiated enter the tagger, which deflects the electrons away from the beam line thanks to its dipole magnet and lets the photon beam continue straight onto the target. This is illustrated in Figure 2.5.

The energy transferred to a radiator nucleus during the deceleration (scattering) of an electron is negligibly small, so the reaction obeys the energy conservation relation

$$E_\gamma = E_0 - E_e \tag{2.1}$$

where E_e is the energy of the outgoing electron and E_γ is the energy of the emitted photon. Since E_0 is uniquely determined by the accelerator, a measurement of the outgoing electron energy by a magnetic spectrometer thus provides a

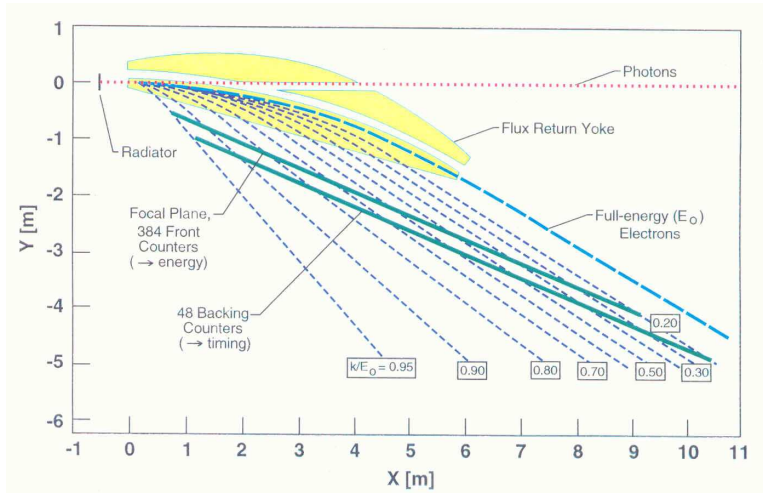

Figure 2.5: Photon beam production and tagging.

determination of the photon energy.

At energies of a few MeV, the outgoing electron and photon emerge at very small angles relative to the incident beam direction. The angular distribution of the photons has a characteristic angle

$$\theta_c = mc^2/E_0 \tag{2.2}$$

where m is the electron rest mass, while the electron's characteristic angle is given by

$$\theta_e = \theta_c E_\gamma / E_e \tag{2.3}$$

At the Jlab energies (usually > 800 MeV for experiments), both of these angles are of the order of 1 mrad or smaller, so that in first approximation, both the photon and the electron are still traveling along the original beam direction at their exit from the radiator.

A collimation system, to further define the photon beam leaving the tagger, is positioned just downstream of the tagger, centered on the photon beamline. This system has two sets of interchangeable collimator sets inserts, with interspaced sweep magnets to clean up any charged particle background generated in the collimator walls.

The tagger magnet

The field setting of the tagger magnet is matched to the incident beam energy so that those electrons which do not radiate will follow a circular arc just inside the curved edge of the pole face, and will be directed into a shielded beam dump below the floor of the experimental hall. Electrons which do give up energy to radiate a photon, experience a greater curvature in the tagger field, and emerge from the magnet somewhere along the straight edge of the pole gap. A scintillator hodoscope along the flat focal plane downstream from this straight edge detects these energy-degraded electrons, and thereby allows for the determination of the energy of the radiated photon. This hodoscope must have adequate segmentation to deliver the desired energy resolution. Its instrumentation must also provide timing information sufficiently precise to allow for correlation with a particular nuclear interaction in the downstream target to within the 2 ns interval between beam "buckets" from the accelerator.

The tagger hodoscope

The hodoscope is made of two scintillator planes. The first plane is called the E-plane and the second plane, the T-plane, where E denotes the energy and T the time. The E-plane contains 384 narrow plastic scintillators called the E-counters to record deflected electron positions in the E-plane, an thus the momenta of those degraded electrons. The E-counters are 20 cm long and 4 mm thick, and with widths (along the dispersion direction) that range from 6 to 18 mm in order to subtend approximately constant momentum interval of $0.003E_0$. Each E-counter optically overlaps its adjacent neighbors by one third of their respective widths, thus creating 767 separate photon energy bins through appropriate recording of coincidences and anti-coincidences, and providing an energy resolution of $0.001E_0$. Light from the scintillators is collected by optical fiber light guides and transmitted to photo-multiplier tubes. The T-plane provides a

timing resolution better than 300 ps with its 61 T-counters, 2 cm thick, read out using phototubes attached by solid light guides at both ends of each scintillator. The T-counter scintillators are organized in two groups, with the first group of 19 narrower counters spanning the photon energy range from 75-95% of the incident electron energy, and the remaining group of 42 counters spanning the range from 20-75%. The T-counter widths (along the dispersion direction) are varied to compensate for the $1/E_{gamma}$ behaviour of the bremstrahlung cross section, so that the rate in each detector remains approximately the same within each group, with the rate in the first group approximately 1/3 of that in the second group. T-counter lengths (transverse to the momentum direction) are also varied from 20 cm at the high electron momentum end to 9 cm at the low momentum end. These lengths were chosen to be large enough to accept ~98% of the electrons from the radiator at $E_0 = 0.8$ GeV.

The tagger electronics

As for the tagger electronics, each of the 122 T-counter photomultiplier signals is fed to one input of a fast (200 MHz) constant-fraction discriminator (Phillips 715). The output of each fast discriminator is then sent to one of four 64-input, 12-bit, multi-hit, FASTBUS TDCs (LRS 1872A), operating in the 50 ps/channel resolution mode. The output of each E-counter photomultiplier tube is fed to a signal-amplifier, discriminator, multiplexer and logic module (ADML). The amplifier discriminator in this module is a Phillips 6816, 16-channel, time-over-threshold unit. The output of each E-counter discriminator is fed to one input of a 96-input, 12-bit, multi-hit, FASTBUS TDC (LRS 1877), running in common-stop mode with a timing resolution of 500 ps/channel. The stop signal is supplied by the CLAS event trigger.

The timing information from the E- and T-counters is used during data analysis to establish the hit patterns and to make tight timing coincidences between the counters. Timing windows of less than 0.5 ns for the T-counters and 3 ns for

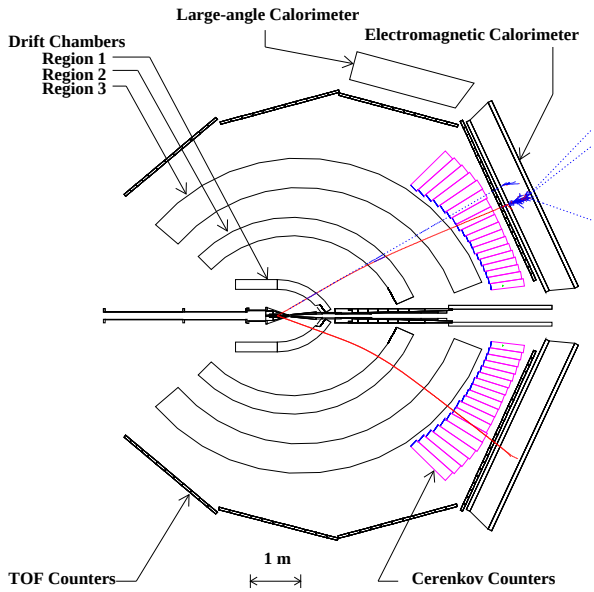

Figure 2.6: The CLAS detector, top view, cut along the beam line ([Mec03]). Typical electron, photon and proton tracks from an interaction are superimposed on the figure.

the E-counters allow software rejection of most background events.

2.2.2 The CLAS detector

The CEBAF Large Acceptance Spectrometer (CLAS) has been operating for intermediate energy electromagnetic physics experiments since December 1997 ([Bro00]). The Table 2.2 (from reference [Mec03]) gives a summary of the detector's design goals. The magnetic field is given by six superconducting coils (main torus), an extra six coil torus of smaller size (mini torus) can be used to get additional field around the target. The detector is otherwise made of 3 regions of drift chambers, time of flight scintillators, Cerenkov counters, electromagnetic calorimeters, and what's called the large angle calorimeters as can be seen in Figure 2.6. A description of these individual components and their specifications will be given in the subsections that follow.

Table 2.2: Summary of the detector design goals ([Mec03]).

Capability	Quantity	Range
Coverage	charged particle angle	$8° \leq \theta \leq 140°$
	charged particle momentum	$0.1 \leq p \leq 4GeV/c$
	photon angle	$8° \leq \theta \leq 45°$
	photon energy	$E_\gamma \geq 0.1GeV$
Resolution	momentum ($\theta \leq 30°$)	$\sigma_p/p \approx 0.5\%$
	momentum ($\theta \geq 30°$)	$\sigma_p/p \approx (1-2)\%$
	polar angle	$\sigma_\theta \approx 1mrad$
	azimuthal angle	$\sigma_\phi \approx 4mrad$
	time (charged particles)	$\sigma_t \approx (100-250)ps$
	photon energy	$\sigma_E/E \approx 10\%/\sqrt{E}$
Particle ID	π/K separation	$p \leq 1.5GeV/c$
	π/p separation	$p \leq 3GeV/c$
	π^- misidentified as e^-	$\leq 10^{-3}$
Luminosity	electron beam	$L \approx 10^{34}cm^{-2}s^{-1}$
	photon beam	$L \approx 5$ x $10^{31}cm^{-2}s^{-1}$
Data acquisition	event rate	1.5 kHz
	data rate	10 MB/s

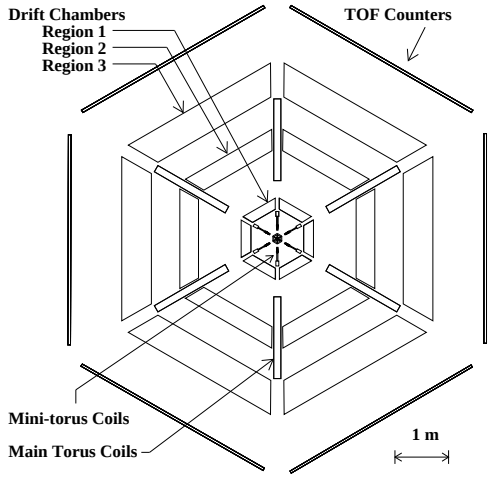

Figure 2.7: The CLAS detector, cut perpendicular to the beam line ([Mec03]).

A conventional spherical coordinate is generally used to describe CLAS. The z-axis is taken to lie along the beam direction, with θ as the polar (scattering) angle, and ϕ as the azimuthal angle. The x and y directions are then respectively horizontal and vertical in the plane normal to the beam.

The CLAS magnetic field

The CEBAF Large Acceptance Spectrometer design is based on a toroidal magnetic field. Primary requirements driving this choice were the ability to measure charged particles at small angles with good momentum resolution, geometrical coverage to large angles in the laboratory, and a magnetic-field-free region around the target to allow the use of polarized targets. A view of the particle detection system normal to the direction of the beam (cut in the target region) can be seen in Figure 2.7. One can see the localization of the main and the mini torus with respect to the rest of the detector components.

The main torus

The main torus generates the primary field for CLAS. It is always present, be it for an electron run or a photon run type of experiment, as it gives the field necessary to do the tracking of charged particles with the drift chambers. The six superconducting coil geometry gives a field pointing primarily in the ϕ-direction. The layout of the coils and the contours of absolute field strengths are shown in Figure 2.8. The Figure 2.9 shows the magnetic field vectors in a plane perpendicular to the torus axis at the target position. The kidney-shape of the coils results in a high field integral for forward-going particles (typically high momentum) , and a lower field integral for particles emitted at larger angles. This geometry also preserves a fields-free region at the center for a polarized target. The maximum design current is 3860A, the total number of turns is $5x10^6$ (summed over all loops). At this current, the integral magnetic field reaches 2.5 Tesla.meter in the forward direction, dropping to 0.6 Tesla.meter at a scattering angle of 90 degrees. Routine operation has been limited to 87% of the maximum current (3375 A) to keep internal mechanical stresses within conservative limits.

Each of the six coils has 4 layers of 54 turns of aluminum-stabilized NbTi/Cu conductor. Cooling of the coils to 4.5 K is accomplished by forcing super-critical helium through cooling tubes located at the edge of the windings. Super-insulation and an intermediate liquid-nitrogen cooled heat shield reduce that heat load. The coils are designed to be self-protecting in case of a quench.

The mini torus

The mini torus is typically not used for photon experiments but used for electron experiments. In this second type of experiments, the beam creates a big amount of low energy electrons by Møller interaction (electron-electron scattering) in the target. An additional magnetic field around the region I of the drift chambers, supplied by the mini torus, is necessary to bend these electrons into the beam pipe. Because the g7 target had high-Z material in it, it was a source of a big amount of low energy electron-positron pairs from photons pair-creating in the electromagnetic field of the target nuclei. This required the use of

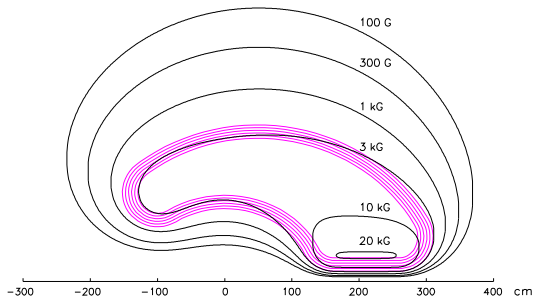

Figure 2.8: Contours of constant absolute magnetic field for the CLAS toroid in the midplane between coils ([Mec03]). The projection of the coils onto the midplane is shown for reference.

the mini torus, contrary to the typical photon experiments. Testing the efficiency of the mini torus in removing these electrons and positrons (i.e. bending them into the beam pipe so that the the region I of the drift chambers does not see them any more) was a big part of the simulations prior to the run. The details of the pre-run simulations can be found in [Tur03].

The mini-torus, just like the main torus, is a toroidal magnet, consisting of six resistive water cooled coils. The maximum current in the magnet is 8000 A. Again, routine operation has been limited to 75% of the maximum current (6000 A) to keep internal mecanical stresses within reasonable limits.

The Drift Chambers

A good source of inspiration for this section was the reference [Mes00]. The reader interested in more detail about the drift chambers, should refer to it.

CLAS was designed to track charged particles with momenta greater than

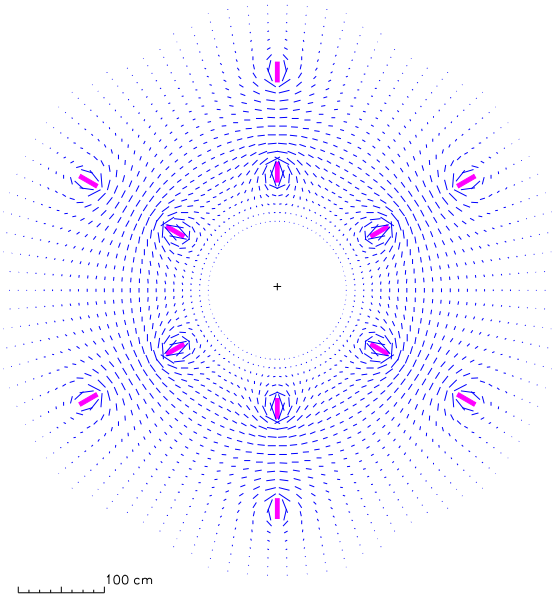

Figure 2.9: Magnetic field vectors for the CLAS toroid transverse to the beam in a plane centered on the target ([Mec03]). The length of each segment is proportional to the field strength at that point. The six coils are seen in cross section.

200 MeV/c over the polar angle range from 8° to 142°, while covering up to 80% of the azimuth. In order to achieve this, it is necessary to reconstruct the trajectories of all charged particles that do not strike the cryostat of the toroidal magnet. All non-active parts of the drift-chamber structure are required to reside in the "shadow" of the torus cryostat as viewed by rays from the target, imposing tight space constraints.

The magnet coils naturally separate the detector into six independent tracking areas or "sectors", since a particle that leaves the target and enters a sector stays within that sector (indeed the CLAS toroidal magnet bends the charged particles towards or away from the beam axis but leaves the azimuthal angle essentially unchanged). To simplify the detector design and construction, 18 separate drift chambers were built and located at three radial locations in each of the six sectors. These radial locations are referred to as "Regions". The "Region One" chambers (R1) surround the target in an area of low magnetic field, the "Region Two" chambers (R2) are somewhat larger and are situated between the magnet coils in an area of high magnetic field near the maximum track sagitta, and the "Region Three" chambers (R3) are the largest devices, radially located outside of the magnet coils.

To optimally fill the wedge-shaped volume between the torus coils, the chamber bodies were designed to support wires running between two endplates, each parallel to its neighboring coil plane, and thus tilted at 60° with respect to each other. This design provides maximum sensitivity to track momenta since the wire direction is approximately perpendicular to the bend plane of the curved trajectories. The wire midpoints are arranged in "layers" of concentric circles. For pattern recognition and tracking, the wire layers are grouped into two "superlayers", one axial to the magnetic field, and the other tilted at 6° stereo angle around the radius of each layer to provide azimuthal information. Each superlayer nominally consists of six layers of drift cells as shown in Figure 2.10.

The wires are shifted by half the nominal position in successive layers. This

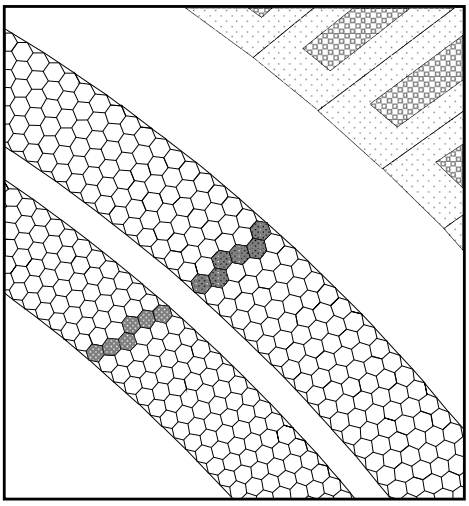

Figure 2.10: Representation of portion of a region III sector of the drift chambers showing the layout of its two superlayers ([Mes00]). The sense wires are at the center of each hexagon and the field wires are at the vertices. The perimeters of the hexagons are shown to outline each cell. Not shown are the guard wires that surround each superlayer. In this view, projected on the mid-plane of the sector, a passing charged particle is shown by the highlighted drift cells that have fired. Beyond the drift chamber, in the upper right corner, the edge of a Cerenkov detector is shown.

"brick-wall" pattern of wires in neighboring layers, with a repeating pattern of two field-wire layers and one sense-wire layer, results in a quasi-hexagonal pattern with six field wires surrounding one sense wire. The cell size increases uniformly with increasing radial distance from the target. A layer of guard wires surrounds the perimeter of each superlayer with high-voltage potential adjusted to reproduce the electric-field configuration given by an infinite grid of hexagonal cells, i.e. the electric field at the sense wire surface is approximately the same for all sense wires, independent of wire-layer number.

The three chamber Regions share many of the same basic design elements. Each is made of six identical wedge-shaped sectors constructed from a pair of long wire-supporting endplates that bear both the load of the wire tensions and the weight of all associated hardware. A representative chamber is shown in Figure 2.11. Each endplate contains thousands of accurately positioned holes into which the wire-fixture assemblies were placed. The sense wire for all chambers consists of 20-μm diameter gold-plated tungsten, the smallest practical choice. Tungsten was chosen because of its durability, and the gold-plating of the wires, amounting to a thickness of 0.127 μm, ensures chemical inertness as well as a smooth surface finish. The electric field at the surface of the sense wires is about 280 kV/cm. The field wire for all chambers consists of 140-μm diameter gold-plated aluminum 5056 alloy. Aluminum was chosen because it has the longest radiation length of any practical wire material and thus minimizes multiple scattering. The main requirements for the chamber gas were that it should have reasonably low multiple scattering, allow for reasonable gas gains, have short collection times in order to reduce the random background expected from Møller electrons and target generated X-rays, and be inexpensive because of the large volume of chambers. Ultimately, a 90% argon-10% CO_2 mixture was chosen for several reasons: the gas has a fairly high saturated drift velocity (> 4 cm/μs), and it has an operating voltage plateau of several hundred volts before breaking down occurs. The mixture additionaly provides good efficiency, adequate

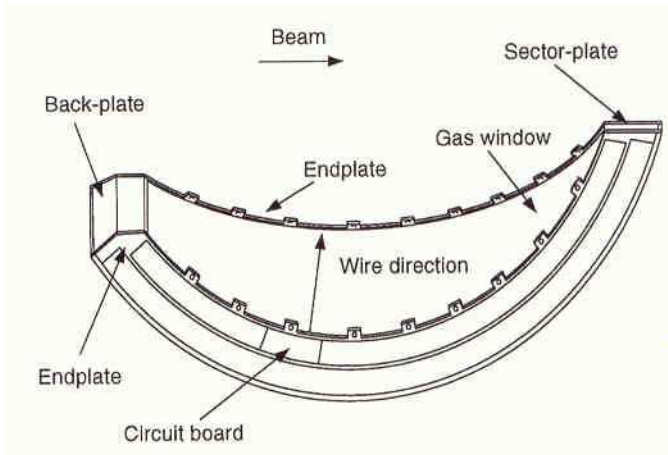

Figure 2.11: Schematic representation of a typical drift chamber sector (here an R3 sector) highlighting some of the common hardware pieces used by each ([Mes00]).

resolution, and resonable collection times. The drift-chamber frames are made primarily of aluminium (R1), fiberglass (R2), or steel-clad structural foam (R3).

R1 consists of six identical sectors integrated into a single unit. Each sector consists of 1296 hexagonal drift cells ranging in diameter from 15 to 17 mm, with all wires located within 1 m of the primary beam. Each sector consists of two superlayers, the stereo layer at smaller radius. This arrangement, which is opposite to the outer two Regions, was necessitated by space constraints within the torus. While each R2 and R3 consists of 12 layers of sense wires, the limited space within the torus allowed for only 10 layers in each R1 sector. The final R1 design included 6 axial layers and four stereo layers.

Each R2 sector contains a total of 2262 hexagonal drift cells ranging in diameter from 26 to 29 mm, with cell size increasing uniformly with wire layer number. The wires are arranged in two superlayers, one axial (at smaller radius) and one stereo (at larger radius). Each of the 12 layers contains between 184 and 192 drift cells. One of the two endplates in each chamber has a 2.54-cm step away from the cryostat to avoid projection that decreases the azimuthal coverage slightly for $\theta \geq 120°$. The hexagonal wire pattern is unaffected by this step.

The R3 chambers were designed and manufactured at Jlab. The shape of each 7-m long sector follows the outer contour of the CLAS torus. The sectors are located outside of the toroid in a field-free region at a distance from the target of between 3.0 and 3.5 m. Each chamber has 2304 hexagonal drift cells ranging in diameter from 40 to 45 mm, with cell size increasing uniformly with layer number. The wires are laid out with the axial superlayer closer to the target. Each of the 12 wire layers contains 192 drift cells.

The tracking resolution is the deviation of the reconstructed momenta and angles of the charged-particle tracks from their true values. Tracking uncertainties arise from three primary sources: multiple scattering in the material along the particle trajectory, geometric misalignments of the separate tracking chambers or lack of knowledge of true value of the traversed magnetic field strength, and the single-wire resolution. The single-wire resolution depends upon where within a cell the track has passed. Within a given layer, this is estimated by fitting a track to all hits except those in that layer. The residual fit is the difference between fitted distance-of-closest-approach (DOCA) of the track and the value of the DOCA calculated from the drift time in the excluded layer. The single-wire resolution worsens near the wire and also at the outer edge of the cell. This arises due to the Poisson distribution of ion-pair production along the path of the primary ion near the sense wire along with time-walk effects and the divergence of the electric field lines near the field wire. The average single-wire resolution in the mid-portion of the cell for each region is about 200 to 250 μm. The whole-cell average is about 310, 315 and 380 μm for R1, R2 and R3, respectively.

The Cerenkov counters

The CLAS Cerenkov gas detector serves the function of triggering on electrons, and separating electrons from pions ([Ada01]). The detector consists of 216 optical modules. Each module consists of three adjustable mirrors of lightweight

composite construction, a Winston light collecting cone, a 5-in, photomultiplier tube, and specially designed magnetic shielding. Its design aims at maximizing the coverage in each of the six sectors up to an angle $\theta = 45°$. This is done by covering as much of the available space as possible with mirrors, and placing the light collecting cones and photomultiplier tubes (PMTs) in the regions of ϕ which are obscured by the magnet coils. Due to the six-fold symmetry of CLAS, the Cerenkov detectors were fabricated as six independent identical detector sectors. Each sector subtends an azimuthal angle (ϕ) of 60° and a zenith (scattering) angle $8° < \theta < 45°$. Each sector was individually assembled. Every one of the six sectors of CLAS was divided into 18 regions of θ, and each θ segment was divided into two modules about the symmetry plane bisecting each sector. This results in a total of 12 identical (except for an inversion symmetry) subsectors around the ϕ direction for each θ interval, and a total of 216 light collection modules.

The optics of each θ module was designed to focus the light onto a PMT associated with that module and located in the region obscured by the coils. Figure 2.12 shows the optical arrangement of two modules. The array of the modules in one sector is shown in Figure 2.13. The optical elements of each module consists of two focusing mirrors, a "Winston" light collection cone, and a cylindrical mirror at the base of the cone as shown in Figure 2.12. The light detection is done by means of a 5-in. Phillips XP4500B PMT mounted at the base of the Winston cone. The trajectory of the light produced by a typical electron through the Cerenkov detector is also illustrated in Figure 2.12. Since the distance between coils increases approximately linearly with θ, each of the 18 modules in θ has unique optical design parameters.

Each detector sector is then filled with $6m^3$ of C_4F_{10} (perfluorobutane) gas, which was chosen for its high index of refraction (n = 1.00153). This results in a high photon yield, and an acceptably high pion momentum threshold of $p_\pi \approx 2.5$ GeV/c. In addition, C_4F_{10} has excellent light transmission properties.

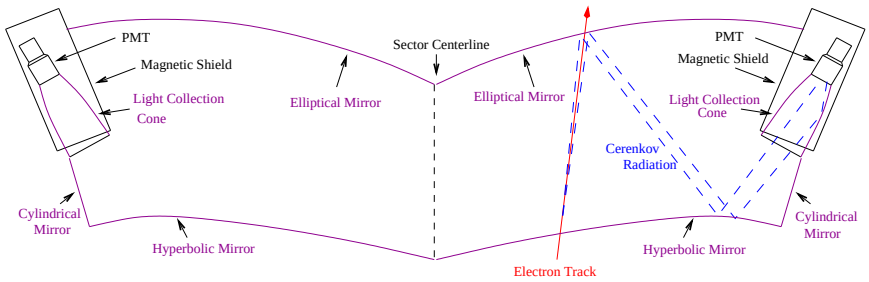

Figure 2.12: Optical arrangement of two of 216 optical modules of the CLAS Cerenkov detector, showing the optical and light collection components.

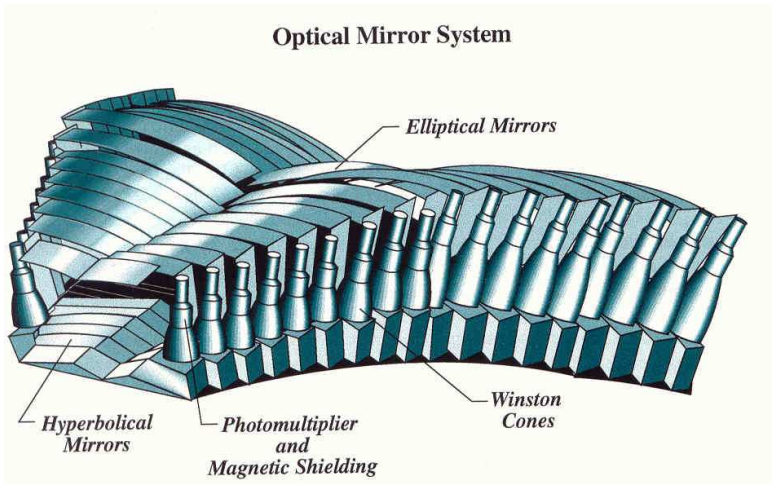

Figure 2.13: Schematic drawing of the array of optical modules in one of the six sectors of CLAS ([Ada01]).

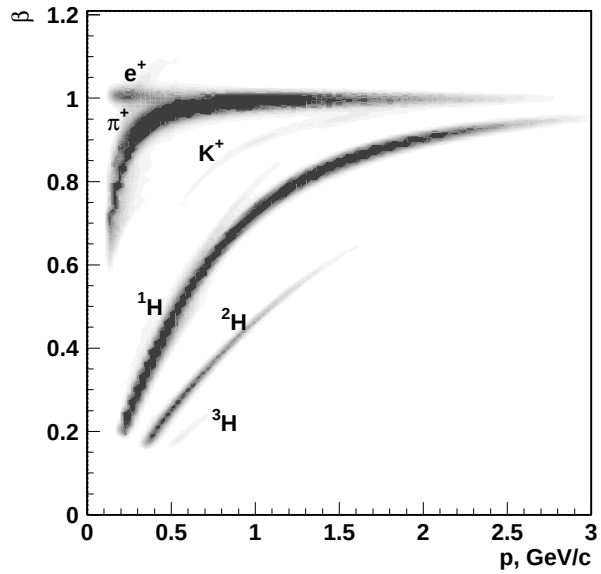

Figure 2.14: Example of β/p plot used to do particle identification.

The measured mirror reflectivity, though typically around 90% in the visible region, drops to about 85% in the near UV, and then typically near 20% at 200 nm, so that light absorption in gas does not play a significant role in the degradation of signal. The physical density of the gas corresponds to about 1 g/cm^2 effective thickness traversed by a typical particle. Except for isolated spots at the midplane, where the gaps between the mirrors are the largest, the electron efficiency within the fiducial acceptance should exceed 99%.

The time of flight scintillators

Particle identification with CLAS mainly uses their time of flight (TOF) information from the time of flight scintillators in correlation with their momenta from the drift chambers (needed to plot a β/p spectrum, see example in Figure 2.14).

The TOF system covers a total area of 206 m^2, representing the range from 8° to 142° in polar angle θ and the entire active range in azimuthal an-

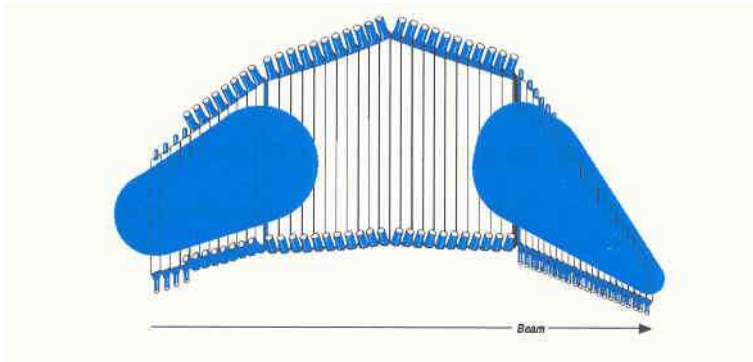

Figure 2.15: Schematic drawing of one sector of the time of flight system.

gle ϕ ([Smi99]). The scintillators are located radially outside the tracking system and the Cerenkov counters but in front of the calorimeters. Their alignment and relative positioning with respect to other detector subsystems can be best seen in Figure 2.6. Just like the other detectors, the TOF is divided into six sectors and each sector is made of four scintillator panels (see Figure 2.15 representing the four panels in a given sector). The scintillator thickness of 5.08 cm is uniform throughout, chosen to give a large signal for traversing minimum-ionizing particles. Each scintillator is placed perpendicular to the average local particle trajectory, such that the width of the counter subtends about 1.5° of scattering angle. The forward counters (at $\theta < 45°$) are 15 cm wide, and the large-angle counters are 22 cm wide, in the $\triangle\theta$ direction. Their lengths vary from 32 to 445 cm. Thus, each sector has 57 scintillators in total with a PMT at each end.

The requirements for the TOF system include excellent timing resolution for particle identification, and good segmentation for flexible triggering and prescaling. The design parameters were chosen to allow separation of pions and kaons up to 2 GeV/c. The most energetic particles are produced at small angles. The system specifications called for a time resolution of $\sigma = 120ps$ at the small angle and $\sigma = 250ps$ at angles above 90°. Particle identification is achieved by off-line analysis that combines leading-edge time measurements with pulse-height information from time-walk corrections. The TOF system is also used for energy-loss

measurements and velocity determination in specific instances. Pulse-height information, being proportional to the energy-loss in the counter, provides an independent means for the identification of slow particles. Also the flight time can provide a more accurate measurement of particle energy than magnetic analysis for slow particles when the tracking resolution is dominated by multiple scattering. The vertex time is determined by the accelerator RF, modulo 2.004 ns. The time of flight information from the TOF counters is essential to the identification of the right RF bucket for the electron run experiments, as it also was for g7.

The Electromagnetic Calorimeters

The last components of CLAS, those radially the farthest from its center, are the Forward Electromagnetic Calorimeter, divided into six sectors, covering the θ range up to 45°, and the Large-Angle Electromagnetic Calorimeter, covering only two azimuthal sectors of CLAS (corresponding to 120° in ϕ) and a range in the scattering angle θ between 45° and 75°. The next two "paragraphs" give more details about each of these detector components.

The Forward Electromagnetic Calorimeter

The main functions of the forward electromagnetic calorimeter (EC) are the detection of and triggering on electrons at energies above 0.5 GeV, detection of photons at energies above 0.2 GeV (for reconstruction of π^0 and η via the measurement of their decay into 2 photons), and the detection of neutrons. Based on requirements of energy and position resolution and large acceptance coverage, a sampling calorimeter made of alternating layers of scintillator strips and lead sheets with a total thickness of 16 radiation lengths was chosen. The lead-scintillator ratio is 0.24, requiring a total thickness of 39 cm of scintillator and 8.4 cm of lead (see Figure 2.16 for a vertical section of an EC module). For more information on the EC, see the reference [Ama01].

Each EC module (representing one sector of the EC), the lead-scintillator sandwich, is contained within a volume having the shape of a nearly equilateral

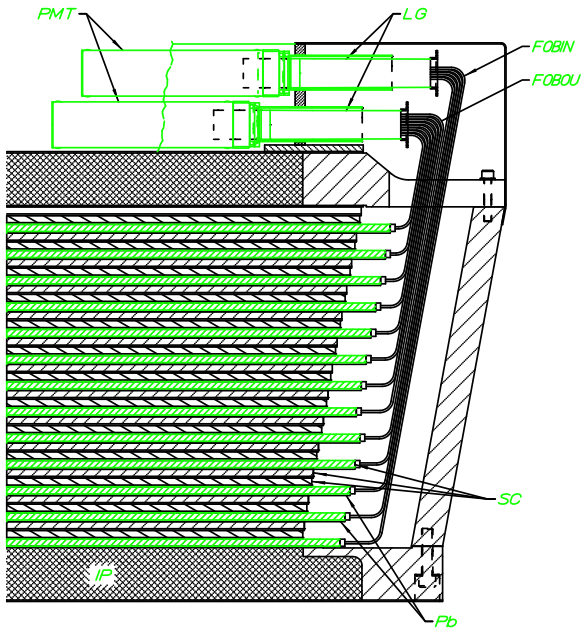

Figure 2.16: Vertical section of a module with its read-out systems: LG=Light Guide, FOBIN=Fiber Optic Bundle INner, FOBOU=Fiber Optic Bundle OUter, SC=scintillator, Pb=2 mm lead sheets, IP=Inner Plate.

triangle. The sandwich has 39 layers, each consisting of a 10-mm thick scintillator followed by a 2.2-mm thick lead sheet. The calorimeter utilizes a "projective" geometry pointing to the nominal target position, i.e. the area of each layer increases linearly with distance. For readout purposes, each scintillator layer consists of 36 strips parallel to one side of the triangle, with the orientation of the strips rotated by 120° in successive layers (Figure 2.17). Thus, there are three orientations, or views (labeled U, V, and W), each containing 13 layers, which provide stereo information on the location of the energy deposition. Each view is further subdivided into an inner (5 layers) and an outer (8 layers) stack, to provide longitudinal sampling of the shower for improved electron/hadron separation. To reconstruct a hit in the EC, energy deposition is required in all three views (U, V, W) of inner or outer layers of a module.

The energy resolution of the EC can be parametrized as

$$\sigma/E = 10.3/\sqrt{E}\% \tag{2.4}$$

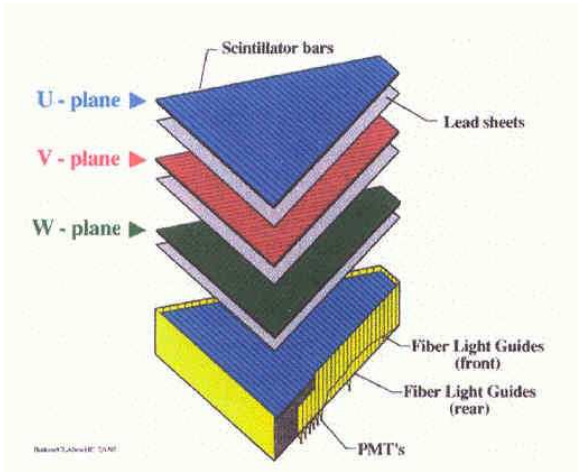

Figure 2.17: Exploded view of one of the six CLAS electromagnetic calorimeter modules ([Mec03]).

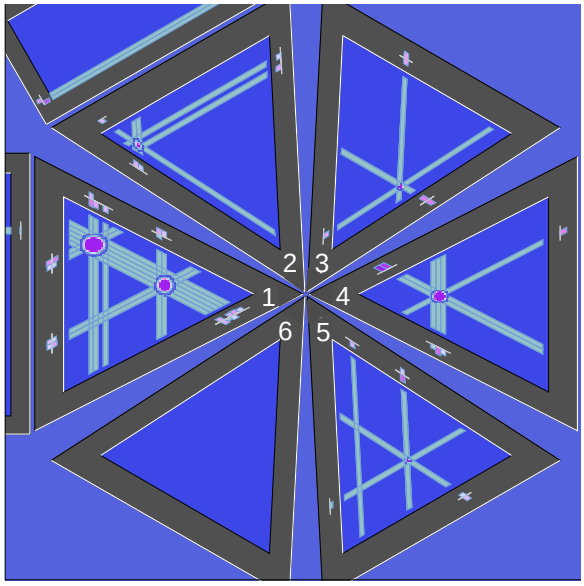

Figure 2.18: Event reconstruction in the electromagnetic calorimeter. In sectors 2, 3, 4, and 5, a single intersection of peaks on each view (U, V, W) is found, while in sector 1, two hits are reconstructed. The size of the oval at each intersection depicts the transverse energy spread in the shower ([Mec03]).

with a negligible constant term, where E is in GeV. The sampling fraction is approximately 0.3 for electrons of 3 GeV and greater, and for smaller energies, there is a monotonic decrease to about 0.25 for electrons of 0.5 GeV. The average rms position resolution for electrons is 2.3 cm for deposited energy greater than 0.5 GeV. The timing resolution for electrons averages 200 ps over the entire detector.

The Large-Angle Electromagnetic Calorimeter

The large angle electromagnetic calorimeter (LAC) enables the detection of scattered electrons and of neutral particles such as neutrons and photons coming from radiative processes or from the decays of π^0 and η mesons.

The LAC is a sampling calorimeter composed of two identical modules with a multi-layer structure of lead sheets and scintillator bars similar to the forward electromagnetic calorimeter. A single LAC module consists of 33 layers, each composed of a 0.2-cm thick lead foil and a 1.5-cm thick NE110A plastic scintillator bar ([Ros96]). The geometry is projective just like for the EC with scintillators of 10-cm average width. Each LAC module corresponds to 12.9 radiation lengths and 1.0 hadronic absorption lengths. To avoid optical coupling, 0.2-mm thick teflon sheets separate neighboring scintillators. Scintillator bars in consecutive layers are rotated by 90° to form a 40 x 24 matrix of roughly 10 x 10 cm^2 cells (see Figure 2.19). To improve the e^-/π^- discrimination, the LAC modules are longitudinally divided into inner (17 layers) and outer (16 layers) regions with individual light readouts.

The light produced by showers in the active material is collected into light guides at each end of a given scintillator bar and then guided into 256 PMTs per LAC module.

The LAC energy resolution for electromagnetic showers can be parametrized as:

$$\sigma(E)/E = (7.5 \pm 0.2)/\sqrt{E}\% \tag{2.5}$$

where E is the energy in GeV. The π^- contamination is less than 1% at a detection

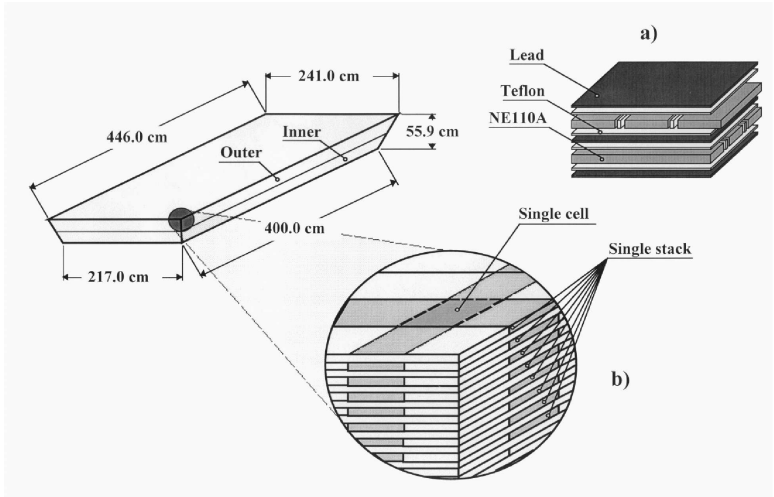

Figure 2.19: Geometry of one LAC module and a schematic view of the lead-scintillator sandwich structure with details a) the calorimeter layers and b) the composition of a stack of scintillators that are read out ([Mec03]).

efficiency of 95% for 2 GeV electrons. A good timing resolution for the LAC is essential to determine the momentum of neutrons via the TOF scintilators. For neutron detection, efficiencies greater than 30%, a time resolution of 260 ps was obtained for momenta higher than 0.5 GeV/c. Requiring $\beta_{neutral} \leq 0.95$ enables separation of neutrons from photons.

The triggering with CLAS

The detectors that use PMTs to generate electronic signals record signal times using LeCroy FASTBUS 1872A TDCs (Time to Digital Converters) and signal amplitudes (that give the energy deposited in each detector) using LeCroy 1881M ADCs (Analog to Digital Converters). Most TDCs are fed from leading-edge LeCroy 2313 CAMAC discriminators set at a low threshold, typically 20 mV. The PMT signals are processed through a pipelined memory lookup by the Level 1 trigger within 90 ns. There is an additional Level 2 trigger and finally a trigger supervisor which decides to record or not a given event based on information from the Level 1 and Level 2 triggers.

The underlying idea of the Level 1 trigger is to use all available prompt

information from the PMT channels to determine if a desired event has occurred. This information includes the general location of hits in the TOF detector, the signals in the Cerenkov detector and the energy deposited in the electromagnetic calorimeter. Bit patterns from these detector subsystems are compared against patterns preloaded in memory tables for rapid response.

However, the Level 1 trigger can be set by events such as cosmic rays that lack matching particle trajectories in the drift chamber system. In order to reject triggers arising from those events, the Level 2 trigger finds "likely tracks" in each sector, optionally performs a correlation with the Level 1 trigger, and generates a "Level 2 Fail" signal if no correlated tracks are found. While Level 1 does practically not contribute to the deadtime of the detector, Level 2 has a direct contribution to it and so the goal in designing it was to make it as fast as possible and at the same time consistent with accurately finding tracks. Identifying "likely tracks" begins by finding track segments in five superlayers in each sector (the Region I stereo superlayer is not used). Track segments are found by comparing drift chamber hits with nine templates that were designed to catch all tracks passing through a superlayer at angles of up to 60°. In the present implementation, a "likely track" in a sector is tagged when track segments are found in three of the five superlayers. The Level 2 trigger is satisfied by either the simple logic "OR" of these six sector tracks, or by requiring additional correlations between these tracks and the information from Level 1.

The trigger supervisor is a custom electronics board that takes the Level 1 and Level 2 inputs from the trigger system and produces all common signals, busy gates and resets required by the detector electronics, and controls the readout.

The data acquisition

The CLAS data acquisition (DAQ) system was designed for an event rate of 1.5 kHz. During the period of CLAS commissioning in 1997, the actual rate was 400 Hz ([Mec03]). Continued development of the DAQ over five years resulted in

routine operation at event rates between 3 and 4 kHz for the 2000-2001 running period. At present, the limit for the total data output rate is 25 MByte/s, constrained not by experimental hardware, but by the current use of the Unix file system.

The data from the different detector components are digitized in 24 FASTBUS and VME crates within the experimental hall and collected by the 24 VME ReadOut Controllers (ROC1 to ROC24) in these crates. The arrays of digitized values associated with electronic modules are then translated into tables in which each data value (up to 16 bits) is associated with a unique identity number describing the active component within the detector.

These data arrays, or event fragments, are then buffered and sent in bunches via fast Ethernet lines to the CLAS online acquisition computer (CLON10) in the control room. Three primary processes, the Event Builder (EB), the Event Transport (ET) and the event recorder (ER), comprise the main dataflow elements in the acquisition computer. The Event Builder (EB) on CLON10 assembles the incoming fragments into complete events. The individual tables are prefixed by headers to form "banks" that contain alphanumeric names that can be linked together. The completed event is then labeled by run and event number, event type, and trigger bits that are all contained in a header bank. At this stage, the event has the final format it needs for off-line analysis.

The EB passes the completed events to shared memory (ET1) on the CLAS online computer. The Event Transport (ET) system manages this shared memory, allowing access by various event producer and consumer processes on the same or remote processor systems. The Event Recorder (ER) picks up all events for permanent storage. Some events are transferred to remote ET systems for raw data checks, such as hit maps, status and events display, and for online reconstruction, analysis, and monitoring.

The ER writes the data in a single stream to magnetic media. The output files are striped across an array of local RAID disks. A second fiber link, from

the local RAID in the control room to the computer center a kilometer away, transfers the data files to the remote tape silo. Since the maximum tape writing speed at present is 10 MBytes/s, data transfers may be started in parallel, and successive files may end up on different tapes.

2.2.3 The photon beam flux

The absolute photon flux is determined at very low flux rates by inserting a large lead-glass Total Absorption Shower Counter (TASC) into the photon beam. The TASC is essentially 100% efficient and can only be operated at beam currents up to 100 pA, and has to be retracted from the beam line under normal running conditions. Thus, secondary monitors, with absolute efficiency of only a few percent, but sensitive to any variation in flux, have to be cross-calibrated against the TASC at low rates and then used to monitor the flux at higher intensities.

The g7 experiment made use of the Pair Spectrometer as a beam flux monitor for its normal runs, operated with a thin conversion foil in front of it and itself situated in front of the CLAS target (it used to be situated 22 m behind CLAS previously). By operating the entire system in vacuum, and by using the thin pair-conversion foil that removes less than 1% of the photons from the beam, it is possible to monitor the photon flux even at high flux rates with the pair spectrometer.

2.3 The g7 target

Since the goal of the g7 experiment is to study the effect of nuclear density on the properties of vector mesons, the ideal target is one that contains materials with different average densities (increasing A). This was the main idea behind the design of the target.

The g7 target, contained a liquid deuterium (LD_2) cell of 6.2 cm in length and of about 3 cm in diameter, and seven solid foils, each with a 1.2 cm diameter.

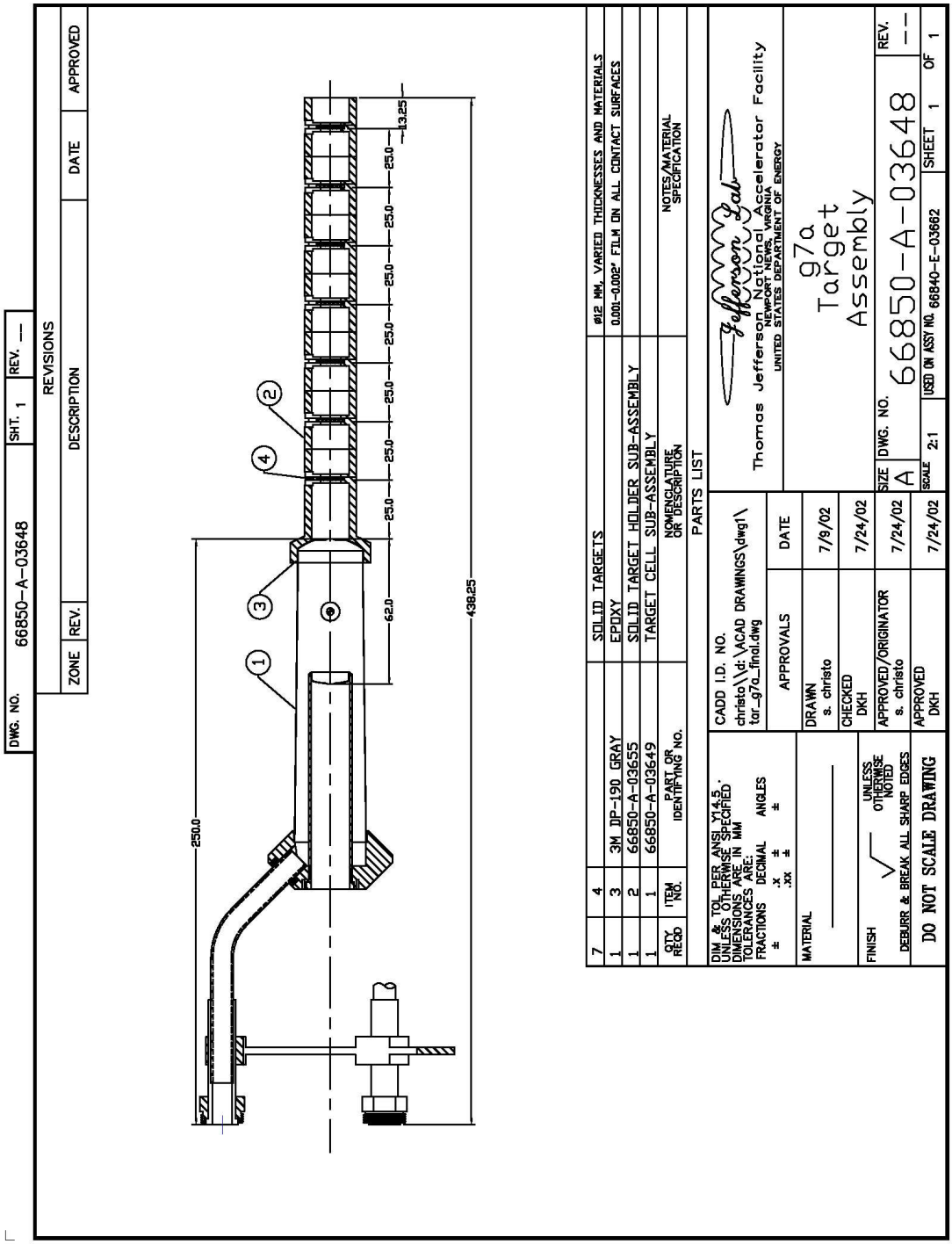

Figure 2.20: A drawing of the g7 target.

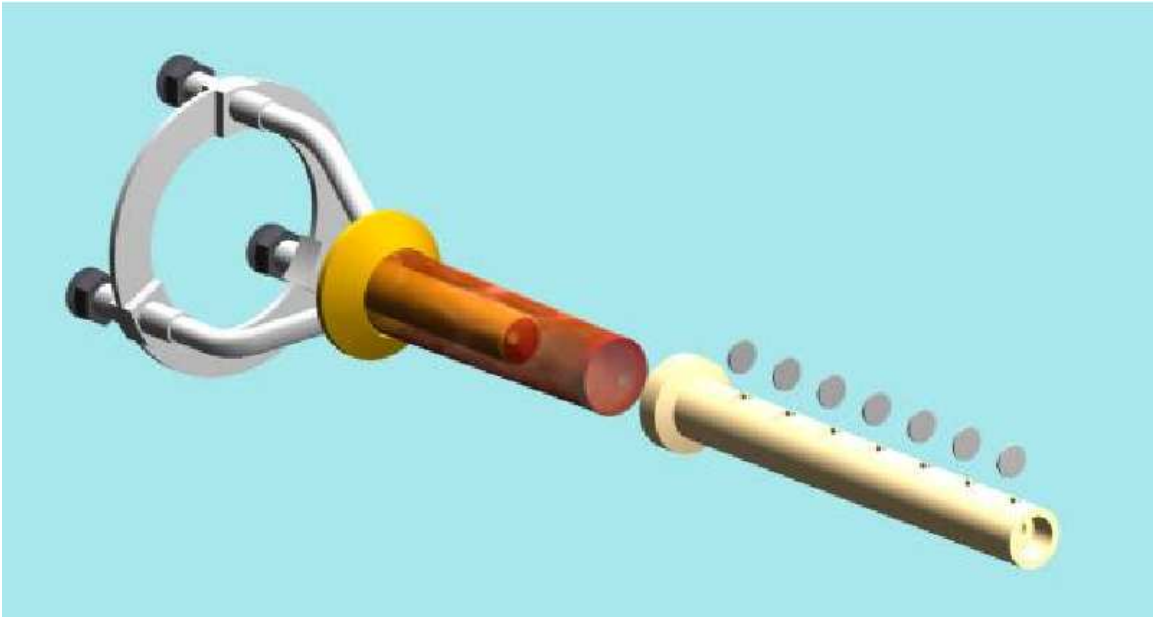

Figure 2.21: g7 target cell with solid target holder.

The ordering of the various targets as seen in Figures 2.20 and 2.21 (from left to right) was the following: LD_2, carbon (C1), iron (Fe), carbon (C2), lead (Pb), carbon (C3), titanium (Ti), carbon (C4). The thicknesses of the solid foils were: 1.5 mm (C1), 0.6 mm (Fe), 1.5 mm (C2), 1 mm (Pb), 1.5 mm (C3), 1 mm (Ti) and 1.5 mm (C4). The total amount of each material was chosen to be as close as possible to 1 g/cm^2, an amount seen as reasonable to get sufficient counts for the three vector mesons being studied in a fair amount of running time according to simulations done before the 1994 proposal ([Ber94]). The distance between the LD_2 cell and the first carbon foil was chosen to be 2.5 cm and the spacing between each two successive solid foils was 2.5 cm as well.

In order to minimize the multiple scattering of the emerging e^+e^- pairs inside the target, one needs to separate the individual targets as much as possible from each other and at the same time decrease their diameter. The idea is that an e^+ or an e^- emerging from one target should not hit the following target before being detected by CLAS. A diameter of 1.2 cm for the actual target was about as low as one could go given the fact the heavily collimated photon beam for

g7, would have ended by having a diameter of 1 cm by the time it would have reached the target. It was essential to have the full beam on the target given the low statistics expected for the experiment. And a separation of 2.5 cm between the individual targets was about as wide as one could go if one wanted the target and scattering chamber to fit inside the mini torus.

The deuterium is used as a reference. Since it is such a small nucleus, one expects most of the ρ mesons produced on the neutron or the proton to decay outside of the nucleus. On the other hand, for the carbon, iron or lead, most of the rho should be decaying inside (especially for the iron and lead), so that, by comparing the invariant mass spectra of the e^+e^- pairs from the heavy nuclei to the one from the deuterium, one might see changes to the width or peak position of the vector mesons, in case they do occur. The choice of the liquid deuterium instead of liquid hydrogen is due to a twofold argument: In the first place, the deuterium has contributions from both the proton and the neutron, and so, it has some Fermi motion inside while having almost "no nuclear density". Secondly, the same amount of liquid deuterium takes less space than liquid hydrogen, and lets enough space in the scattering chamber to put the other solid foils and separate them sufficiently to avoid multiple scattering effects.

Chapter 3

The event generator

The events fed into GSIM, a GEANT 3 simulation package for the CLAS detector, to simulate the g7 experiment were generated using a code based on a semiclassical Botzmann-Uehling-Uhlenbeck (BUU) transport model. The code has been developed over many years by U. Mosel and his numerous students at the Institute for Theoretical Physics (University of Giessen). Originally written to describe heavy-ion collisions at SIS energies ([Tei97], [Wol93]), it has been further extended to also investigate inclusive particle production in heavy-ion collisions of up to 200A GeV and π- ([Eff99a]) and p-induced as well as photon- and electron-induced reactions in the resonance region ([Eff97], [Leh00]) with the very same physical input. The model is rather complete in its inclusion of the various nuclear effects: the shadowing of the photon-induced reactions, the Fermi motion of the nucleons, the Pauli blocking of the outcoming fermionic states, the mean field potential inside the nucleus, the Coulomb potential felt by the charged particles and the final state interactions (FSI) of the particles produced during the initial interaction are all carefully integrated. A collisional broadening of the width of the produced resonances is equally present (the code allows one to use

the vacuum widths, but that is usually not done since the lifetime of any particle state is necessarily reduced in the medium do to collisions and hence its width is broadened). It is possible to also incorporate at will additional medium effects such as a dropping of the mass of the vector mesons according to the Brown-Rho scaling and investigate the consequences of such effects. In the following sections, a detailed description of the BUU model and its implementation into the present code, as well as the specifics of the treatment of the reactions relevant to the g7 experiment will be given.

3.1 The coupled channel semiclassical BUU transport model

The content of this section is based on information that can be found in the references [Eff00], [Fal02], [Leh00], [Mue02], and [Tei97]. The gist of that information will be presented here, but, the reader is highly recommended to refer to the original papers for a different insight.

3.1.1 The BUU equation

The BUU equation describes the classical time evolution of a many-particle system under the influence of a self-consistent mean-field potential and a collision term that takes into account the Pauli principle. More precisely, it gives the evolution in time of the one-particle phase-space density $f(\vec{r}, \vec{p}, t)$. For the description of a system of particles with continuous mass spectra, the classical equation is extended by defining the spectral phase-space density as the product of the ordinary phase-space density f and the particle spectral function S:

$$F(\vec{r}, \vec{p}, \mu, t) = f(\vec{r}, \vec{p}, t) S(\vec{r}, \vec{p}, \mu, t), \tag{3.1}$$

where $\vec{r}$ and $\vec{p}$ are the spatial and momentum coordinates of the particle and μ denotes its invariant mass. The set of transport equations of a system of N

particles is then given by:

$$(\partial_t + \partial_{\vec{p}}\mathcal{H}_i\partial_{\vec{r}} - \partial_{\vec{r}}\mathcal{H}_i\partial_{\vec{p}})F_i = I_i[F_1, ..., F_N], i = 1, ..., N, \tag{3.2}$$

where $I_i[F_1, ..., F_N]$ denotes the collision term, which now also contains the spectral information of the particle. $\mathcal{H}_i = \mathcal{H}_i(\vec{r}, \vec{p}, \mu, F_1, ..., F_N)$ is the single-particle mean-field Hamilton function given by the relativistic expression for the single-particle energy:

$$\mathcal{H}_i = \sqrt{(\mu_i + U_i)^2 + \vec{p}^2}, \tag{3.3}$$

with U_i denoting the effective mean-field potential $U_i(\vec{r}, \vec{p}, \mu, F_1, ..., F_N)$. The equation (3.2) is called the coupled channel Boltzmann-Uehling-Uhlenbeck(BUU) equation (also known as the Vlassov-Uehling-Uhlenbeck, Boltzmann-Nordheim or Landau-Vlassov equation). Its left hand side is called the Vlassov equation and its right side is the collision integral which describes changes to the spectral function due to collisions and incorporates the Pauli-blocking of the final nucleon states. Once the equation (3.2) is solved and the expression of the spectral phase-space density is at hand, the particle yields are calculated, at a fixed time t, using: $N_i = \int d^3r \int d^3p \int F_i(\vec{r}, \vec{p}, \mu, t)d\mu$. More detail on the ingredients of equation (3.2) and a sketch of the method to solve it will be presented in the subsequent sections.

3.1.2 The collision term

The collision term (i.e. the right hand side of equation (3.2)) describes the time evolution of the spectral phase-space density $F(\vec{r}, \vec{p}, \mu, t)$ due to two-body collisions in the nucleus. It can be decomposed into a gain and a loss term. In an obvious notation the collision term then reads:

$$I_i(\vec{r}, \vec{p}, \mu, F_1, ..., F_N) = G_iS_i(1 \pm f_i) - L_iF_i, \tag{3.4}$$

where the upper sign in the parenthesis of the right hand side holds for bosons and the lower sign for fermions. In the latter case, it is there to account for the Pauli principle. The gain term accounts for the creation of particles of the type i

in the phase-space element with coordinates $(\vec{r}, \vec{p}, \mu)$ due to all kinds of collisions with particles of type i in the final state. One can write the general expression for G_i in terms of cross sections by neglecting n-body collisions ($n \geq 3$). This expression then reads:

$$G_i = (2\pi)^3 \sum_{1,2} \sum_X \int \frac{d^3p_1 d\mu_1}{(2\pi)^3} \frac{d^3p_2 d\mu_2}{(2\pi)^3} v_{12} F_1 F_2 (\frac{d^3\sigma}{dp_i{}^3})_{12\to iX} (1 \pm f_3)...(1 \pm f_m), \quad (3.5)$$

where v_{12} is the relative velocity of the colliding particles 1 and 2, and X denotes a final state consisting of the particles 3,...,m. The loss term accounts for annihilation of particles of type i and can be written in the following way:

$$L_i = \Gamma^*{}_{i\to X} + \sum_2 \rho_2 [\sum_X v_{i2} \sigma_{i2\to X} (1 \pm f_3)...(1 \pm f_m)], \quad (3.6)$$

where $\Gamma^*{}_{i\to X}$ denotes the total decay width of the particles of species i including medium corrections, i.e. Pauli blocking / Bose enhancement of the final state. ρ_2 is the spatial density of the particles of species 2 and v_{i2} is again the relative velocity of the incoming particles. The square brackets have to be understood as an average over the momentum distribution of particles of species 2. The second term of expression (3.6) has the general form of a collision width arising from two-body collisions of particle species i and 2.

3.1.3 The treatment of high energy baryon-baryon and meson-baryon collisions

For invariant energies $\sqrt{s} > 2.6$ GeV for the baryon-baryon collisions and $\sqrt{s} > 2.2$ GeV for meson-baryon collisions, the Lund string fragmentation model FRITIOF is used. In the FRITIOF model, particle production occurs as a two step process. First, two excited states with the quantum numbers of the incoming hadrons are produced (string excitation). In the second step, these strings fragment into observable hadrons (fragmentation). In the case of photoproduction, since the FRITIOF model does not accept photons in the entrance channel,

the vector dominance model is used to write the incoming photon as:

$$|\gamma >= (1 - \sum_{V=\rho,\omega,\phi} \frac{e^2}{2g_V^2})|\gamma_0 > + \sum_{V=\rho,\omega,\phi} \frac{e}{g_V}|V >, \tag{3.7}$$

and pass the photon as a massless ρ^0, ω, or ϕ (denoted V for vector meson in equation (3.7)) with a probability corresponding to the strength of the vector meson coupling to the photon times its nucleonic cross section σ_{VN}:

$$P(V) = \frac{(e/g_V)^2 \sigma_{VN}}{\sigma_{\gamma N}}. \tag{3.8}$$

The FRITIOF model gives a good description of inclusive particle production for elementary hadronic reactions. However, one does not get an equally good description of elastic processes. Therefore elastic vector meson production as well as exclusive strangeness production are treated independently of the FRITIOF model.

3.1.4 The test-particle method

The Coupled Channel BUU equations (3.2) (later denoted CBUU) are solved by means of the test-particle method. Let us take the case of particles with a well-defined mass. Then, the CBUU equations simply describe the time evolution of the one-particle phase-space density f. In the test-particle method, f is represented by a sum over δ-functions:

$$f(\vec{r}, \vec{p}, t) = \frac{1}{N} \sum_{i=1}^{N \times A} \delta(\vec{r} - \vec{r}_i(t)) \times \delta(\vec{p} - \vec{p}_i(t)). \tag{3.9}$$

Here N denotes the number of test-particles per nucleon, while A is the total number of nucleons participating in the reaction. Inserting the ansatz (3.9) into the CBUU equations (3.2) leads to the following equations of motion for the test particles:

$$\frac{d\vec{r}_i(t)}{dt} = \frac{\vec{p}}{E} + \frac{m^*}{E} \nabla_p U(\vec{r}_i, \vec{p}_i(t)) \tag{3.10}$$

$$\frac{d\vec{p}_i(t)}{dt} = -\frac{m^*}{E} \nabla_r U(\vec{r}_i, \vec{p}_i(t)), \tag{3.11}$$

where $m^*(\vec{r},\vec{p}) = \mu + U(\vec{r},\vec{p})$ and $E = \sqrt{m^*(\vec{r},\vec{p})^2 + p^2}$. Thus the solution of the CBUU equations within the test-particle method reduces to the time evolution of a system of classical point particles according to equations (3.10) and (3.11). For the actual numerical simulation, the time t is discretized and the equations of motion are integrated using a predictor-corrector method.

3.1.5 The mean-field potential

Particles propagating inside nuclear matter are exposed to the mean-field potential generated by all other particles. This mean field potential, denoted as U in the previous section, is related to a non-relativistic potential U^{nr} expressed in the local rest frame of nuclear matter by:

$$\sqrt{(\mu + U(\vec{r},\vec{p}))^2 + \vec{p}^2} = \sqrt{\vec{p}^2 + \mu^2} + U^{nr}(\vec{r},\vec{p}), \tag{3.12}$$

with U^{nr} defined for the nucleon and nucleon resonances with spin 1/2 as:

$$U^{nr}(\rho(r),\vec{p}) = A\frac{\rho}{\rho_0} + B(\frac{\rho}{\rho_0})^\tau + \frac{2C}{\rho_0}\sum_{I,S}\int \frac{d^3p'}{(2\pi)^3}\frac{f(\vec{r},\vec{p'})}{1+(\frac{\vec{p}-\vec{p'}}{\Lambda})^2}. \tag{3.13}$$

The nucleon phase space density f_N is given in coordinate space by a Woods-Saxon distribution: $\rho(r) = \rho_0(1+exp\frac{r-r_0}{\alpha})^{-1}$. I and S denote the isospin and spin respectively. The summation yields a factor 4 for the nucleon. The parameters r_0 and α are fitted to experimental data for each nucleus type. A, B and τ are fitted to the binding energy, saturation energy, and compressibility respectively. Λ is taken to be 2.13 fm^{-1}. The integral over the phase-space distribution function in equation (3.13) can be performed analytically by using $f(\vec{r},\vec{p}) = \Theta(p_F - p)$, with the local Fermi momentum given by: $p_F(r) = (\frac{3}{2}\pi^2\rho(r))^{\frac{1}{3}}$.

3.1.6 The Coulomb potential

Charged baryons and mesons are additionally exposed to the Coulomb potential $V_c(\vec{r})$ generated by all charged particles. This represents an additional

force in the equations of motion (3.10) and (3.11) for the charged mesons and baryons given by: $\vec{F}_c(\vec{r}) = -q\nabla_r V_c(\vec{r})$. The Coulomb potential $V_c(\vec{r})$ is obtained by solving the Poisson equation by means of the *Alternating-Direction Implicit Iterative* (ADI-) algorithm. At center of mass energies of a a few GeVs the Coulomb contribution is usually neglected.

3.1.7 The treatment of the shadowing of photon-induced reactions

The photon-induced reactions are known to be shadowed (i.e. $\sigma_{\gamma A} < A\sigma_{\gamma N}$) above photon energies of approximately 1 GeV ([Fal02]). In naive words, what happens is that the nucleons on the front side of the nucleus shadow or hide the downstream nucleons. This shadowing in photoproduction is taken into account in a straightforward way in the Glauber theory, customarily used to model the final state interactions (FSI) considered purely absorptive. A more realistic description of the FSI has to also take into account the regeneration of the mesons studied. The coupled channel semiclassical transport model based on the BUU equations that is used in the present code does exactly this. How precisely to transpose the formulation of the shadowing from the simple Glauber theory to the more complex CBUU model will be presented in the text that immediately unfolds. As explained in the section 3.1.3, the Lund Model FRITIOF is used for high-energy photoproduction (to which the following explanations are limited), where the photon has to be passed as a massless ρ^0, ω, or ϕ with a probability given in (3.8) following the vector meson dominance (VMD) picture in which the incoming photon state can be written according to equation (3.7). Using this equation and the optical theorem, one gets the following expression for the γN cross section:

$$\sigma_{\gamma N} = (1 - \sum_{V=\rho,\omega,\phi} \frac{e^2}{2g_V^2})^2 \sigma_{\gamma_0 N} + \sum_{V=\rho,\omega,\phi} (\frac{e}{g_V})^2 \sigma_{VN}. \tag{3.14}$$

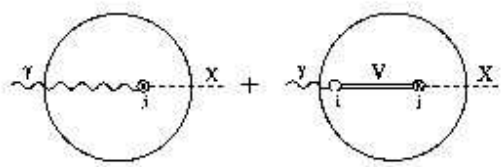

Figure 3.1: The two amplitudes of order α_{em} that contribute to the incoherent meson production in the simple Glauber theory. The left amplitude alone would lead to an unshadowed cross section. Its interference with the right amplitude gives rise to shadowing (figure taken from reference [Fal02]).

As can be seen from equation (3.14), there is also a finite probability for the "bare" photon to be passed to FRITIOF, given by:

$$P(\gamma_0) = 1 - \sum_{V=\rho,\omega,\phi} P(V). \tag{3.15}$$

The component γ_0 does not get shadowed in the nucleus. In a generalized VMD model, for example, the γ_0 includes contributions from heavy intermediate hadronic states, which are not shadowed because of the large momentum transfer q_V that is needed to put them on their mass shell. Since FRITIOF does not accept a "bare" photon as input, the latter is again replaced by a vector meson $V(= \rho, \omega$ or $\phi)$, with the probability:

$$P_{\gamma_0}(V) = \frac{(e/g_V)^2 \sigma_{VN}}{\sum_{V'=\rho,\omega,\phi}(e/g_{V'})^2 \sigma_{V'N}}. \tag{3.16}$$

Up to now no shadowing was taken into account. In Glauber theory this corresponds to using only the left amplitude in Figure 3.1, where a photon directly produces some hadron X at nucleon j. The left amplitude alone leads to the unshadowed cross section (using cylindrical coordinates $\vec{r} = (\vec{b}, z)$):

$$\sigma^{unshadowed}_{\gamma A \to X A^*} = \sigma_{\gamma N \to XN} \int d^2b \int dz_j \tilde{n}(\vec{b}, z_j) \times exp(-\sigma_{XN} \int_{z_j}^{\infty} dz n(\vec{b}, z)), \tag{3.17}$$

where $n(\vec{r})$ denotes the nucleon number density, $\tilde{n}(\vec{r})$ the number density of nucleons with the correct charge to produce the hadron X, and σ_{XN} is the total XN cross section. The exponential damping factor describes the absorption of

the particle X on its way out of the nucleus. In Glauber theory, shadowing arises from the interference of the left amplitude in Figure 3.1 with the second amplitude of order α_{em}, which is shown on the right hand side. In this process the photon produces a vector meson V on nucleon i without excitation of the nucleus. This vector meson then scatters at fixed impact parameter $\vec{b}$ (eikonal approximation) through the nucleus to nucleon j and produces the final state meson X, leaving the nucleus in the same excited state as in the direct process. The incoherent vector meson cross section, this time taking into account the shadowing, is given in Glauber theory by:

$$\sigma_{\gamma A \to VA^*} = \sigma_{\gamma N \to VN} \int d^2b \int_{-\infty}^{\infty} dz_j n(\vec{b}, z_j)$$
$$\times exp(-\sigma_{VN} \int_{z_j}^{\infty} dz n(\vec{b}, z)) \times |1 - \overline{\Gamma_V}(\vec{r_j})|^2, \tag{3.18}$$

with the nuclear profile function containing the shadowing given by:

$$\overline{\Gamma_V}(\vec{b}, z_j) = \int_{-\infty}^{z_j} dz_i n(\vec{b}, z_i) \frac{\sigma_{VN}}{2} (1 - i\alpha_V) e^{iq_V(z_i - z_j)}$$

$$\times exp\{-\frac{1}{2}\sigma_{VN}(1 - i\alpha_V) \int_{z_i}^{z_j} dz n(\vec{b}, z)\}. \tag{3.19}$$

α_V is the ratio of the real to the imaginary part of the VN forward scattering amplitude. The momentum transfer $q_V \approx m_V^2/2E_\gamma$ arises from putting the vector meson on its mass shell. One clearly sees from equation (3.18) how the FSI separate from the "initial state interactions" of the photon. Then the exponential dumping factor $exp(-\sigma_{VN} \int_{z_j}^{\infty} dz n(\vec{b}, z))$, which corresponds to a purely absorptive FSI, is replaced by a transport model to incorporate a wider class of FSI. To include events where the final vector meson V is not produced in the primary reaction, but via sidefeeding, one needs to use the Glauber theory to calculate how the single V components of the photon change due to multiple scattering on the way to the nucleon j where the state X is produced:

$$\sigma_{\gamma N} = (1 - \sum_{V=\rho,\omega,\phi} \frac{e^2}{2g_V^2})|\gamma_0> + \sum_{V=\rho,\omega,\phi} \frac{e}{g_V}\{1 - \overline{\Gamma_V}(\vec{r_j})\}|V> . \tag{3.20}$$

Note that the γ_0 component is, by definition, not modified due to the presence of the nuclear medium. The cross section for the photon to react with nucleon j at position $\vec{r}_j$ inside the nucleus can be deduced via equation (3.20) from the optical theorem:

$$\sigma_{\gamma N}(\vec{r}_j) = (1 - \sum_{V=\rho,\omega,\phi} \frac{e^2}{2g_V^2})^2 \sigma_{\gamma_0 N} + \sum_{V=\rho,\omega,\phi} (\frac{e}{g_V})^2 |1 - \overline{\Gamma_V}(\vec{r}_j)|^2 \sigma_{VN}. \tag{3.21}$$

As for the photon in vacuum, each term gives the relative weight for the corresponding photon component to be passed to FRITIOF. When integrated over the whole nucleus, one gets the total incoherent photonuclear cross section using equation (3.21):

$$\sigma_{\gamma A}^{inc} = \int d^3 r_j n(\vec{r}_j) \sigma_{\gamma N}(\vec{r}_j). \tag{3.22}$$

Now let us formally deduce the effect of shadowing on $\sigma_{\gamma N}$ from the knowledge of the shadowed $\sigma_{\gamma A}$. For the total photon-nucleus cross section, one has:

$$\sigma_{\gamma A} = A\sigma_{\gamma N} - \int d^3 r \rho(\vec{r}) S(\vec{r}) \equiv A_{eff} \sigma_{\gamma N}, \tag{3.23}$$

where everything is expressed in cylindrical coordinates. ρ is the nuclear density and the exact expression for the function S can be found in reference [Eff00]. We can define a shadowing factor $s_N(\vec{r})$ for an in-medium photon-nucleon cross section by:

$$s_N(\vec{r}) = 1 - \frac{S(\vec{r})}{\sigma_{\gamma N}}, \tag{3.24}$$

so that one can write the total photon-nucleus cross section as an integral over the in-medium shadowed single nucleon cross sections given by:

$$\sigma_{\gamma A} = \int d^3 r \rho(\vec{r}) s_N(\vec{r}) \sigma_{\gamma N}. \tag{3.25}$$

Now, the in-medium cross section $\sigma_{\gamma N \to Nm}^{med}$ for photoproduction of a meson m in $\gamma N \to Nm$ is related to the same cross section in vacuum by:

$$\sigma_{\gamma N \to Nm}^{med} = s_N(\vec{r}) \sigma_{\gamma N \to Nm}^{vac}. \tag{3.26}$$

3.1.8 The perturbative weight of each outcoming particle type

As already stated, in the present model the incoherent reaction of a photon with a nucleus takes place in two steps. In the case of photonuclear reactions for instance, in the first step the photon reacts with one nucleon inside the nucleus (impulse approximation) and produces some final state X. In this process nuclear effects such as Fermi motion, binding energies and Pauli blocking of the final state nucleons are taken into account. In the second step the final state X is propagated within the transport model. During the first step, each particle making up the final state X is assigned a perturbative weight which is simply the total photon-nucleon cross section at the center of mass energy $\sqrt{(s)}$ of that original interaction. In the following elastic and inelastic scattering of those secondary particles (i.e. their propagation through the nucleus which is the second step of the calculation), the same perturbative weight is transferred from the initial state to all final state particles. Also, in the decay of an unstable particle, the perturbative weight of each decay product, is the perturbative weight of the decaying particle.

3.1.9 The two-pion cut-off for the rho

In the CBUU model, the only hadronic decay channel for the rho (in vacuum) is the two-pion decay. Therefore the rho vacuum self-energy as well as the rho spectral distribution (containing the imaginary part of the self-energy in the denominator) vanish below the two-pion threshold. Hence, in processes where the vacuum cross sections are used (which is usually the case in transport simulations), no rho mesons with masses below twice the pion mass are produced. This can be seen from the discontinuity in the Figure 3.2 (taken from the reference [Eff99b]) for the $\rho_0 \to e^+e^-$ contribution spectrum to the general channel $\gamma Pb \to e^+e^-X$ at 2.2 GeV photon energy for instance.

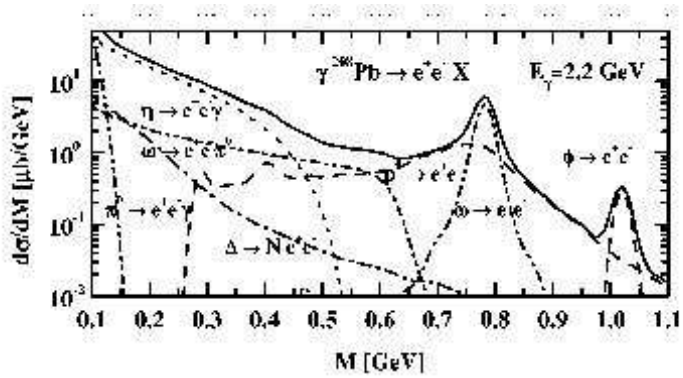

Figure 3.2: The dilepton invariant mass spectrum $d\sigma/dM$ for γPb at the photon energy $E_\gamma = 2.2GeV$ calculated with bare meson masses including a resolution of 10MeV (taken from reference [Eff99b]).

3.2 The specifics of the treatment of the inclusive e^+e^- pair production from γA reactions (i.e. g7 case)

The content of this section is largely inspired from the reference [Eff99b] which gives a complete treatment of the e^+e^- production from γA reactions at the fixed photon energies of 0.8, 1.5 and 2.2 GeV, where A is the C, Ca or Pb nucleus. The authors present dilepton cross sections with and without the inclusion of medium effects such as collisional broadening and Brown-Rho mass shift for the vector mesons. The reader is recommended to have a look at this paper for the detail of their findings. Some of the specifics for the numerical implementation of the inclusive e^+e^- pair production from γA reactions is given here.

3.2.1 The resonance properties

The right hand side of the CBUU equation (3.2) (i.e. the collision term) accounts for the collisions between the particles produced during the primary

reaction with the nucleons during their propagation inside the nucleus. In addition to the elastic scattering processes, it also includes inelastic contributions such as direct meson production channels and the excitation/deexcitation of higher baryon resonances. The CBUU model used here incorporates, besides the nucleon, all baryonic resonances up to a mass of 2350 MeV/c^2, i.e.:$P_{33}(1232)$, $P_{11}(1440)$, $D_{13}(1520)$, $S_{11}(1535)$, $P_{33}(1600)$, $S_{31}(1620)$, $S_{11}(1650)$, $D_{15}(1675)$, $F_{15}(1680)$, $P_{13}(1879)$, $S_{31}(1900)$, $F_{35}(1905)$, $P_{31}(1910)$, $D_{35}(1930)$, $F_{37}(1950)$, $F_{17}(1990)$, $G_{17}(2190)$ and $D_{35}(2350)$. The resonances couple to the following channels:$N\pi$, $N\eta$, $N\omega$, ΛK, $\Delta(1232)\pi$, $N\rho$, $N\sigma$, $N(1440)\pi$, and $\Delta(1232)\rho$. The cross section for the production of a resonance R in a collision of a meson m with a baryon B is given by:

$$\sigma_{mB\to R} = \frac{2J_R+1}{(2J_m+1)(2J_B+1)}\frac{4\pi}{k^2}\frac{s\Gamma^{in}_{mB}\Gamma^{out}_{tot}}{(s-M_R^2)^2+s\Gamma^{out2}_{tot}}, \tag{3.27}$$

where J_R, J_m and J_B denote the spins of the resonance, the meson and the baryon, respectively. k is the center of mass system momentum of the incoming particles, s is the squared invariant energy, M_R is the pole mass of the resonance. The total decay width Γ^{out}_{tot} is given as a sum over the partial decay widths of the resonance. For a specific channel mB, it is:

$$\Gamma^{out}_{mB} = \Gamma^0_{mB}\frac{\rho_{mB}(s)}{\rho_{mB}(M_R)}, \tag{3.28}$$

with Γ^0_{mB} being the partial decay width at the pole of the resonance and $\rho_{mB}(s)$ given as:

$$\rho_{mB}(s) = \int d\mu_m d\mu_B S_m(\mu_m)S_B(\mu_B)\times\frac{q(s,\mu_m,\mu_B)}{\sqrt{s}}B^2_{l_{mB}}(qR), \tag{3.29}$$

where S_m and S_B denote the spectral functions of the outgoing particles. q is their center of mass momentum, l_{mB} their relative angular orbital momentum and $B_{l_{mB}}$ is a Blatt-Weisskopf barrier penetration factor. For an unstable particle i, the spectral function S_i is given by:

$$S_i(\mu) = \frac{2}{\pi}\frac{\mu^2\Gamma_{tot}(\mu)}{(\mu^2-M_i^2)^2+\mu^2\Gamma^2_{tot}(\mu)}, \tag{3.30}$$

where M_i denotes the pole mass and $\Gamma_{tot}(\mu)$ is the total width. For a stable particle, S_i is simply:

$$S_i(\mu) = \delta(\mu - M_i). \tag{3.31}$$

The incoming width Γ^{in}_{mB} in equation (3.27) is given by:

$$\Gamma^{in}_{mB} = C^{I_R}_{mB}\Gamma^0_{mB}\frac{kB^2_{l_{mB}}(kR)}{\sqrt{s}\rho_{mB}(MR)}, \tag{3.32}$$

where $C^{I_R}_{mB}$is the appropriate Clebsch-Gordan coefficient for the coupling of the isospins of the baryon and meson to the isospin I_R of the resonance.

3.2.2 Baryon-baryon and meson-baryon collisions

As mentioned previously, the FRITIOF model is used for high energy (defined as in 3.1.3) baryon-baryon and meson-baryon collisions. In the case of $\pi^- p$ scattering, the incoherent sum of all the resonance contributions gives a very good agreement with experimental data for $\sqrt{s} \leq 1.73$ GeV. For higher energies a background $\pi N \rightarrow \pi\pi N$ cross section needs to be included. For the $\pi^+ p$ case, again the incoherent sum of all the resonance contributions gives a good agreement and for higher energies, the background contributions from $\pi N \rightarrow \pi N$ and $\pi N \rightarrow \pi\pi N$ need to be taken into account additionally. The $\pi^0 p$ total cross section is given using isospin symmetry by:

$$\sigma_{\pi^0 p} = \frac{1}{2}(\sigma_{\pi^+ p} + \sigma_{\pi^- p}). \tag{3.33}$$

In addition to the resonance contributions, the following processes are taken into account: $\pi N \leftrightarrow \omega N$, $\pi N \rightarrow \omega\pi N$, $\omega N \rightarrow \pi\pi N$, $\omega N \rightarrow \omega N$, $\pi N \leftrightarrow \phi N$, $\pi N \rightarrow \phi\pi N$, $\phi N \rightarrow \pi\pi N$, $\phi N \rightarrow \phi N$. The references from which their cross sections are taken are given in [Eff99b].

3.2.3 The treatment of broad resonances and the parametrization of elementary γN cross sections

For a broad resonance such as the ρ, the in-medium width appearing in the spectral function of the equation (3.30) is directly related to the loss rate L_ρ (defined in equation (3.6)) by:

$$\Gamma_{tot,\rho} = \gamma L_\rho, \tag{3.34}$$

where γ is a Lorentz factor which appears since $\Gamma_{tot,\rho}$ is the decay rate in the rest frame of the ρ meson. The one-pion, two-pion and eta production from γN reactions at low and higher energies is treated according to the descriptions given in the sections 3.1.3, 3.1.7 and 3.2.2. The production of the vector mesons ρ, ω and ϕ from $\gamma N \to VN$ collisions is fitted to experimental data and treated independently of the Lund model FRITIOF for all energies. The cross section for those reactions is given by:

$$\sigma_{\gamma N \to NV} = \frac{1}{p_i s} \int d\mu |M_V|^2 p_f S_V(\mu), \tag{3.35}$$

where $\sqrt{s}$ is the total energy of the γN system, p_i and p_f are the momenta of the initial and final particles in the center of mass system, and S_V is the spectral function of the vector meson V. The matrix elements M_V are parametrized as: $|M_\rho|^2 = 0.16 mbGeV^2$, $|M_\omega|^2 = \frac{0.08 p_f^2}{2(\sqrt{s}-1.73GeV)^2+p_f^2} mbGeV^2$ and $|M_\phi|^2 = 0.004 mbGeV^2$.

3.2.4 Dilepton production

The dilepton yields include contributions from the direct vector meson decays $\rho \to e^+e^-$, $\omega \to e^+e^-$ and $\phi \to e^+e^-$, as well as 4 Dalitz decays: $\Delta \to Ne^+e^-$, $\eta \to \gamma e^+e^-$, $\omega \to \pi_0 e^+e^-$ and $\pi_0 \to \gamma e^+e^-$. The references from which the parameters used for the Dalitz decays are taken are given in [Eff99b]. The dilepton decay of vector mesons is calculated assuming strict vector meson dominance with:

$$\Gamma_{V \to e^+e^-}(M) = C_V \frac{m_V^4}{M^3}, \tag{3.36}$$

where $C_\rho = 8.814 \times 10^{-6}$, $C_\omega = 0.767 \times 10^{-6}$ and $C_\phi = 1.344 \times 10^{-6}$. See reference [Eff99b] for the formula of the calculation of dilepton yields from vector meson decays and from the Δ Dalitz decay.

3.2.5 Inclusion of in-medium effects: collisional broadening and Brown-Rho scaling

The code allows one to choose to include effects such as collisional broadening and a dropping of the ρ and ω mass according to the Brown-Rho formula. The in-medium widths of the ρ and ω mesons are calculated as sketched in 3.2.3. In the rest frame of the meson, the total in-medium width is given as:

$$\Gamma^V_{tot}(\mu, |\vec{p}|, \rho) = \Gamma^V_{vac}(\mu) + \Gamma^V_{coll}(\mu, |\vec{p}|, \rho), \tag{3.37}$$

where the collisional width Γ^V_{coll} reads:

$$\Gamma^V_{coll}(\mu, |\vec{p}|, \rho) = \gamma\rho < v_{VN}\sigma^{tot}_{VN} >, \tag{3.38}$$

and Γ^V_{vac} is the vacuum decay width. The brackets in the above equation stand for an average over the Fermi sea of the nucleons, v_{VN} is the relative velocity between vector meson and nucleon, and σ^{tot}_{VN} is their total cross section. ρ is the nuclear density and γ the Lorentz factor for the boost to the rest frame of the vector meson. To explore the consequences of the vector meson mass shift at finite nuclear density, the vector mesons can be modeled according to the Brown-Rho scaling or Hatsuda and Lee by introducing a scalar potential $S_V(\vec{r})$:

$$S_V(\vec{r}) = -\alpha m^0_V \frac{\rho(\vec{r})}{\rho_0}, \tag{3.39}$$

where $\rho(\vec{r})$ is the nuclear density, m^0_V the pole mass of the vector meson, $\rho_0 = 0.168 fm^{-3}$ and $\alpha = 0.18$ for the ρ and ω. This leads to an 18% drop in the mass of those vector mesons since their effective mass is then given by:

$$\mu_* = \mu + S_V = (1 - \alpha\frac{\rho(\vec{r})}{\rho_0})m^0_V. \tag{3.40}$$

3.2.6 The form of the output when the code is used as an event generator

The code can be used to get final state yields to do studies such as in reference [Eff99b] or it can be used to generate events to be fed into a simulation package. When used as an event generator for the purposes of simulating the g7 experiment, it gives in its output the e^+e^- final state from the 7 decays cited in 3.2.4 (3 direct vector meson decays and 4 Dalitz decay contributions). For each such final state, an array is made with the production channel, the photon energy and the weight of the event in its first row, the charge, and the x, y and z components of the momentum for the positive and negative lepton in its second and third raw. A different generated data file is produced for a given photon energy and a given target nucleus. Those events are then propagated through the g7 target and the CLAS detector using the GSIM simulation package.

3.3 The final word on the code

The reference [Eff99b] has a very nice conclusion paragraph on the Giessen CBUU code which will be stated as is here: In photonuclear reactions, vector mesons are in general produced with larger momenta relative to the nuclear medium than in heavy-ion collisions. Since the in-medium spectral functions of the vector mesons are momentum dependent, one might observe rather different in-medium effects in both reactions. These, together with additional information from pion-nucleus reactions might help to discriminate between the different scenarios of medium modifications. Therefore a calculation of all reactions within one model is necessary for a conclusive interpretation of the experimental data. The Giessen CBUU transport code provides such a tool.

Chapter 4

The analysis

4.1 Vertex Cuts

Since the goal of the g7 experiment is the detection of an e^+e^- pair from a vector meson decay, a first set of general cuts is applied on the vertex of the lepton candidates. The two leptons should be matched to the same vertex. The three vertex cuts applied were: (1) difference in z-vertices, (2) radial position in the target, and (3) vertex timing. Fig 4.1 shows a histogram of the difference between the electron and positron z-positions at the vertex. A cut was applied to reject events with a z-difference greater than 3.0 cm, which enforces some correlation between the e^+ and the e^- but remains rather loose. Fig 4.2 shows the radial distribution of the vertex in the target. A cut was set at 2.0 cmin. Any particles originating from beyond this distance would be outside the target area. Now this setting is also loose since the radius of the g7 solid foils actually measured 0.6 cm only. Tightening those cuts would have lowered the statistics which are already low for this experiment because of the small branching ratios for the decay channel being studied.

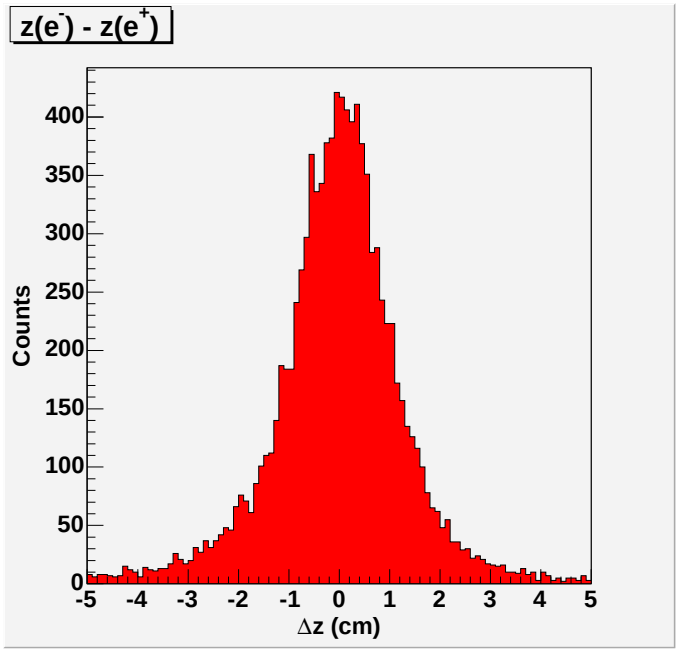

Figure 4.1: The difference in z-vertex of e^- from e^+.

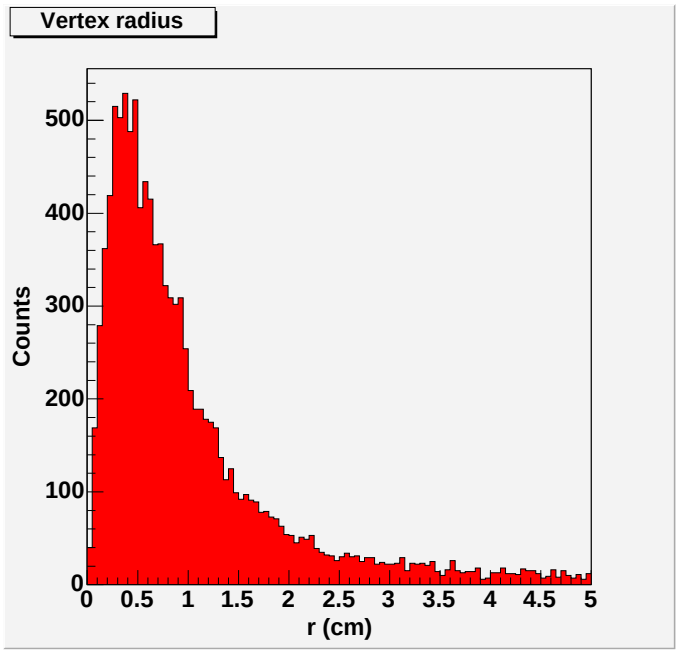

Figure 4.2: The radial vertex position for e^+e^-.

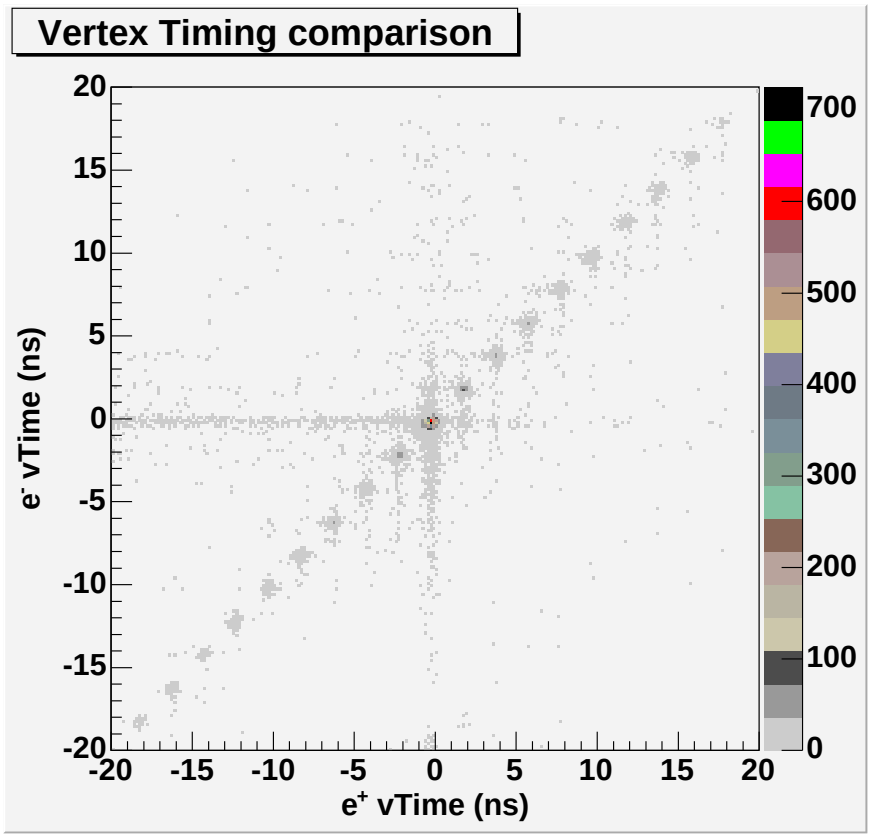

Figure 4.3: Vertex timing for e^- versus e^+.

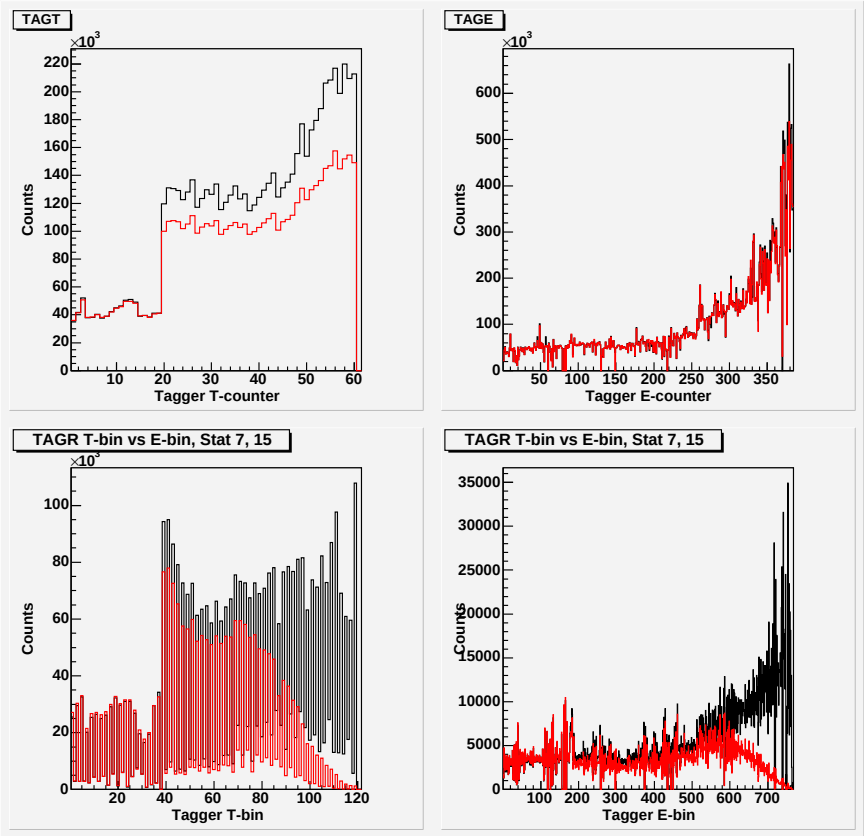

Figure 4.4: Tagger occupancy comparisons for low- and high-intensity runs. The black lines are from a 5nA electron beam run while the red data come from a 50nA run. The 50nA histograms were scaled to match the events in T-counters 1-20 in the 5nA run. The distributions are raw T-counters(upper,left), raw E-counters(upper,right), T-channels(lower,left), and E-channels(lower,right).

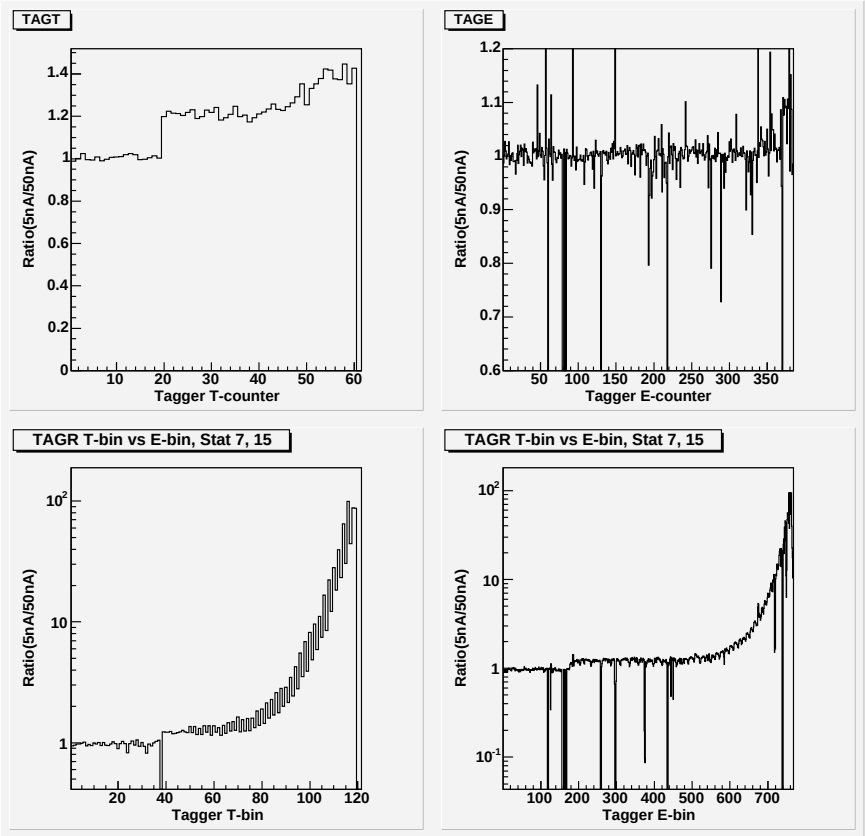

Figure 4.5: Tagger occupancy ratios of low- to high-intensity runs. The 50nA data were scaled to match the events in T-counters 1-20 in the 5nA run. Next, each distribution from the 5nA run was divided by the corresponding data from the 50nA run. The distributions are raw T-counters(upper,left), raw E-counters(upper,right), T-channels(lower,left), and E-channels(lower,right).

The third vertex cut was applied to the vertex timing. The vertex timing is given by

$$t_v = t_{pho} + t_{prop} - t_v^{TOF} \tag{4.1}$$

where t_{pho} is the photon time at the center of CLAS, t_{prop} is the propagation time from the CLAS center to the vertex, and t_v^{TOF} is the particle vertex time calculated from time-of-flight (TOF). For good pair identification, both leptons should have roughly the same vertex timing. Fig 4.3 is a plot of the e^+ vertex timing versus the e^- vertex timing after EC and CC cuts were applied which are outlined in the next section. The timing cut applied is $|t_v(e^-) - t_v(e^+)| < 1.002$ or basically, both leptons had to be from the same beam time bucket. What is interesting to note is the number of pairs which have timing in neighboring beam buckets. Figs 4.4 and 4.5 contain some comparisons of tagger occupancies for a low-intensity 5nA run (black) and higher-intensity 50nA run (red). The 50nA beam current was the standard for all production runs. From this last figure, there is an observable inefficiency in the tagger T-counters for high flux runs at the transition region of the tagger. The raw E-counter occupancies overlap perfectly between the two types of runs. Thus, any lost photons in the reconstruction were due to a T-counter inefficiency and not the E-counters. In a large fraction of events ($\sim 40\%$), the photon timing is misidentified. The effect is the large number of events with vertex timing which appear out-of-time with the good physics events at $t_v = 0$. The missed photon timing does not impact the particle identification since the g7 analysis is an invariant mass calculation of the e^+e^- pair.

4.2 Electron Identification with the CLAS Detector

In this section, the electron identification for the g7a analysis will be described. The electron identification with the CLAS detector has been established by previous electron-beam experiments. The basic procedure is a combination of cuts with the Electromagnetic Calorimeter(EC) and the Cerenkov Counters(CC). These cuts will be discussed in Sections 4.2.1 and 4.2.2.

In order to justify the identification methods, the cuts were applied to two different data sets, a pure sample of π^- particles and an electron sample from the e1b running period. Section 4.3 outlines the use of the $\gamma p \rightarrow \Lambda K^+ \rightarrow p\pi^- K^+$ reaction for the pion misidentification test. Section 4.4 contains the results of the cuts on an electron sample from the e1b experiment.

4.2.1 Electromagnetic Calorimeter

The EC is the primary detector for electron identification. It is a sampling detector where the sampling fraction was designed to be 0.272. Fig 4.6 is a plot of the EC total energy versus momentum for negatively charged particles. A cut was placed above and below the diagonal band with the following functional form

$$\begin{aligned} E_{EC} &= (0.23 + 0.071P - 0.032P^2)(P - P_0) \quad \text{if} \quad P < 1.0 \\ &= 0.272(P - P_0) \quad \text{if} \quad P \geq 1.0 \end{aligned} \tag{4.2}$$

where E_{EC} is the total energy deposited in the EC, P is the momentum, and P_0 is the momentum offset. The value for the offsets were 0.5 and -0.3 GeV/c for the cuts above and below, respectively. Fig 4.7 shows another view of the cuts on the quantity E_{EC}/P.

The EC detector is divided into two sections, an inner and an outer. This segmentation could be employed to further remove misidentified pions from the

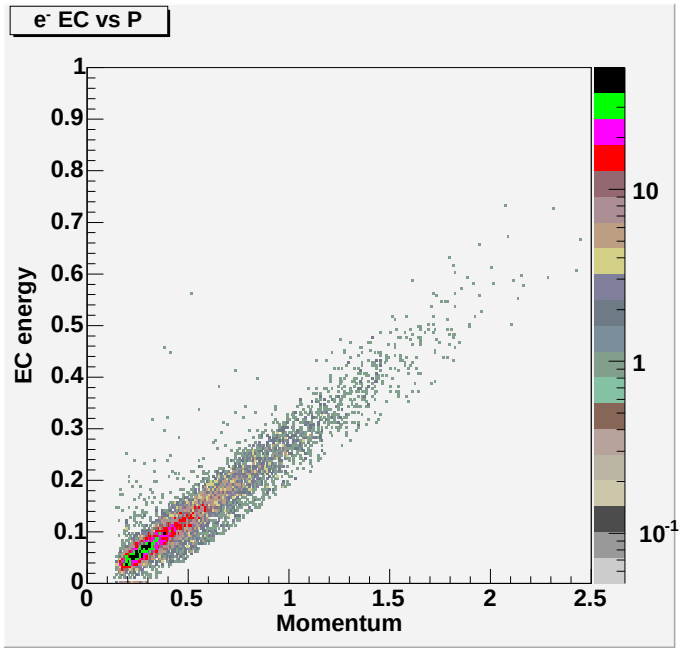

Figure 4.6: Plot of E_{EC} versus momentum for e^- candidates.

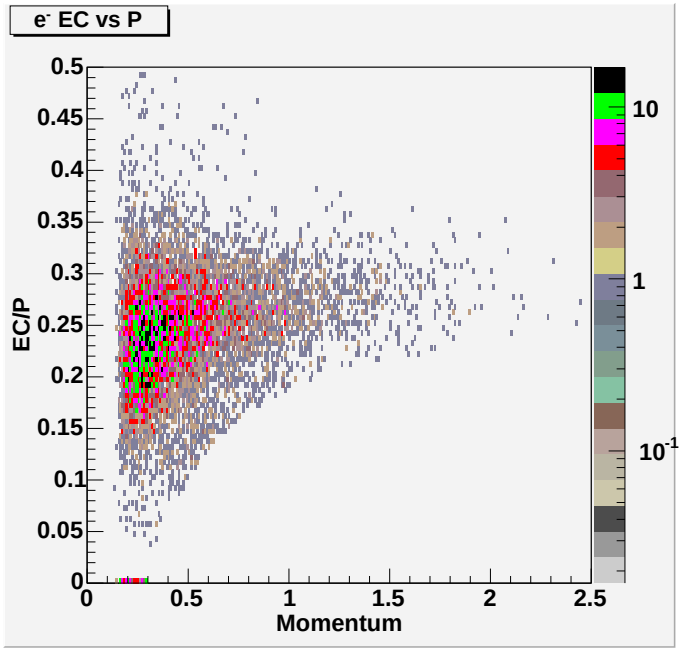

Figure 4.7: Plot of $\frac{E_{EC}}{P}$ versus momentum for e^- candidates.

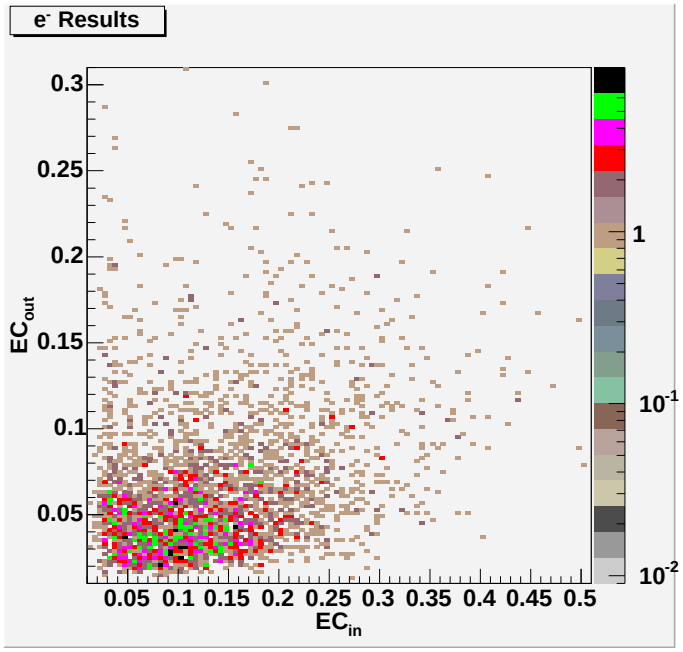

Figure 4.8: Plot of E_{EC} inner versus outer energies for e^- candidates.

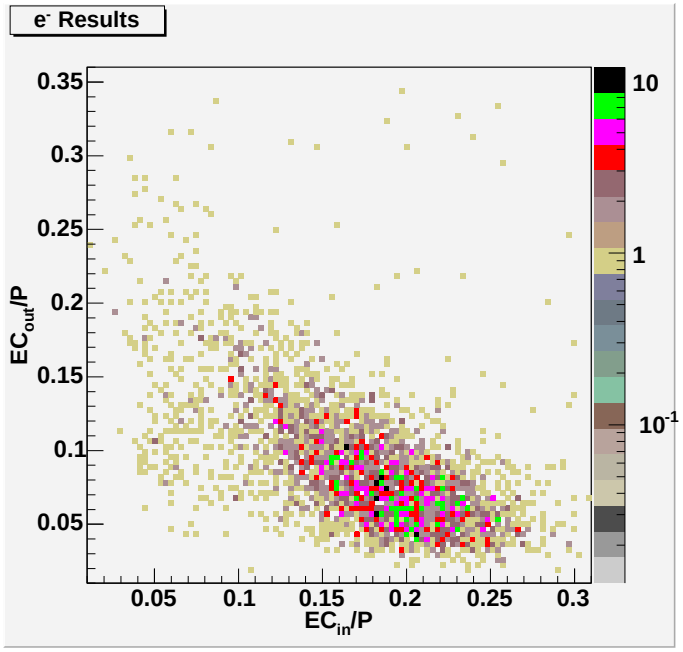

Figure 4.9: Plot of $\frac{E_{EC}}{P}$ inner versus outer energies for e^- candidates.

lepton sample since the lepton is assumed to lose most of its energy in the inner layers whereas the minimum-ionizing pions should lose energy uniformly through both sections. Fig 4.8 shows the EC inner energy versus the EC outer energy, and Fig 4.9 shows the same quantities divided by momentum. The pion contamination would be a vertical band below an EC inner energy of 0.05 GeV. After applying the cut on EC versus P, the vertex cuts, and the CC cuts described in Section 4.2.2, there is very little pion contamination revealed in the plots of EC inner and outer energies.

4.2.2 Cerenkov Counters

With the CC, the leptons are identified by the amount of Cerenkov light produced in the detector. The amount of light is quantified by the number of electrons produced in the photomultiplier tubes (pmt) which collect the light. These electrons from the pmts are called photoelectrons. A typical photoelectron spectrum contains a broad distribution spanning up to 50 or 100 photoelectrons (true leptons) and large peak close to zero (misidentified pions). To reduce the pion misidentification, two cuts were considered:

1. difference in polar angles θ calculated from the hit in CC and the hit in TOF

2. matching the azimuthal angle ϕ in a sector calculated from particle tracking with the side of the sector reported by the hit in the CC

Fig 4.10 shows the results for cut 1. The black line is for the electrons and the red is for positrons. The negative angular difference for the positrons arises from the fact that they were outbending tracks while the tracks of the electrons were inbending toward the beamline. From this typical plot, there is almost no background so this relationship does not aid in background removal. Thus, this cut in matching the polar angles was not used. Cut 2 is a very simplistic and fundamental one. The CC have pmts on both sides of the chambers where the

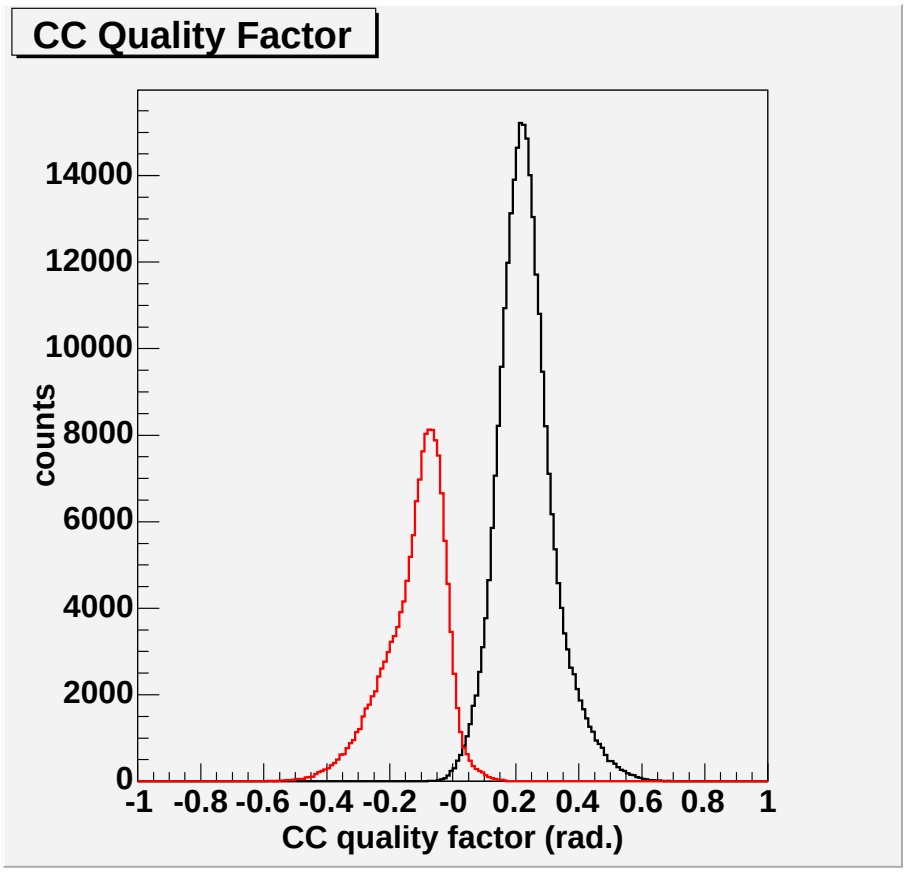

Figure 4.10: Polar angular difference in radians between CC hit and TOF hit. The black (red) histograms are for electrons (positrons).

torus coils are. Therefore, the Cerenkov light will be collected on either the left of the right side of the chambers. The best granularity possible in the angle ϕ is binary, either left or right. The hardware threshold on the CC was set as low as possible with being saturated by pions so there can be a fair amount of accidentals in the CC. This second cut is an obvious first filter of the accidental pions which produce hits in the CC.

Figs 4.11 and 4.12 are examples of the number of photoelectrons after the cuts listed above reduced some of the accidental pion contamination. The pion background has decreased but was not eliminated. A final cut rejecting events with less than 2.5 photoelectrons was applied. This cut is consistent with previous Hall B electroproduction analyses and gives confidence that the pion rejection is

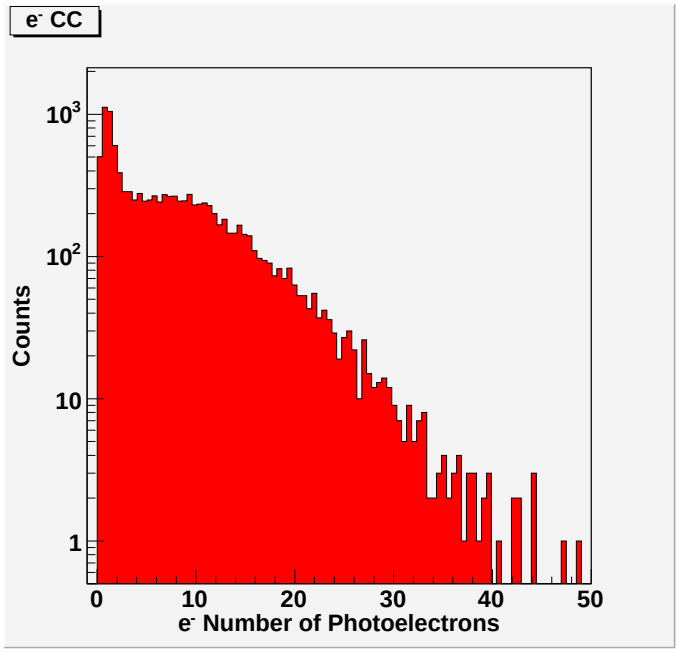

Figure 4.11: Number of CC photoelectrons for electron candidates.

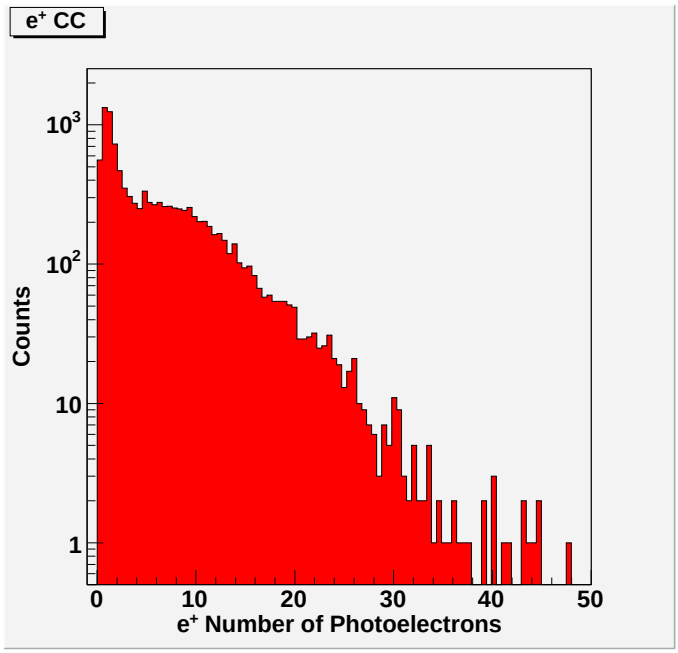

Figure 4.12: Number of CC photoelectrons for e^+ candidates.

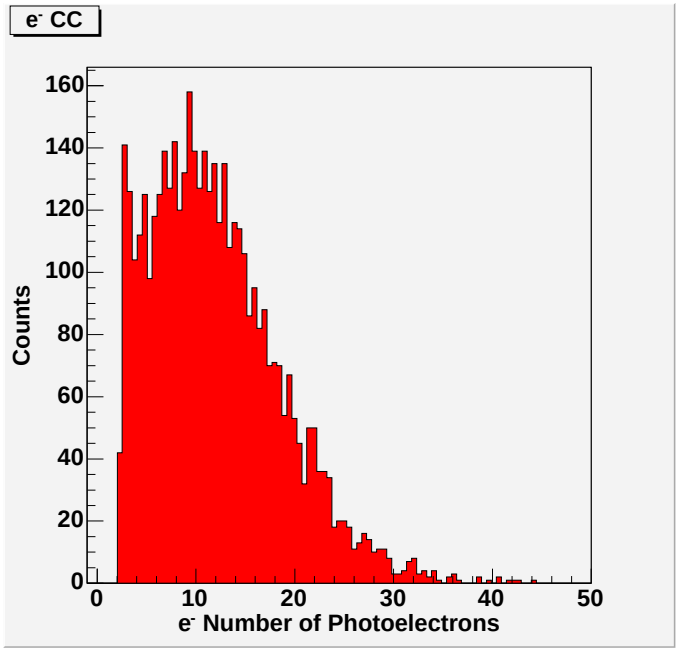

Figure 4.13: Number of photoelectrons for e^- candidates for CC segments from 10 to 18. The events with photoelectrons $\leq$ 2.5 were removed.

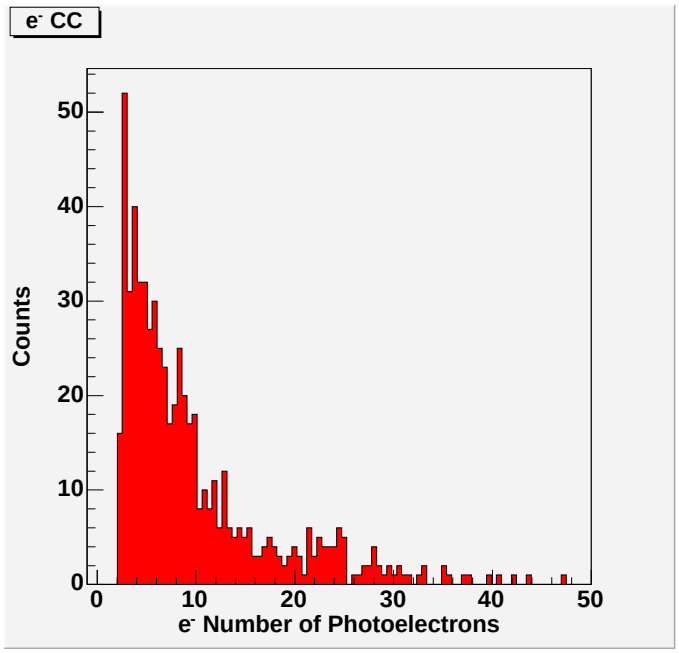

Figure 4.14: Number of photoelectrons for e^- candidates for CC segments 1 and 2. The events with photoelectrons $\leq$ 2.5 were removed.

well understood.

Another issue with the CC is the efficiency of the most forward segments. Each CC sector is divided in 18 segments with a pmt on either side of the segment (left or right). The width of each segment increases as one moves backward in polar angle. The small width of CC segments 1 and 2 means that there is higher probability that a particle will hit the pmt directly which will produce a false signal. Moreover, the volume of gas is smaller in the forward segments which leads to less light collected and a smaller number of photoelectrons. Fig 4.13 is a plot of the number of photoelectrons from segment 10 to 18. Fig 4.14 is a plot of the number of photoelectrons from segments 1 and 2. In segments greater than 10 , a clear peak of true electron is formed. In segment 1, there is very little in terms of a distributions of true electrons. Even though there is definite inefficiency in the forward CC segments, the data from those segments were not removed. This experiment is of such low statistics that throwing away this information would have been too frugal and a more conservative approach was taken. The large peak below 2.5 photoelectrons was still removed by the final cut.

4.3 Pion Misidentification

The most important background to eliminate in order to obtain the final event sample for g7 is the pion background. One needs to keep in mind that almost 100% of the ρ mesons decay into two pions and that the relative branching ratio for the e^+e^- channel is of the order of 10^{-5}. It is thus crucial to discriminate very well between the e^+e^- and the $\pi^+\pi^-$ states.

To test the level to which pions were misidentified by the EC, and CC cuts, the procedure is to apply these cuts on a well-identified sample of pions. The sample chosen was π^- from the well-known Λ decay in the reaction: $\gamma p \rightarrow \Lambda K^+ \rightarrow p\pi^- K^+$. During the g7 run, the Liquid Deuterium target was replaced

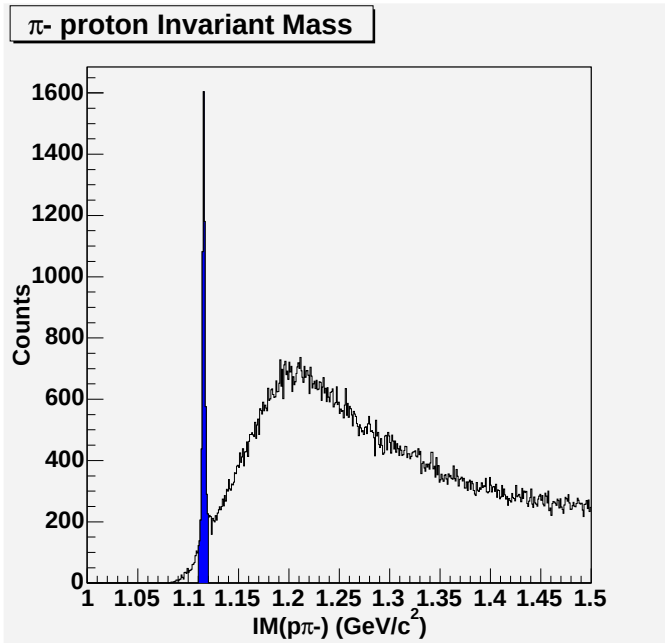

Figure 4.15: Invariant mass of $\pi^- p$ from the reaction $\gamma p \rightarrow \Lambda K^+ \rightarrow p\pi^- K^+$. The blue shaded region is the cut to select the Λ events.

for a short amount of time by a Liquid Hydrogen (i.e. proton) target. The proton target data is about $\frac{1}{4}$ the size of the entire g7 data and was used in case a missing mass off of the proton target was needed. For the purpose of determining the pion rejection efficiency factor, first the proton data set was filtered for a final state containing a proton, a π^-, and a K^+. The second step was to reconstruct the $p\pi^-$ invariant mass which is displayed in Fig 4.15. The last step was to apply the EC and CC cuts to the pions in the mass range of 1.11 to 1.12 GeV/c^2 (i.e all the pions that contribute to the Λ peak). A sample of 5581 "good pion" candidates were selected in this fashion. From the invariant mass plot, there is a small amount of background under the peak. Of those 5581 π^- particles, 3 were misidentified, i.e. 3 passed the g7 EC and CC electron identification cuts. Thus, the pion rejection factor for one arm is 5.4×10^{-4}. The g7 analysis requires a lepton pair in the final state and this translates into a rejection factor of 2.9×10^{-7} for two arms. Given those numbers, one can be quite confident in asserting that the g7 EC and CC cuts do an excellent job of rejecting pions.

4.4 Electron Identification Efficiency

4.4.1 Analysis of e1b Data

Along with the pion misidentification, the efficiency of the lepton cuts must be understood. The level of the EC and CC cuts may be excellent at rejecting pion leakage but could be set too high. Good electron events could be discarded which is unwarranted in this low statistics measurement. For this study, several files from the e1b experiment were analyzed. The events which were filtered had a scattered electron with a momentum from 0.2 to 2.5 GeV/c. The e1b run period immediately preceded the g7 run period and so, the e1b calibration constants for the various CLAS components should be very close to the g7 constants. This was the main motivation for looking at this particular data obtained with an electron beam, in addition to the obvious reason for choosing an electron run because of the presence of an electron (the scattered one) for all final states.

The plots of EC information are displayed in Fig 4.16. These distributions were discussed for g7 data in Section 4.2.1. A striking difference between the e1b results and the g7 results is the vertical band of events at the highest momentum in the E_{EC} versus P and E_{EC}/P versus P plots. These electrons were in the forward fiducial region of the calorimeters. Fig 4.17 shows the EC x- versus y-positions summed over all sectors. In the forward x-position, there are many hits on the edges. These electrons deposit a smaller amount of energy than the sampling fraction since they do not travel through all of the calorimeter layers. If a fiducial cut is applied along the edges as in Fig 4.17, the vertical band disappears in Fig 4.18. In Fig 4.19, the g7 EC and CC cuts were applied. The EC cuts around this distribution are loose enough that barely any of the good electron candidates are removed. Figs 4.20 and 4.21 show the EC x versus y distribution for the g7 data for e^- and e^+ particles respectively. The fiducial cuts in red were determined from the e1b data. The e^+e^- pairs in g7 data are of a different kinematics than e1b. For g7, the leptons are from vector meson decays

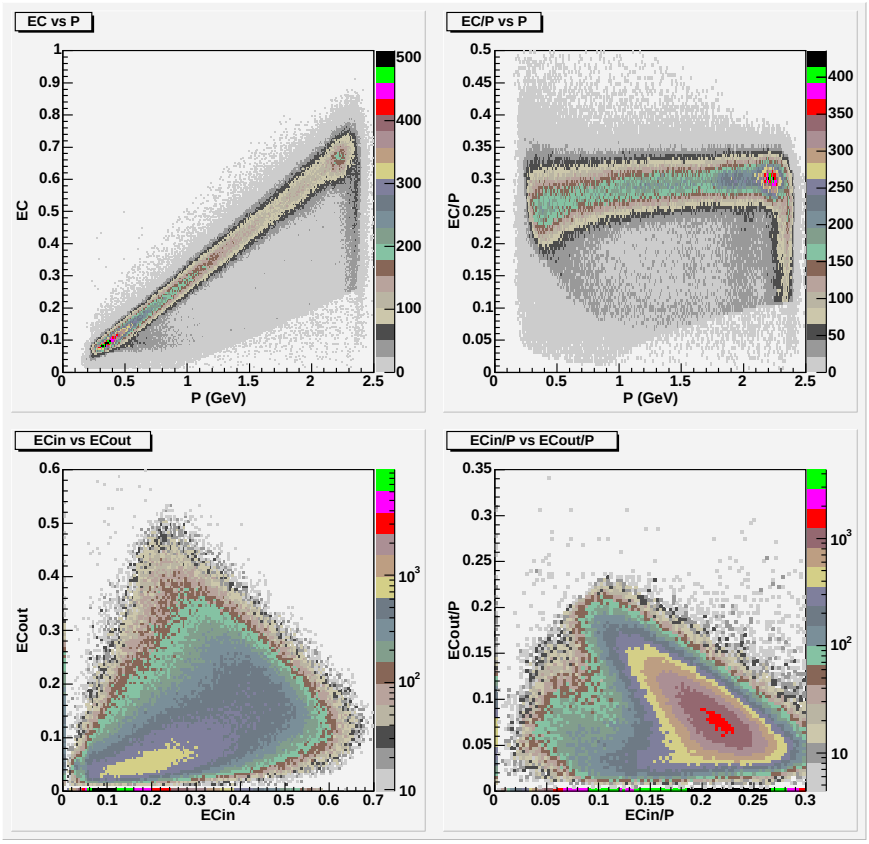

Figure 4.16: Plots of EC distributions for scattered electrons from e1b data.

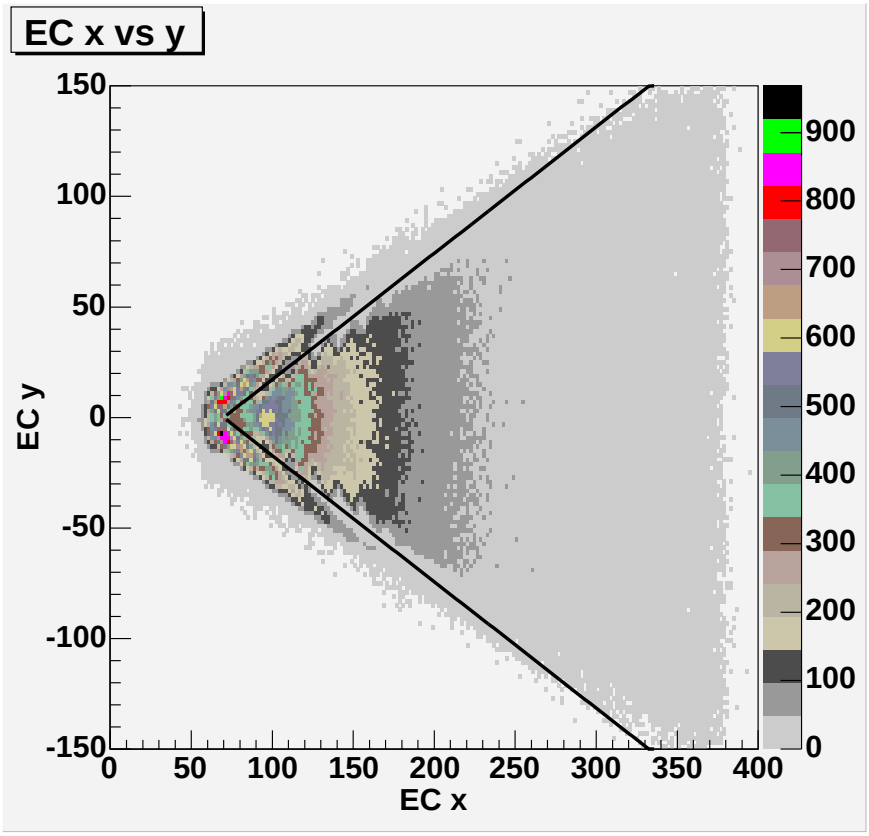

Figure 4.17: The EC x versus y distribution for e1b e^- candidates. The black lines are the fiducial cuts determined for this data.

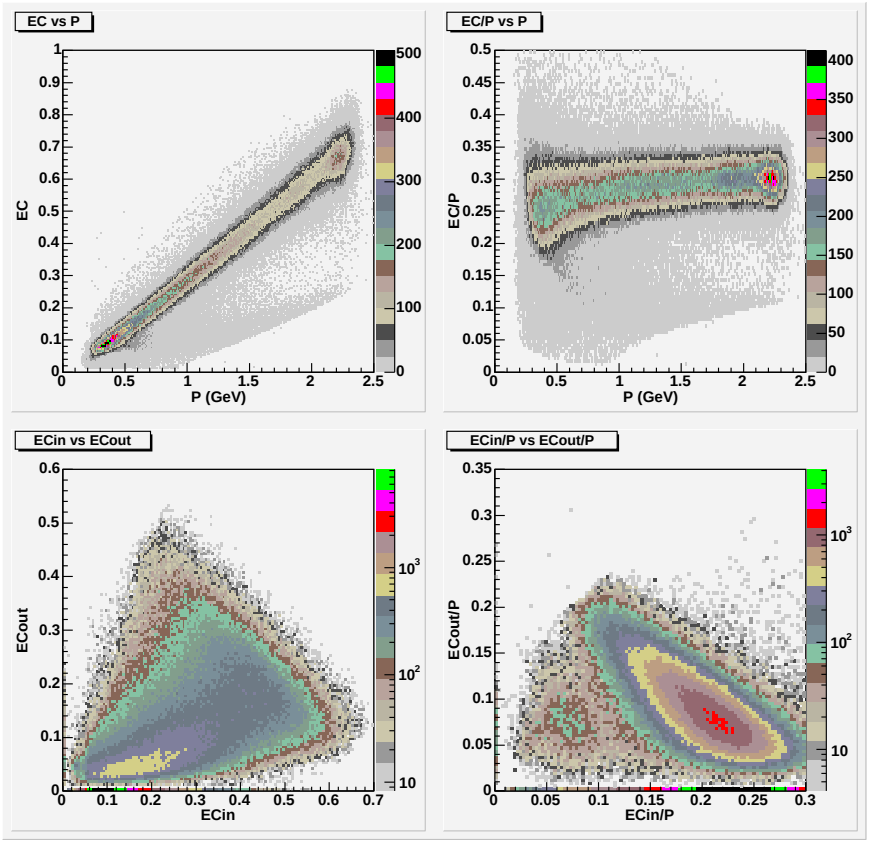

Figure 4.18: Plots of EC distributions for scattered electrons from e1b data after EC x-y fiducial cuts.

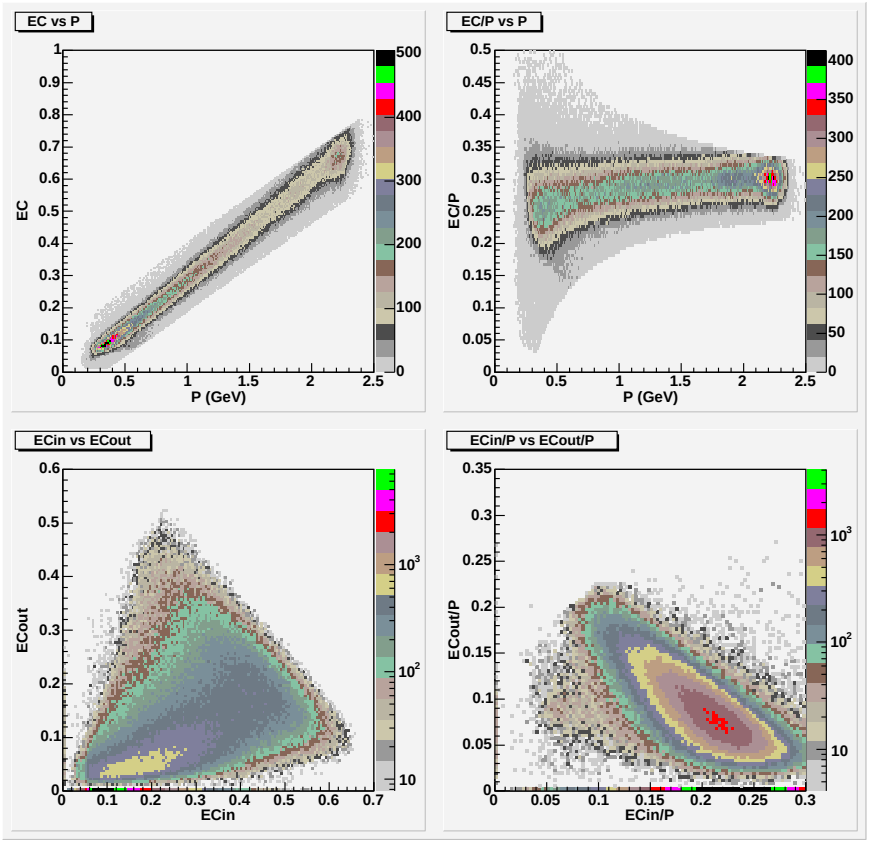

Figure 4.19: Plots of EC distributions for scattered electrons from e1b data after EC x-y fiducial cuts and g7 EC cuts.

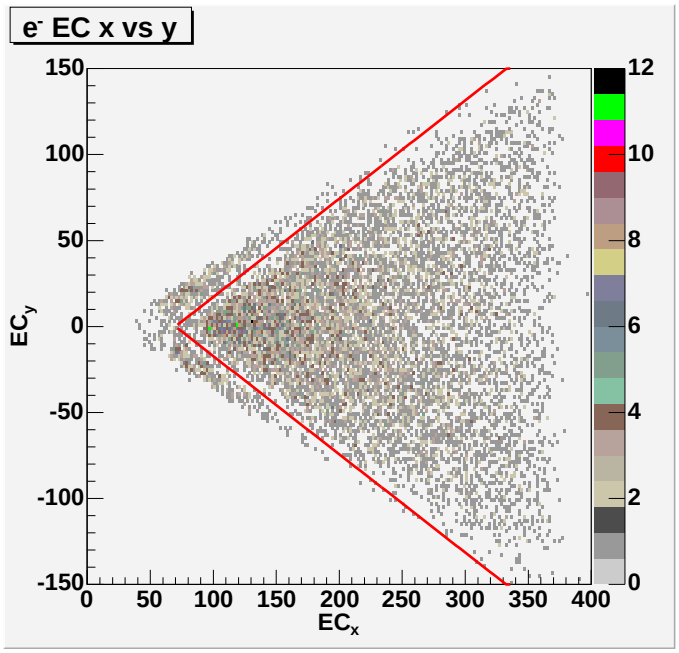

Figure 4.20: The EC x versus y distribution for g7 e^- candidates. The red lines are the fiducial cuts determined from e1b data.

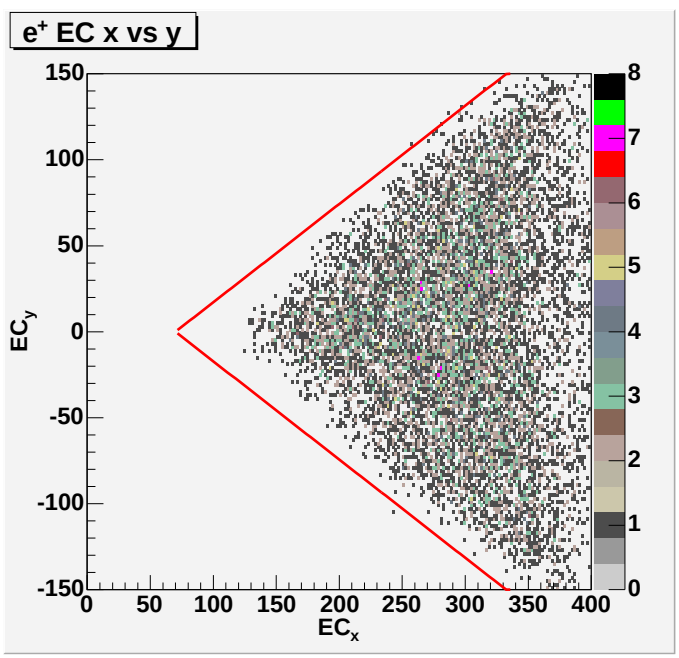

Figure 4.21: The EC x versus y distribution for g7 e^+ candidates. The red lines are the fiducial cuts determined from e1b data.

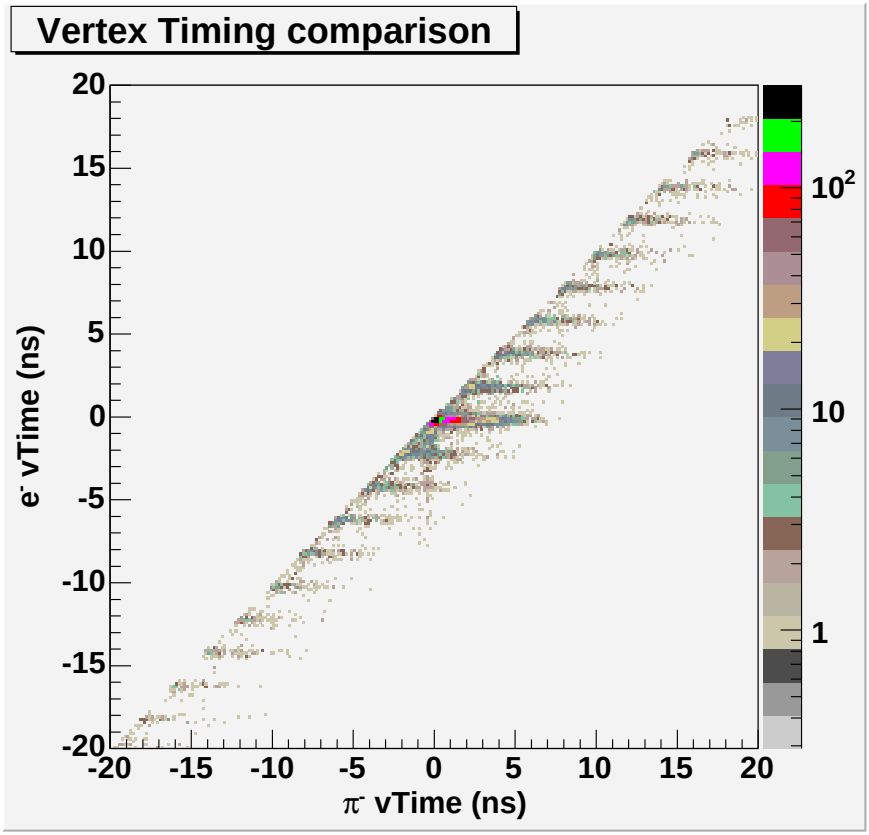

Figure 4.22: Vertex timing for e^+ candidate constrained with electron mass and pion mass.

and have lower momenta. For e1b, the electrons are from inelastic and elastic scattering and can have momenta up to the incident electron beam momentum. This is the reason why the vertical band of events at the highest momentum in the E_{EC} versus P and E_{EC}/P versus P plots for the e1b run when no fiducial cut is applied does not appear on the same plots done for g7. Since those events are also those that give hits at the edges of the EC, the EC x-y fiducial cuts necessary to remove them and thus clean up the e1b data was not employed for the g7 analysis.

4.4.2 Timing with Pion Masses

Another check of the lepton sample purity is to constrain the mass of the lepton candidate with the pion mass. The TOF vertex time t_v^{TOF} in Eq. 4.1 was recalculated with the pion mass. Fig 4.22 is a plot of the vertex timing with the pion mass versus the electron mass. As with Fig 4.3, there are a number of events in neighboring beam buckets due to bad photon timing. The feature which is most important is that events form horizontal bands parallel to the x-axis or the pion-mass constrained time. This result implies that the particles vertex timing is best described when the particle is labeled a lepton. When given the mass of a charged pion, the vertex timing is smeared out. If the particles were truly pions misidentified as leptons, the timing would be smeared out in vertical bands.

4.5 Different sector cut

Fig 4.23 represents invariant mass spectra of e^+e^- pairs from a partial sample of g7 data, where the leptons have been identified by the EC and CC cuts described in Section 4.2. The black curve on that figure corresponds to the spectrum with no additional cuts. The x-axis that represents the invariant mass of the pairs starts at 0.1 GeV. If the same plot was done with the x-axis starting at 0 GeV, a huge peak would be seen at 0 GeV that corresponds to pair production. The dip around 0.16 GeV is due to acceptance. Now, if the vertex cuts described in Section 4.1 are applied then the curve drawn in blue is obtained. If in addition, one requires that the e^+ and the e^- come from different sectors of CLAS, then one gets the red curve. This last requirement essentially cuts in the low mass region dominated by pair production and leaves the signal region unchanged.

One can clearly see very distinct ω and ϕ peaks. The right hand side of the spectra is extremely clean, i.e essentially background free. On the red plot, the ρ signal seems entangled in the low-mass background which forms a bump-like structure around 500 MeV. The shape of this low-mass background is persistent

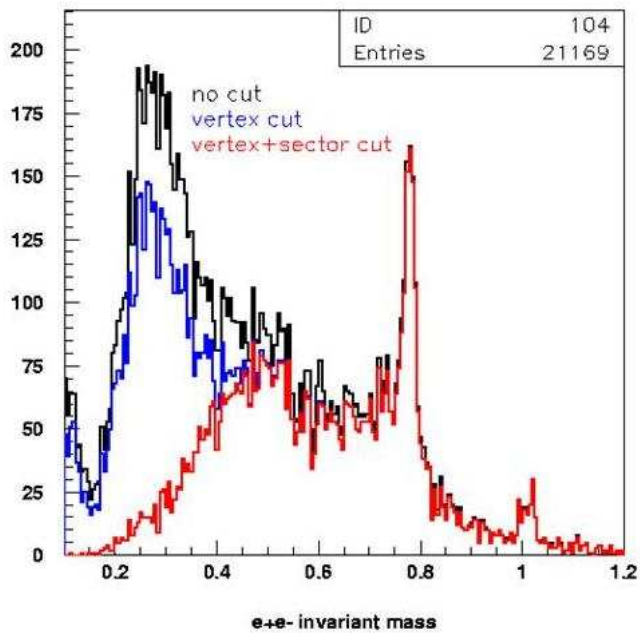

Figure 4.23: Invariant mass spectra of e^+e^- pairs from partial g7 data sample, with no cuts (black), with vertex cuts (blue) and with vertex cuts and the different sector requirement for each lepton. The leptons have been identified with the EC and CC cuts described in Section 4.2.

when one breaks up the data per target. It is thus essential to understand the components of this bump-like structure in order to correctly extract the ρ signal and be able to tell something about its mass. The study of the low-mass background is the subject of Section 4.7.

4.6 The simulations

The simulated e^+e^- invariant mass spectra were generated using the Giessen BUU code described in Chapter 3 as an event generator. As stated in that chapter, the code generates 7 decays: the direct vector meson decays $\rho \to e^+e^-$, $\omega \to e^+e^-$ and $\phi \to e^+e^-$, as well as 4 Dalitz decays: $\Delta \to Ne^+e^-$, $\eta \to \gamma e^+e^-$, $\omega \to \pi_0 e^+e^-$ and $\pi_0 \to \gamma e^+e^-$. Those decays are generated at one given photon energy. In order to get a realistic simulation for the experiment, it was necessary to generate those 7 decays for a g7-beam-like spectrum.

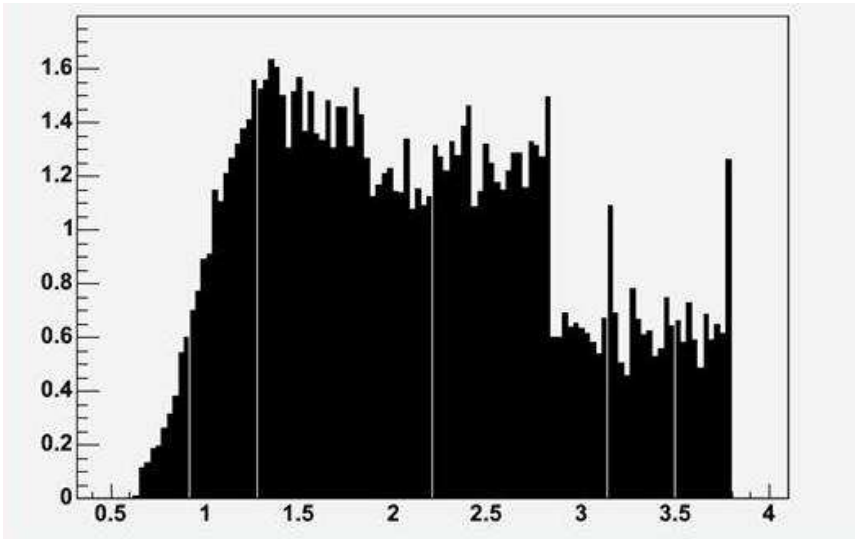

Figure 4.24: Photon spectrum for g7 for 106 tagged energy bins, representing on the x-axis, the photon energy and on the y-axis, the quantity: (number of photons per bin) / (total number of photons in all bins) * 106.

Now, the g7 beam had the spectrum represented on Fig 4.24. To obtain this spectrum, first the g7 tagged photon energy range (0.635 GeV to 3.785 GeV) was divided into 106 energy bins. Next, for each energy bin, the number of photons for that energy bin was obtained by summing over all g7 runs. Then this number of photons per energy bin was divided by the total number of photons in all energy bins and multiplied by the total number of energy bins i.e. 106. This last number is plotted on the Y axis on Fig 4.24 against the photon energy on the X axis. The sharp slope at the low energies is due to the inefficiency of the few last tagger T-counters as a result of the high rate for the g7 experiment. The discontinuity at 2.85 GeV is due to the fact that the spectrum is the sum of 2 bremsstrahlung spectra, one for the first $2/3^{rds}$ of the run period were the photons were generated by a primary electron beam of 3 GeV and the other for the last $1/3^{rd}$ of the run period were they were generated by a primary electron beam of 4 GeV.

The events from the Giessen BUU code come out weighted. The code treats the incoherent reaction of a photon with a nucleus as a two-step process. In the

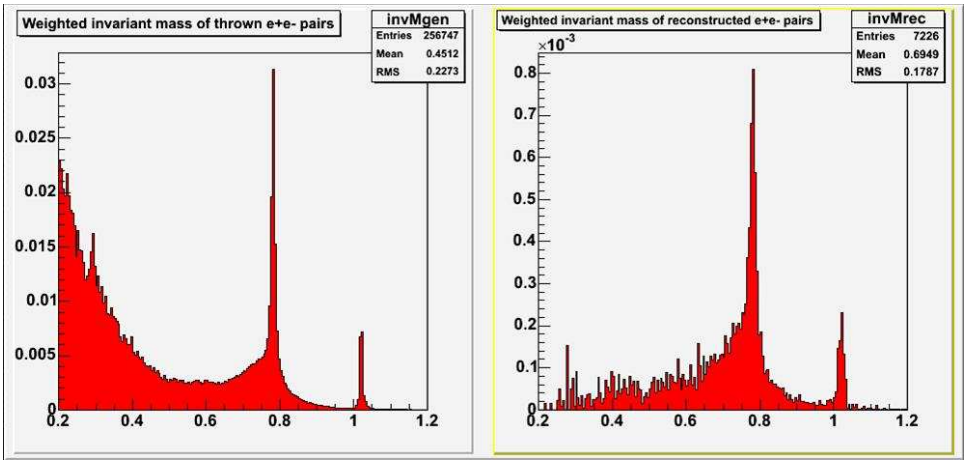

Figure 4.25: Simulated invariant mass of e^+e^- events (weighted) off of the proton target with Giessen BUU code, generated(left) and reconstructed after going through CLAS(right).

first step the photon reacts with one nucleon inside the nucleus (impulse approximation) and produces some final state X. In this process nuclear effects such as Fermi motion, binding energies and Pauli blocking of the final state nucleons are taken into account. In the second step, the final state X is propagated within the transport model. During the first step, each particle making up the final state X is assigned a perturbative weight which is simply the total photon-nucleon cross section at the center of mass energy $\sqrt{(s)}$ of that original interaction. In the following elastic and inelastic scattering of those secondary particles (i.e. their propagation through the nucleus which is the second step of the calculation), the same perturbative weight is transferred from the initial state to all final state particles. Also, in the decay of an unstable particle, the perturbative weight of each decay product, is the perturbative weight of the decaying particle.

So, what one had to do in order to have a realistic simulation for the experiment was to generate the 7 decay channels at the 106 different energies specified by the binning, then simply modify the weight of the event given by the code by multiplying it by the quantity represented on the Y-axis of Fig 4.24 for the corresponding energy bin and finally sum all those events. The resulting invariant

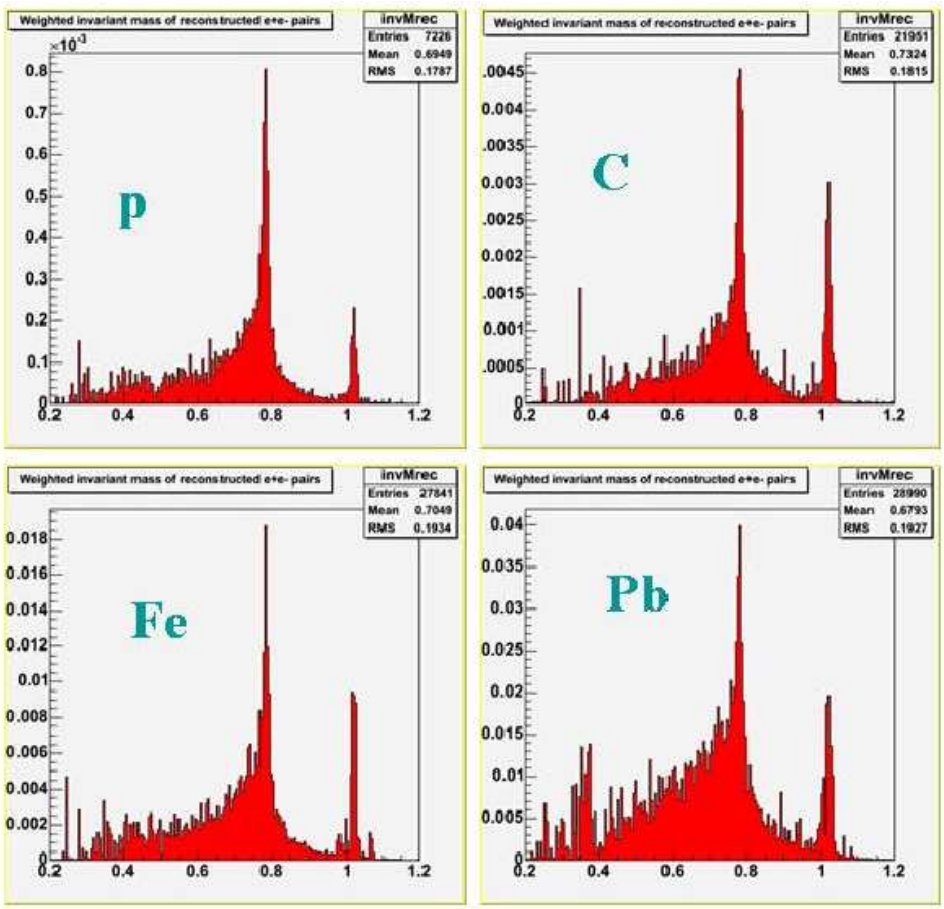

Figure 4.26: Simulated invariant mass of e^+e^- events (weighted) off of the p, C, Fe and Pb targets with Giessen BUU code. The events were reconstructed after going through CLAS.

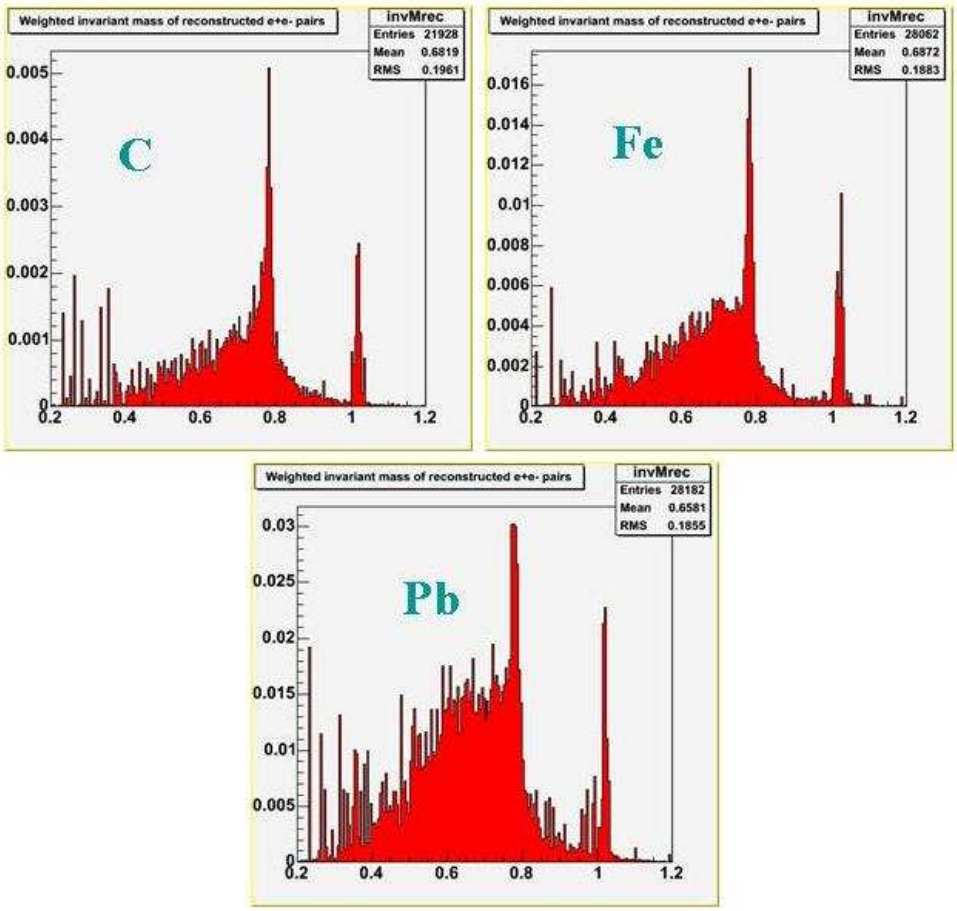

Figure 4.27: Simulated invariant mass of e^+e^- events (weighted) off of the C, Fe and Pb targets with Giessen BUU code when a Brown-Rho shift is added to the vector meson masses. The events were reconstructed after going through CLAS.

mass distributions then seem as if they were generated by a g7-photon-beam-like spectrum.

Another element that contributed to making the simulations as realistic as possible was the inclusion of effects such as the smearing of the resolution for the drift chambers and the time of flight counters, as well as the inclusion of dead time of flight counters and drift chamber holes into GSIM via a standard CLAS program called gpp before reconstructing the events.

The invariant mass spectra obtained in this fashion are represented on Fig 4.25, Fig 4.26, and Fig 4.27. The spikes seen around twice the pion mass are unphysical and are due to a cut-off implemented in the code for the ρ meson. On Fig 4.25, one can compare the generated spectrum to the reconstructed one for the proton target. The 4 Dalitz decays essentially contribute to the low mass region and very few of them actually make it through CLAS as seen in the reconstructed spectrum. Lepton pairs from two Dalitz decays actually make it through CLAS and contribute to the left hand tail at the low invariant masses and those are the pairs from the Dalitz decays of the η and the ω. Fig 4.27 represents the e^+e^- invariant mass spectra for the C, Fe and Pb targets when a Brown-Rho shift is added (dynamically) to the mass of the generated vector mesons (i.e. 16% drop for ρ and ω mesons and 3% drop for the ϕ). The shifted ρ becomes more and more obvious as the target density is increased.

4.7 Understanding the low-mass background

Nothing that resembles the low-mass bump-like structure observed in the data and represented in red on Fig 4.23 can be seen at low masses on the simulation plots (Fig 4.25, Fig 4.26, and Fig 4.27). This suggests that something else than the η Dalitz and ω Dalitz decay contributions is at play. One physical candidate would be e^+e^- pairs from Bethe-Heitler events. Now this already small effect can be expected to be even more reduced in the case of g7 because of the presence of

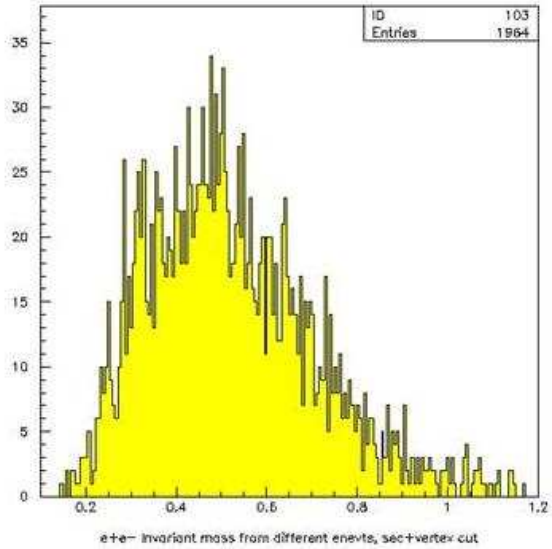

Figure 4.28: Combinatorial background from mixed e^+e^- g7 events. The vertex and different sector cuts have been applied.

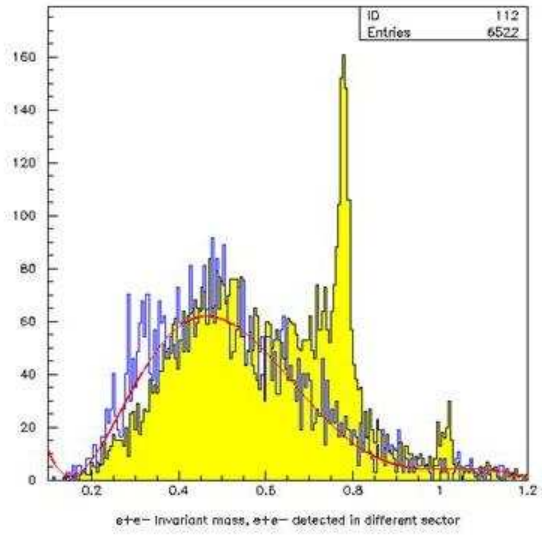

Figure 4.29: Scaled mixed event background shape superimposed on g7 data (partial statistics).

the different sector cut. Most of the Bethe-Heitler pairs come out at small angles, which gives them a very good probability of having hits within the same sector of CLAS and consequently of being cut out through the different sector requirement. Another possibility is to explore the shape of the combinatorial background by mixing e^+ and e^- particles from different g7 events. The idea behind this is the presence of pair production within the target nuclei whose leptons could get mixed with leptons from true vector meson decays that occur simultaneously. Fig 4.28 shows the shape of the combinatorial mixed e^+e^- event background and Fig 4.29 represents that same shape when scaled and superimposed on the partial g7 data from which it was obtained. It is possible to smooth out that shape by mixing the events more times. One can see that the mixed events describe pretty well the low-mass bump-like structure seen on the data, although the match is not quite perfect, and do not cut much at all into the signal region. This suggests that the mixed events give the major contribution to the low-mass background, but also that smaller contributions from the η Dalitz and ω Dalitz decays and the Bethe-Heitler events have to be added in order to improve the fit at the low masses.

Chapter 5

Results

5.1 The final invariant mass spectra

Fig 5.1 represents the invariant mass spectrum of e^+e^- pairs from the full-statistics g7 data, and Fig 5.2 represents the same when the data is broken up per target. The spectra are remarkably clean and the ω and ϕ peaks are extremely distinct thanks to the outstanding pion rejection with CLAS and to its excellent mass resolution. In fact these results represent the first observation of the photoproduction of the ρ, ω and ϕ mesons close to threshold via their rare decay into e^+e^-.

5.2 Observation of the depletion of the ω and ϕ peaks with increasing density

One remarkable observation from Fig 5.2 is the strong depletion of the ω and ϕ peaks with increasing density, i.e. the decrease in the number of counts in the ω and ϕ peaks as one goes from the deuterium target to the carbon target, to the

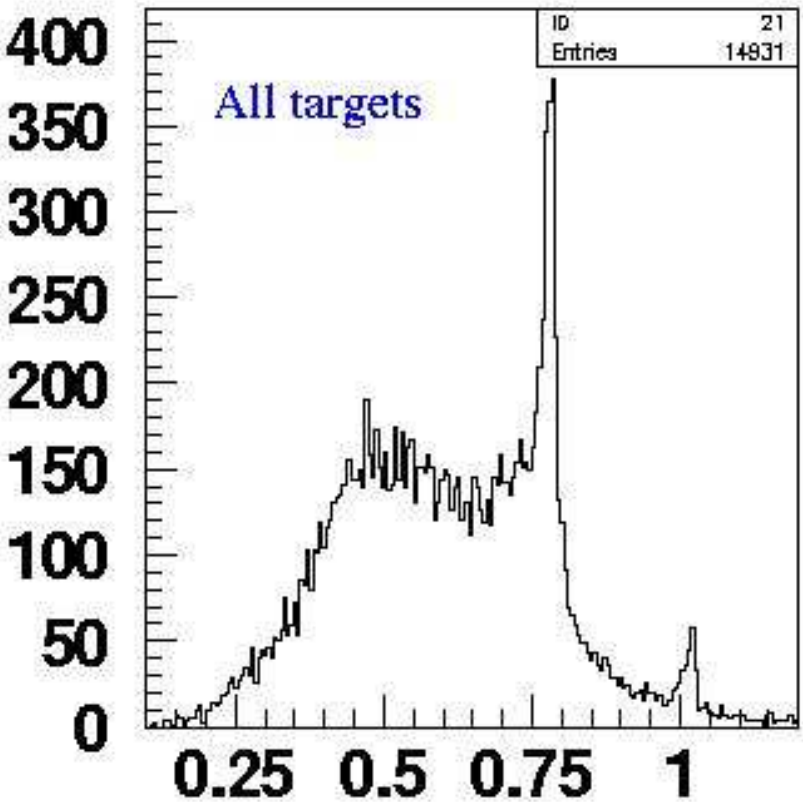

Figure 5.1: Invariant mass of e^+e^- pairs from all g7 targets after vertex cuts and the different sector cut described in Chapter 4 (full statistics).

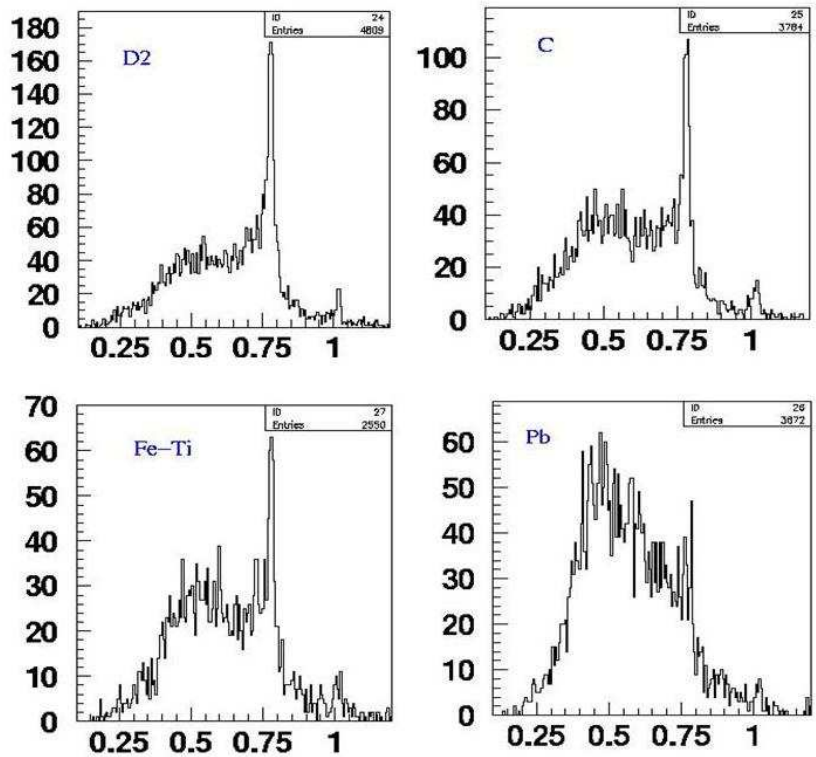

Figure 5.2: Invariant mass of e^+e^- pairs from the g7 D2, C, Fe+Ti and Pb targets after vertex cuts and the different sector cut described in Chapter 4 (full statistics).

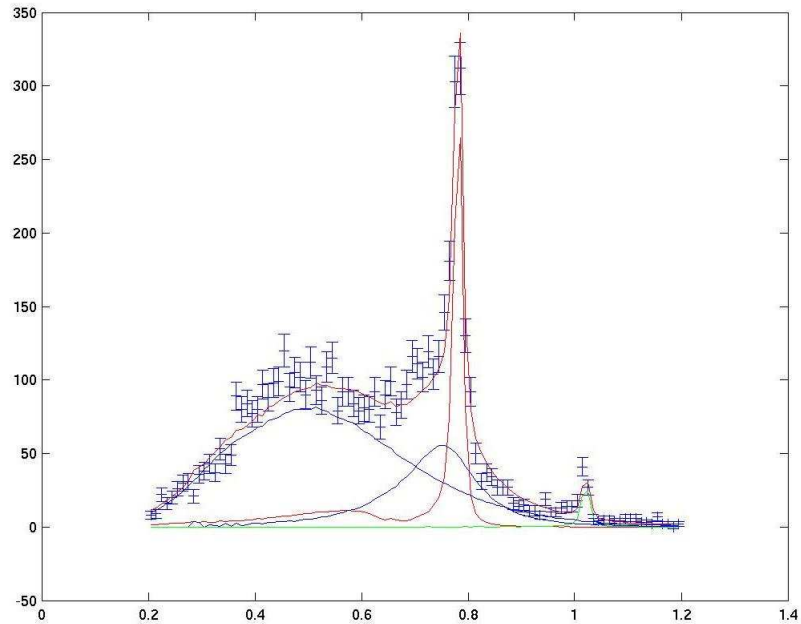

Figure 5.3: Fitted invariant mass spectrum of e^+e^- pairs from *deuterium* target. In blue, data with error bars, in green, fit to the ϕ (from simulations), in red with peak at ω mass, fit to the ω and ω Dalitz (also from simulations), in blue with peak at ρ mass, fit to the ρ (from simulations again), in blue with peak around 500 MeV, fit to the mixed event background and overall fit to data in red.

iron target and to the lead target. Indeed the number of counts in the ω peak is decreased by about 65% in the iron and titanium data combined compared to the deuterium data and by about 85% in the lead data compared once again to the deuterium data. This depletion is not seen in such a dramatic fashion on the simulation plots generated with the Giessen BUU code and consequently it is not being taken into account as it should in the existing theoretical models.

5.3 The fitting and discussion on the medium effects

Fig 5.3, Fig 5.4 and Fig 5.5 represent the fitted invariant mass spectrum of e^+e^- pairs from the deuterium, carbon and iron data. The x-axis that represents

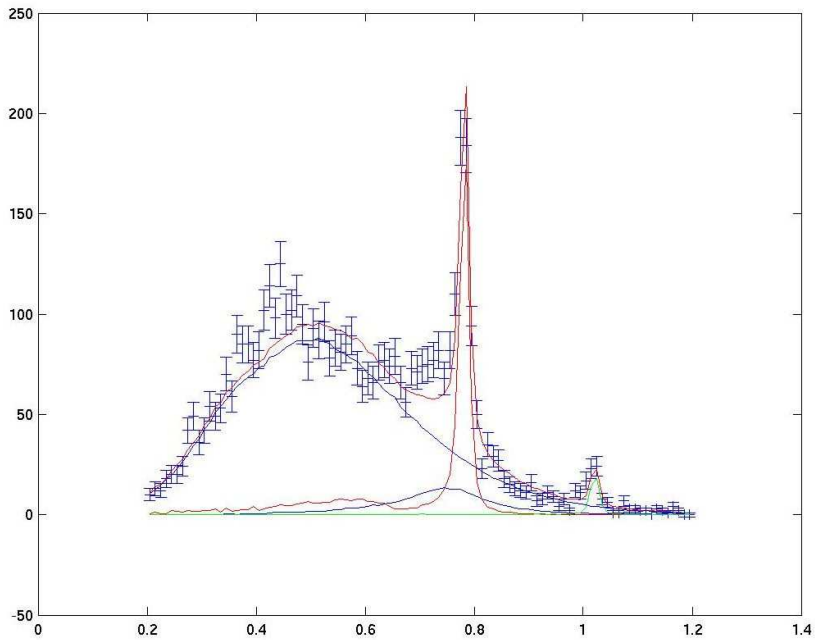

Figure 5.4: Fitted invariant mass spectrum of e^+e^- pairs from *carbon* target. In blue, data with error bars, in green, fit to the ϕ (from simulations), in red with peak at ω mass, fit to the ω and ω Dalitz (also from simulations), in blue with peak at ρ mass, fit to the ρ (from simulations again), in blue with peak around 500 MeV, fit to the mixed event background and overall fit to data in red.

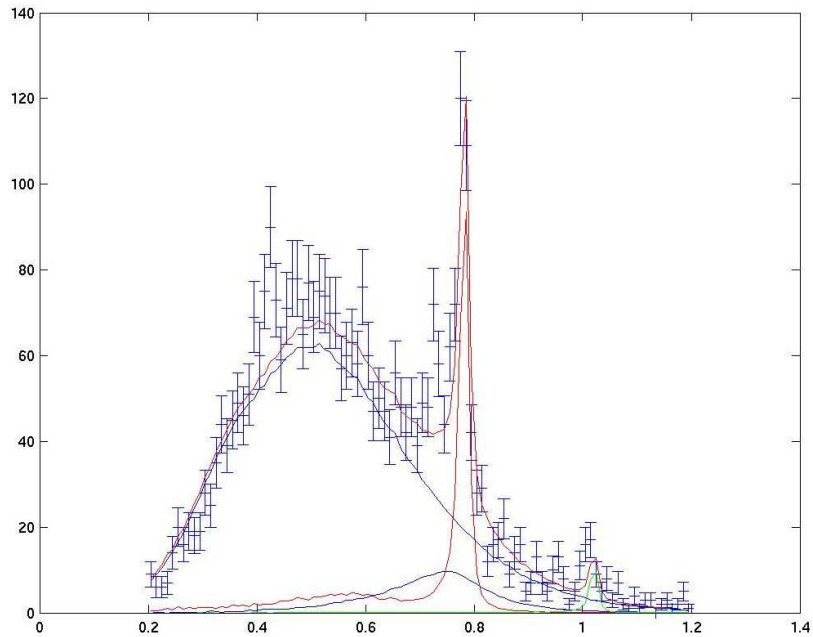

Figure 5.5: Fitted invariant mass spectrum of e^+e^- pairs from *iron* target. In blue, data with error bars, in green, fit to the ϕ (from simulations), in red with peak at ω mass, fit to the ω and ω Dalitz (also from simulations), in blue with peak at ρ mass, fit to the ρ (from simulations again), in blue with peak around 500 MeV, fit to the mixed event background and overall fit to data in red.

the invariant mass of the lepton pairs is divided into 100 mass bins. For each bin, the data point with its error is represented in blue. The figures also show, in green, the fit to the ϕ (from simulations), in red with peak at ω mass, the fit to the ω and ω Dalitz (also from simulations), in blue with peak at ρ mass, the fit to the ρ (from simulations again), in blue with peak around 500 MeV, the fit to the mixed event background and overall the fit to data in red. The ρ, ω and ϕ mesons being fitted are extracted from simulations done for unshifted vector mesons. The fits look reasonable overall. The η Dalitz decay and the Bethe-Heitler contributions have been neglected since they do not have much strength in the mass region of interest i.e. the mass region above about 550 MeV. The chi squared per degree of freedom for the fits is 1.99 for the deuterium data, 2.17 for the carbon data and 1.82 for the iron data. The fits, which are the best to date, are compatible with no medium effects observed on the properties of the vector mesons from this data set. Further work is being done in order to fine-tune these results.

5.4 Work for the future

Obtaining the precise shape of the contribution of the Bethe-Heitler e^+e^- pairs to the invariant mass spectra through Monte Carlo based on quantitative calculations is a current effort. Those calculations take into account the quasi-elastic as well as the inelastic regime via the use of measured nuclear response functions. This will essentially help improve the fits in the low-mass background region, but the Bethe-Heitler distribution may also have a tail into the higher masses which could help fine-tune the fitting of the signal region.

Moreover a quantitative justification for the use of the mixed event method to evaluate the shape of the low-mass background would only be provided via a precise Monte Carlo. So far the tremendous amount of time needed to generate enough pair production leptons that survive up to the furthest regions of CLAS

where they can leave hits detectable by the EC and the CC has been a major obstacle in the way of those simulations. A very clever method needs to be devised in order to significantly reduce the amount of CPU time necessary to carry out this task.

If the current observation of a null result for the medium effects persists through the improved fits, then, this would be a finding with tremendous impact, as it would contradict many recently published results claiming a downward shift for the rho mass. In case a hint for some medium effects appears, then the current data would probably be able to come up with an upper limit on them, however a precise quantification would necessitate increased statistics via a second experimental run.

Chapter 6

Summary and conclusion

A number of theoretical models predict that the properties of vector mesons, such as their mass and width, are modified in a dense medium such as a nucleus. A partial restoration of chiral symmetry at normal nuclear density has been proposed as a possible cause for those modifications besides more "conventional" many-body effects. The E01-112 (g7) experiment has been designed to look for possible density-induced medium effects on the properties of the light vector mesons (ρ, ω and ϕ), in photoproduction, through their rare leptonic decay into e^+e^- pairs. This decay channel has been preferred to the two pion channel to avoid distorting the information by strong final interaction.

A simulation code developed by the group of U. Mosel at the University of Giessen was used to simulate the inclusive e^+e^- photo-production under the conditions of the g7 experiment in order to make comparisons with the experimental data. The code treats the photon-nucleus reactions as a two-step process where, in the first step, the incoming photons react with a single nucleon taking into account the effects of shadowing, then in the second step, the produced particles are propagated explicitly through the nucleus allowing for all kinds of final-

state interactions. The last part of the model is governed by the semiclassical Boltzmann-Uehling-Uhlenbeck (BUU) transport equations. The code actually allows one to simulate the inclusive particle production in heavy-ion collisions from 200A MeV to 200A GeV as well as in pion-, photon-, and electron-induced reactions with the very same physical input.

One major challenge for the analysis of the g7 data set was to separate the e^+e^- final state events from the very large hadronic background (i.e. the decay of the vector mesons into two pions). In doing so, one ought to be careful to reject as much as possible of the pion background, while trying to keep as many as possible of the electron events. A careful study showed that the pion rejection efficiency of CLAS via cuts on the electromagnetic calorimeter and the Cerenkov counters was outstanding with a rejection factor of the order of 10^{-7} for a two-arm final state. The result is an incredibly clean e^+e^- invariant mass spectrum with very distinct ω and ϕ peaks.

The final data sample was broken up per target, which revealed a strong depletion of the ω and ϕ peaks with increasing target density. This depletion was not seen as markedly in the simulations done using the Giessen BUU transport code. The data from each target was fitted using the unmodified ρ, ω and ϕ invariant mass distributions from the BUU simulation code, the omega Dalitz decay contribution also from the same code and the combinatorial background shape from the mixed e^+e^- g7 events. The best fits obtained to date are consistent with no medium effects observed on the properties of the vector mesons from this data set.

Further work is being done in order to fine-tune the fits. A particular attention is given to obtaining the shape of the Bethe-Heitler contribution to the invariant mass spectra via precise calculations and Monte Carlo. This effect is expected to be small but it could help improve the fits, mostly at the lower masses. If the current observation of a null result for the medium effects persists through the improved fits, then, this would be a finding with tremendous

impact, as it would contradict many recently published results claiming a downward shift for the rho mass. In case a hint for some medium effects appears, then the current data would probably be able to come up with an upper limit on them, however a precise quantification would necessitate increased statistics via a second experimental run.

REFERENCES

[Ada01] G. Adams et al., Nucl. Instr. Methods A **465**, 414 (2001).

[Aga95] G. Agakichiev et al., Phys. Rev. Lett. **75**, 1272 (1995).

[Ama01] M. Amarian et al., Nucl. Instr. Methods A **460**, 239 (2001).

[Ber90] P. Y. Bertin and P. A. Guichon, Phys. Rev. C **42**, 1133 (1990).

[Ber94] P. Y. Bertin, M. Kossov, and B. M. Preedom, 1994, CEBAF Proposal PR94-002.

[Bra02] E. Bratkovskaya, Phys. Lett. B **529**, 26 (2002).

[Bro91] G. E. Brown and M. Rho, Phys. Rev. Lett. **66**, 2720 (1991).

[Bro00] W. Brooks, Nucl. Phy. A **663**, 1077c (2000).

[Coh95] T. Cohen, R. Furnstahl, and D. Griegel, Prog. Part. Nucl. Phys. **35**, 221 (1995).

[Dja01] C. Djalali, D. P. Weygand, and M. Kossov, 2001, CEBAF Proposal PR01-112.

[Eff97] M. Effenberger, A. Hombach, S. Teis, and U. Mosel, Nucl. Phys. A **614**, 501 (1997).

[Eff99a] M. Effenberger, E. Bratkovskaya, W. Cassing, and U. Mosel, Phys. Rev. C **60**, 027601 (1999).

[Eff99b] M. Effenberger, E. Bratkovskaya, and U. Mosel, Phys. Rev. C **60**, 044614 (1999).

[Eff00] M. Effenberger and U. Mosel, Phys. Rev. C. **62**, 014605 (2000).

[Fal02] T. Falter and U. Mosel, Phys. Rev. C **66**, 024608 (2002).

[Gil02] J. Gillies, 2002, Probing the boundary of nuclear-particle physics, CERN Courier, May.

[Hat92] T. Hatsuda and S. H. Lee, Phys. Rev. C **46**, R34 (1992).

[Kag99] M. A. Kagarlis et al., Phys. Rev. C **60**, 025203 (1999).

[Ko97] C. M. Ko, V. Koch, and G. Li, Annu. Rev. Nucl. Part. Sci. **47**, 505 (1997).

[Koc96] V. Koch and C. Song, Phys. Rev. C **54**, 1903 (1996).

[Lee01] C. W. Leemann, D. R. Douglas, and G. A. Krafft, Annu. Rev. Nucl. Part. Sci. **51**, 413 (2001).

[Leh00] J. Lehr, M. Effenberger, and U. Mosel, Nucl. Phys. A **671**, 503 (2000).

[Leu98] S. Leupold and U. Mosel, 1998, arXiv:nucl-th/9805024.

[Leu01] S. Leupold, 2001, arXiv:nucl-th/0101013.

[Li95] G. Q. Li, C. M. Ko, and G. E. Brown, Phys. Rev. Lett. **75**, 4007 (1995).

[Lol98] G. J. Lolos et al., Phys. Rev. Lett. **80**, 241 (1998).

[Mas95] M. Massera et al., Nucl. Phys. A **590**, 93c (1995).

[Mec03] B. A. Mecking et al., Nucl. Instr. Methods A **503**, 513 (2003).

[Mes00] M. D. Mestayer et al., Nucl. Instr. Methods A **449**, 81 (2000).

[Mue02] P. Muehlich, T. Falter, C. Greiner, J. Lehr, M. Post, and U. Mosel, 2002, arXiv:nucl-th/0210079.

[Oza01] K. Ozawa et al., Phys. Rev. Lett. **86**, 5019 (2001).

[Oza02] K. Ozawa et al., Nucl. Phys. A **698**, 535c (2002).

[Pet98] W. Peters, M. Post, H. Lenske, S. Leupold, and U. Mosel, Nucl. Phys. A **632**, 109 (1998).

[Ros96] P. Rossi et al., Nucl. Instr. Methods A **381**, 32 (1996).

[Smi99] E. S. Smith et al., Nucl. Instr. Methods A **432**, 265 (1999).

[Sob00] D. I. Sober et al., Nucl. Instrum. Methods A **440**, 263 (2000).

[Son96] C. Song, V. Koch, S. H. Li, and C. M. Ko, Phys. Lett. B **366**, 379 (1996).

[Tei97] S. Teis, W. Cassing, M. Effenberger, A. Hombach, U. Mosel, and G. Wolf, Z. Phys. A **356**, 421 (1997).

[Trn05] D. Trnka et al., 2005, arXiv:nucl-ex/0504010.

[Tur03] C. Tur, 2003, M.S. Thesis.

[Wol93] G. Wolf, W. Cassing, and U. Mosel, Nucl. Phys. A **552**, 549 (1993).